SECTION 1

RESEARCH IN PROGRESS

NUCLEAR REACTIONS -- EXPERIMENTAL

IMPACT PARAMETER SELECTED TWO-PROTON INTENSITY INTERFEROMETRY FOR $^{36}Ar + ^{45}Sc$ AT E/A=80 MeV

M.A. Lisa, C.K. Gelbke, W. Bauer, P. Decowski[a], W.G. Gong[b], E. Gualtieri,S. Hannuschke, R. Lacey[c], T. Li, W.G. Lynch, C.M. Mader, G.F. Peaslee,T. Reposeur[d], A.M. Vander Molen, G.D. Westfall, J. Yee, and S.J. Yennello[e]

Microscopic models based on the Boltzmann-Uehling-Uhlenbeck (BUU) equation make definite predictions for the time evolution of the one-body phase space density created in intermediate energy heavy ion collisions [1-8]. Detailed tests of these predictions are possible through the technique of two-proton intensity interferometry, which makes use of the space-time sensitivity of the two-proton correlation function at small relative momentum [1,9-14]. Model predictions of the behavior of the correlation function depend strongly on impact parameter [1,13], indicating that the space-time evolution of the one-body phase space density is different for central and peripheral collisions. Separate tests of these model predictions for central and peripheral collisions are crucial to distinguish the impact parameters for which the model provides a reasonable description of the reaction from those impact parameters for which there may be physical effects that are poorly understood [1]. We have performed the first study of the two-proton correlation function with simultaneous cuts on the event centrality and on the total momentum of the proton pair. These measurements are used to test BUU predictions of the space-time geometry of the one-body phase space density separately for central and peripheral events.

The experiment was performed with a beam of ^{36}Ar ions at E/A=80 MeV, extracted from the K1200 cyclotron, which bombarded a ^{45}Sc target of areal density 10.0 mg/cm^2. The beam intensity was typically $3x10^8$ particles/sec. Charged particles were measured in the MSU 4π detector array [15], which consisted of 209 plastic ΔE-E phoswich detectors covering polar angles between 7^o and 158^o in the laboratory frame. One of the hexagonal modules of the 4π array, located at 38^o in the lab frame, was replaced by a 56-telescope high-resolution hodoscope [16-18]. Each ΔE-E telescope in the hodoscope consisted of a 300-μm-thick Si detector backed by a 10-cm-long CsI(Tl) detector and subtended a solid angle of $\Delta\Omega$ = 0.37 msr. The nearest-neighbor separation between telescopes was $\Delta\theta = 2.6^o$, and the energy resolution of each telescope was about 1% for 60 MeV protons. During the experiment, both two-proton coincidence and singles events in the hodoscope were recorded in coincidence with the corresponding data from the 4π array.

The experimental two-proton correlation function 1+R(q) is defined in terms of the two-proton coincidence yield $Y_2(\mathbf{p}_1,\mathbf{p}_2)$ and the proton singles yield $Y_1(\mathbf{p})$ [19,20]:

$$\Sigma\, Y_2(\mathbf{p}_1,\mathbf{p}_2) = C\,[1+R(q)]\,\Sigma\, Y_1(\mathbf{p}_1)Y_1(\mathbf{p}_2). \qquad (1)$$

Here, $\mathbf{p}_1$ and $\mathbf{p}_2$ are the laboratory momenta of the two protons, and q is the momentum of relative motion. For a given experimental gating condition, the sums on each side of Eq. (1) extend over all proton energies and detector combinations (of the 56-element hodoscope) corresponding to each q bin. The normalization constant C is determined by the requirement that R(q) vanish for large q.

Following ref. [21], impact parameter selection for the experimental data was achieved via cuts on the transverse energy of the coincident charged particles, defined by

$$E_t = \sum_{i=1}^{N_C} E_i \sin^2 \theta_i \,. \qquad (2)$$

Here, N_C is the charged particle multiplicity measured in the 4π array. (To reduce the effects of "self-biasing" in the impact-parameter-selected correlation functions, particles detected in the 56-element hodoscope were excluded from the sum in Eq. 2.) Gates on the transverse energy were used to construct impact parameter selected two-proton correlation functions.

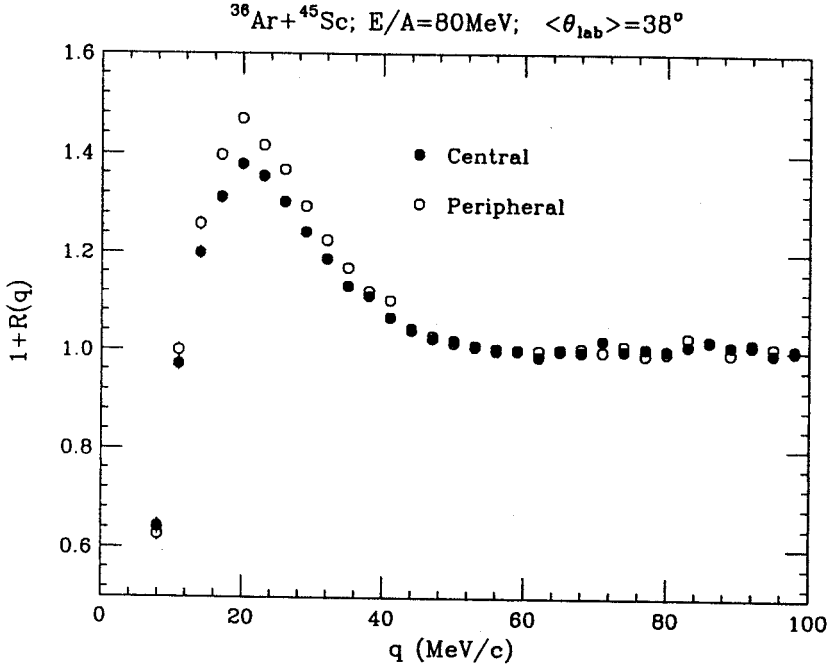

Figure 1: Two-proton correlation functions measured for central and peripheral $^{36}Ar + ^{45}Sc$ collisions at E/A=80 MeV. The correlations were summed over all protons with energies above the detection threshold (about 9 MeV) in the 56-element hodoscope.

Figure 1 shows energy-integrated correlation functions gated on central (high E_t) and peripheral (low E_t) collisions. In a purely geometrical interpretation [21], the employed cuts on E_t represent "reduced" impact parameter cuts of $b/b_{max} \approx 0.0\text{-}0.36$ and 0.44-0.82. The peak of correlation function at q≈20 MeV/c is stronger for peripheral than for central collisions. This observation is qualitatively consistent with the findings of refs. [22-24]. In a static picture, this suggests smaller proton-emitting sources for peripheral collisions.

Considerably more information is obtained when the correlation function is gated on the total momentum of the proton pair, $P = |\mathbf{p}_1+\mathbf{p}_2|$. Figure 2 shows correlation functions for central and peripheral events for two protons with a total momentum in the range P = 400-520 MeV/c (upper panel), and for P ≥ 880 MeV/c (lower panel). Qualitatively consistent with previous inclusive measurements [16,25-34], stronger correlations are observed for proton pairs with high total momentum. Quantitatively, this momentum dependence is also a function of impact parameter. Proton pairs with low total momenta are more strongly correlated in peripheral collisions than in central

collisions. In contrast, the correlation functions constructed from high-momentum pairs in central and peripheral collisions are quite similar.

The total momentum dependence of the two-proton correlation function in central and peripheral events can be used to test detailed predictions of the BUU transport theory. The BUU equation describes the time evolution of the one-body phase space density under the influence of the nuclear mean field and individual nucleon-nucleon collisions. The fact that the emission of fragments is not treated in the theory complicates the comparison of our data to BUU predictions: An observable such as E_t cannot be accurately reproduced by the BUU model because it depends strongly on fragment emission. In order to overcome this dificulty, we employed two methods designed to compare theoretical and experimental results from events of similar impact parameter range.

In the first method, we impose "equivalent" E_t cuts on model events to allow cuts on impact parameter that are similar to those applied to the data. If we denote the measured and calculated inclusive E_t distributions as dP / dE_t and $d\hat{P} / d\hat{E}_t$, then the "equivalent" transverse energies, E_t and $\hat{E}_t$, are defined through the relation

$$\int_{E_t}^{\infty} dE_t' \, dP/dE_t' = \int_{\hat{E}_t}^{\infty} d\hat{E}_t' \, d\hat{P}/d\hat{E}_t' \,. \qquad (3)$$

For the ideal case of a strictly monotonic relationship between transverse energy and impact parameter, the "equivalent" cuts on E_t and $\hat{E}_t$ defined by Eq. 3 select identical regions of impact parameter.

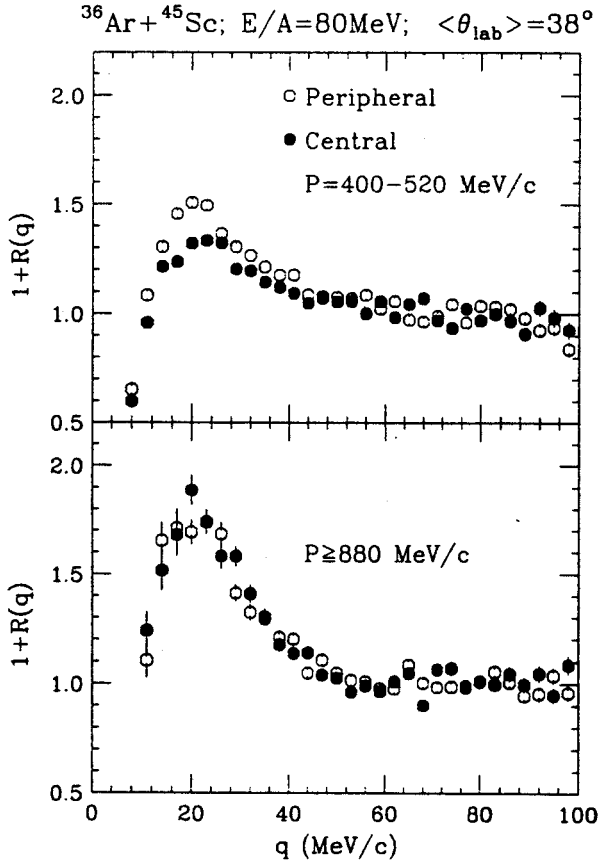

Figure 2: Two-proton correlation functions measured for central (solid points) and peripheral (open points) ^{36}Ar + ^{45}Sc collisions at E/A=80 MeV. Top and bottom panels show results for cuts on low and on high values of the total momenta of the proton pairs.

In the second method, we attempt to extract an impact parameter distribution from the data for each of our centrality cuts which we may use as "input" to the BUU. We extend the prescription of Ref. [21], in which geometrical ideas are used to connect a global observable, such as E_t, to an average reduced impact parameter $\hat{b}(E_t) = b/b_{max}$. The distributions are then convoluted with experimental impact parameter resolution and input into the BUU. Full details of the method are given in Ref. [35].

Theoretical two-proton correlation functions were calculated with the Koonin-Pratt formula, which relates the correlation function to the one-body phase space distribution [9,12,13]. The phase space distribution of emitted particles was calculated with the BUU transport model. Averages over impact parameter were performed and equivalent cuts on transverse energy were applied to the BUU events. The BUU calculations were performed for a stiff equation of state and in-medium cross sections which are equal to the free nucleon-nucleon cross sections. These parameters were successfully used for the description of inclusive correlation functions in this energy domain [13,16,26]. Following refs. [1,13,16,25,26], a particle was considered as emitted if it was located in a region where the local mass density was less than one-eighth normal nuclear density.

The top and bottom panels of Fig. 3 show theoretical and experimental correlation functions for central and peripheral cuts, respectively. The figure shows the total momentum dependence of the average height of the correlation function in the peak region $\langle 1+R \rangle_{15\text{-}25\ MeV/c}$. For reference, we provide on the right-hand axis the Gaussian radius of a zero-lifetime spherical source that produces a correlation function with the same peak value. Data and model predictions are represented by full and open symbols, respectively. Theoretical results corresponding to our two different types of impact parameter weighting for the BUU are shown as square and circular symbols and are labelled "E_t selected" and "$\hat{b}$ selected," respectively; we note that the results are rather independent of the impact parameter weighting scheme used.

For central collisions (top panel), the agreement between experimental and theoretical correlations is quite good, suggesting that the BUU transport theory provides a reasonable description of the final phase space density distribution of nucleons emitted in these collisions. For peripheral collisions (bottom panel), on the other hand, the BUU transport theory underpredicts the total momentum dependence of the correlation function. While the measured peak value of the correlation function increases with the total momentum of the proton pair, the theoretical correlation function depends very little on the total momentum. We cannot rule out that this disagreement could arise from an incomplete understanding of the experimental impact parameter filter. However, two distinct methods were used to simulate the effect of the filter in the theoretical calculations, with similar results.

In summary, we have performed the first measurement of the two-proton correlation function with simultaneous gates on both the total momentum of the proton pair and the event centrality. Correlation functions for central collisions depend more strongly on the total momentum of the proton pair than do correlation functions for peripheral collisions. This implies a strong impact parameter dependence of the space-time evolution of the proton-emitting source created in heavy ion collisions. Theoretical correlation functions were calculated with the BUU equation using the Koonin-Pratt formula. The predicted total momentum dependence of the correlation function agrees well with the data for a central event gate, but disagrees for a peripheral gate. This disagreement suggests that

the present BUU model inadequately describes the evolution of the single-body phase space distribution for peripheral collisions, pointing to an area where future theoretical work is needed. While somewhat unlikely, the disagreement could result from a poor understanding of impact parameter selection. Our calculations were performed with a "standard" set of model parameters which was used successfully in previous work. It is possible that the BUU theory with other parameter sets could provide better agreement with experiment, and further theoretical study is clearly needed.

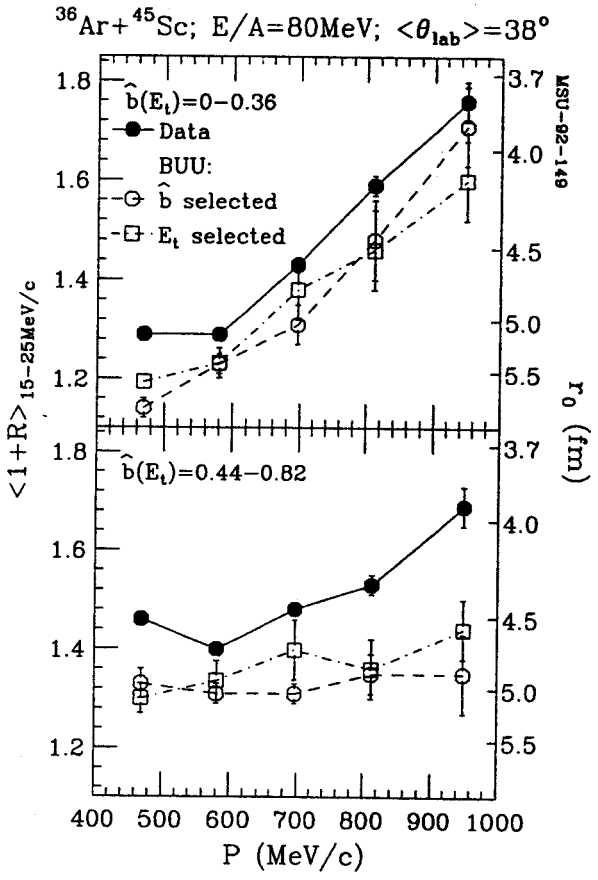

Figure 3: Total momentum dependence of the average height of the two-proton correlation function, <1+R(q)>15-25 MeV/c , for central (top panel) and peripheral (bottom panel) collisions. Solid and open points represent data and transport model predictions, respectively. Details are discussed in the text.

a. Department of Physics, Smith College, Northampton, MA
b. Lawrence Berkeley Laboratory, Berkeley, CA 94720
c. Department of Chemistry, State University of New York, Stony Brook, NY 11776
d. Laboratoire de Physique Nucléaire, Université de Nantes, Nantes Cedex 03, France
e. Cyclotron Instiitute, Texas A&M University, College Station, TX 77843

References

1. W. Bauer, C.K. Gelbke, and S. Pratt, Ann. Rev. Nucl. Part. Sci. **42**, 77 (1992).
2. W. Bauer, G.F. Bertsch, W. Cassing, and U. Mosel, Phys. Rev. C34, 2127 (1986).

3. W. Bauer, Nucl. Phys. A471, 604 (1987);
4. B.A. Li and W. Bauer, Phys. Rev. **C44**, 450 (1991).
5. B.A. Li, W. Bauer, and G.F. Bertsch, Phys. Rev. **C44**, 2095 (1991).
6. H. Stöcker and W. Greiner, Phys. Rep. **137**, 277 (1986).
7. G.F. Bertsch and S. Das Gupta, Phys. Rep. **160**, 189 (1988).
8. P. Schuck et al., Prog. Part. Nucl. Phys. **22**, 181 (1989).
9. S.E. Koonin, Phys. Lett. **70B**, 43 (1977).
10. D.H. Boal and J.C. Shillcock, Phys. Rev. **C33**, 549 (1986).
11. D.H. Boal and H. DeGuise, Phys. Rev. Lett. **57**, 2901 (1986).
12. S. Pratt and M.B. Tsang, Phys. Rev. **C36**, 2390 (1987).
13. W.G. Gong et al., Phys. Rev. **C43**, 781 (1991).
14. D.H. Boal, C.K. Gelbke, and B.K. Jennings, Rev. Mod. Phys. **62**, 553 (1990).
15. G.D. Westfall et al., Nucl. Instr. and Meth. **A238**, 347 (1985).
16. W.G. Gong et al., Phys. Rev. **C43**, 1804 (1991).
17. W.G. Gong etal., Nucl. Instr. and Meth. **A268**, 190 (1988).
18. W.G. Gong et al., Nucl. Instr. and Meth. **A287**, 639 (1990).
19. The momentum dependence of impact parameter selected correlation functions constructed with "singles" (Eq. 1) and "mixed-event" techniques [20] was found to be consistent within statistical errors.
20. M.A. Lisa et al., Phys. Rev. **C44**, 2865 (1991).
21. L. Phair et al., Nucl. Phys. **A548**, 489 (1992).
22. A. Kyanowski et al., Phys. Lett. **B181**, 43 (1986).
23. H.A. Gustafsson et al., Phys. Rev. Lett. **53** 544 (1984).
24. P. Dupieux et al., Phys. Lett. **B200**, 17 (1988).
25. F. Zhu et al., Phys. Rev. **C44**, R582 (1991).
26. W.G. Gong et al., Phys. Rev. Lett. **65**, 2114 (1990).
27. T.C. Awes et al., Phys. Rev. Lett. **61**, (1988).
28. Z. Chen et al., Phys. Rev. **C36**, 2297 (1987).
29. Z. Chen et al., Nucl. Phys. **A473**, 564 (1987).
30. J. Pochodzalla et al., Phys. Rev. **C35**, 1695 (1987).
31. W.G. Gong et al., Phys. Lett. **B246**, 21 (1990).
32. J. Pochodzalla et al., Phys. Lett. **B174**, 36 (1986).
33. W.G. Lynch et al., Phys. Rev. Lett. **51**, 1850 (1983).
34. D. Goujdami et al., Z. Phys. A339, 293 (1991).
35. M.A. Lisa et al., submitted to Phys. Rev. **C**

Energy Dependence of Multifragmentation in ^{84}Kr + ^{197}Au Reactions

G. F. Peaslee, W. Bauer, D. R. Bowman[a], N. Carlin[b], R. J. Charity[c], M. Chartier[d],J. Dinius, D. Fox[e], W. A. Friedman[f], C. K. Gelbke, D. O. Handzy, W. C. Hsi, G. J. Kunde[g], M-C. Lemaire[h], M. A. Lisa, W. G. Lynch, U. Lynen[g], C. M. Mader, L. Phair, J. Pochodzalla[g], H. Sann[g], C. Schwarz, L. G. Sobotka[c], R. T. de Souza[e], S. R. Souza[h], W. Trautmann[g], M. B. Tsang, G. Van Buren[c], and C. Williams

Highly excited nuclear systems have been observed [1-7] to decay by multifragment emission. There is accumulating evidence that multifragment decays are favored for systems that expand to subnormal densities [5-10], and multifragment decays might provide key information about a liquid-gas phase transition in nuclear matter [11-13]. Rather general phase space and barrier penetrability arguments [14-17] lead to the expectation that the multifragment emission probability will exhibit a strong initial rise as a function of temperature. At very high temperatures, on the other hand, the entropy of the system becomes so high that fragment production is suppressed. Hence, fragment production should exhibit a maximum at some intermediate temperature, which will depend on the total charge of the fragmenting system. In fact, measurements of the impact-parameter dependence of fragment emission probabilities in projectile fragmentation reactions of Au nuclei at E/A=600 MeV have revealed the qualitative features of this "rise and fall" of fragment production [3,18]. However, until now, systematic measurements of the beam energy and impact-parameter dependence of multifragment decays did not exist.

Measurements with ^{84}Kr ions at beam energies of E/A=35, 55, and 70 MeV were performed with beams from the K1200 cyclotron. Typical beam intensities were 1-2 $\times 10^8$ particles per second (intensities at E/A=70 MeV were lower by a factor of about two). The measurements at E/A=100, 200, and 400 MeV were performed at the Laboratoire National SATURNE at Saclay, with typical beam intensities of 10^6-10^7 per spill. The gold target thicknesses were: 1.4 mg/cm^2 at E/A=35 and 50 MeV, 4 mg/cm^2 at E/A=70 MeV, 3.0 mg/cm^2 at E/A = 100, and 1.5 mg/cm^2 at E/A=200 and 400 MeV. The emitted charged particles were detected with the combined MSU Miniball/Washington U. Miniwall 4π phoswich detector array. The detector system consisted of 312 low-threshold plastic-scintillator-CsI(Tl) phoswich detectors, covering polar angles of $5.4° < \theta_{lab} < 160°$, corresponding to a total geometric efficiency of approximately 91% of 4π. Wall detectors located at forward angles, $\theta_{lab} = 5.4° - 24°$, used plastic scintillator foils of 80 μm thickness and CsI(Tl) crystals of 3 cm thickness; ball detectors at larger angles, $\theta_{lab} = 24° - 160°$, used 40 μm scintillator foils and 2 cm thick CsI(Tl) crystals. Unit charge resolution up to $Z \approx 15$ was typically achieved for particles that traversed the fast plastic scintillator. At backward angles, where statistics were more limited, charge identification above $Z \approx 6$ was uncertain by $\pm$ 1 charge unit. Approximate energy thresholds for fragments identified by ball detectors were E/A $\approx$ 1.2, 1.5, and 2.5 MeV/nucleon for Z = 1, 3, and 10, respectively; thresholds for particles identified in the wall detectors are higher by approximately 50%. High-energy light charged particles punch through the CsI crystals of the Miniwall at $\approx$100 MeV/nucleon. At the highest bombarding energies, punch-though hydrogen, helium and lithium isotopes could not be distinguished and these particles were identified as Z=1 particles. This misidentification has negligible effect on the measured fragment multiplicities.

In the following text, we will denote as N_{IMF} the number of identified intermediate mass fragments ($3 \leq Z \leq 20$) which have punched through the plastic scintillator foils. The charged particle multiplicity, N_C, is defined as the number of detectors in which at least one charged particle was recorded. This number includes identified fragments, fragments stopped in the plastic scintillator foils, light charged particles, as well as particles which punch through the CsI crystals; because they cannot be unambiguously identified,

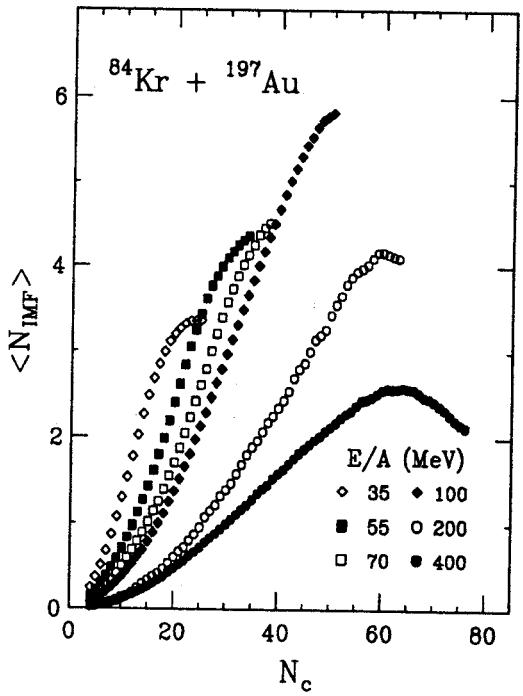

Fig. 1: Relationship between average detected IMF (Z=3-20) multiplicity, $<N_{IMF}>$, and detected charged particle multiplicity, N_C, measured for ^{84}Kr + ^{197}Au collisions. The individual energies are indicated in the figure.

double hits are counted as a single hit.

Figure 1 shows the observed mean IMF multiplicity, $<N_{IMF}>$, as a function of detected charged particle multiplicity N_C for all bombarding energies. For ^{84}Kr + ^{197}Au reactions below E/A $\approx$ 100 MeV, the fragment multiplicity is largest for central collisions, i.e. for high values of N_C. The maximum number of fragments is observed at E/A $\approx$ 100 MeV. At still higher energies, the fragment multiplicity decreases, as qualitatively would be expected from general arguments based upon entropy production.

Charged particle multiplicity distributions measured in this series of experiments have qualitatively similar shapes as those measured in other experiments [5,6,21]. At each energy they exhibit a rather structureless plateau and a near-exponential fall-off at the highest multiplicities. The region where the exponential fall-off begins increases from $N_C \approx 30$ to 80 as the beam energy is increased from E/A = 35 to 400 MeV. As in previous work [20], we constructed a "reduced" impact parameter scale, $\hat{b}$, by means of the geometric formula:

$$\hat{b}(N_C) = \frac{1}{\sqrt{\sigma_R}} \sqrt{\sum_{N=N_C}^{\infty} \sigma(N)} \qquad (1)$$

where $\sigma(N)$ is the cross section for detecting the N charged particles and $\sigma_R = \sum_4^{\infty} \sigma(N)$, is the reaction cross section for $N_C > 3$. The reduced impact parameter assumes values of $\hat{b} = 1$ for the most peripheral collisions and $\hat{b} = 0$ for the most central collisions.

In Figure 2, we show the bombarding energy dependence of $<N_{IMF}>$ for different cuts on the reduced impact parameter, $\hat{b}$, defined in Eq. 1. For the most peripheral collisions ($\hat{b} \geq 0.75$) the average

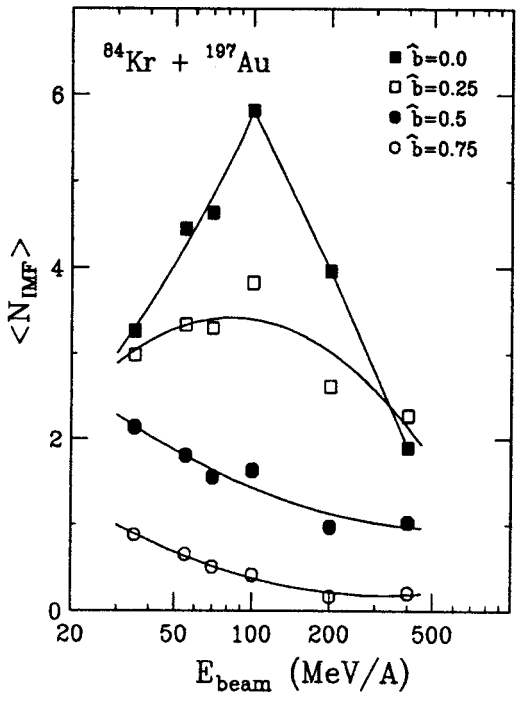

Fig. 2: Beam energy dependence of $<N_{IMF}>$ for different cuts on reduced impact parameter (Eq. 1). The individual cuts are indicated in the figure. The curves are to guide the eye.

number of detected fragments remains small. For smaller impact parameters ($\hat{b} \leq 0.5$), the fragment multiplicity increases up to E/A $\approx$ 100 MeV and then decreases for higher energies. All impact parameters between $\hat{b} = 0$ and 0.25 give approximately the same results, which reflects the mass asymmetry of the entrance channel for this reaction. The decrease at higher energies is faster for central cuts than for cuts on mid-impact parameters, and at the highest energy (E/A=400 MeV) the fragment multiplicities for central collisions are lower than for non-central collisions. With increasing bombarding energy, IMFs produced in the decay of near-beam velocity fragments are focused into an increasingly smaller cone around the beam axis, and the efficiency for the detection of these fragments decreases with energy due to our lack of coverage at $\theta_{lab} < 5.4°$. For non-central collisions, the decrease of $<N_{IMF}>$ with increasing energy may therefore be even less rapid than implied in Fig. 2.

A detailed understanding of the observed energy and impact-parameter dependence of the fragment multiplicities requires a full dynamical treatment of the temporal and spatial evolution of the reaction zone, as well as inclusion of the important statistical decay of the reaction products. This problem has not yet been solved in a consistent framework. In order to provide a perspective and a qualitative understanding of the energy dependence of the IMF multiplicities observed in central collisions, we resort to a hybrid approach which has been previously used [21]. In this approach, the initial phase of the reaction is treated within the framework of the semiclassical Boltzmann-Ühling-Uhlenbeck (BUU) theory [22,23] which describes the evolution of the one-body density distribution. The model incorporates nucleon-nucleon collisions, a density-dependent mean field, and a simple Pauli-blocking prescription to prevent scattering into occupied regions of phase space. As this theory neglects cluster formation, we treat the final stages of the reaction in the framework of the Expanding Evaporating Source (EES) model of ref. [8,9], which incorporates important

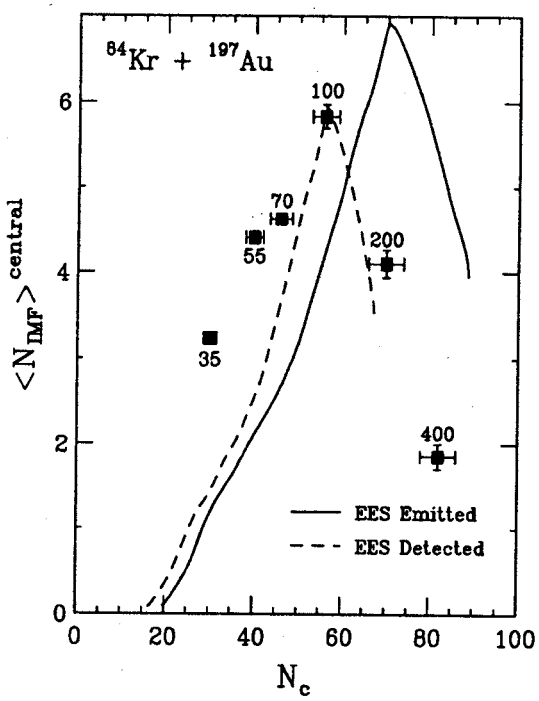

Fig. 3: Relationship between average IMF and charged particle multiplicities, $<N_{IMF}>$ and $<N_C>$ measured for central ^{84}Kr + ^{197}Au collisions. Solid points represent measured values; horizontal and vertical bars indicate the widths of the cuts on N_C and the extreme values of N_{IMF} within these cuts. Dashed and solid curves represent results of the filtered and unfiltered calculations with the hybrid-model described in the text.

aspects of the competition between expansion dynamics and statistical fragment emission from a compound nucleus. Alternative hybrid treatments [3,24] may provide comparable insight. Details of our particular approach and a discussion of conceptual difficulties inherent in such hybrid approaches are given in ref. [21].

Hybrid calculations were performed for all incident energies. For each beam energy, the average numbers of emitted charged particles and intermediate mass fragments, $<N_C>$ and $<N_{IMF}>$, were determined. ($<N_C>$ is the sum of the "preequilibrium" proton multiplicity calculated from the BUU model and the light charged particle multiplicity calculated by the expanding evaporating source model). In Fig. 3, the results of these calculations are compared to the experimental values determined at the various energies for central cuts corresponding to $\hat{b} \leq 0.1$. The solid curves show the results of the "raw" calculations, and the dashed curves show the results of calculations filtered by the response of the experimental apparatus.

The filtered calculations reproduce the qualitative trend of the data, including the approximate location of the maximum of $<N_{IMF}>$ as a function of $<N_C>$. There are, however, considerable discrepancies, particularly at low values of $<N_C>$, i.e. at lower beam energies. Such discrepancies are not surprising, and they reflect inherent difficulties of our hybrid model: At low energies, expansion occurs late (if at all), and there is considerable uncertainty with regard to the time at which the two models are to be matched. Our prescription may make the transition from one model to the other too late in time, thus leading to an overestimate of preequilibrium emission and a corresponding underestimate of the initial temperature of the reaction zone from which fragment emission is allowed. Clearly, there is further work to be done to optimize the agreement between calculations and experiment.

In summary, we have presented the first comprehensive study of the multifragment emission over

a broad range of beam energies, E/A = 35 - 400 MeV. The unique value of this work lies in the low energy thresholds for fragment detection and the broad range of beam energies investigated. For the ^{84}Kr + ^{197}Au system, fragment multiplicities are greatest at E/A $\approx$ 100 MeV. For central collisions, the energy dependence of fragment production qualitatively agrees with simple hybrid model predictions, which treat the early stages of the reaction in terms of BUU transport calculations and the later stages of the reaction in terms of the decay of an expanding compound nucleus. However, significant discrepancies between theory and experiment remain to be resolved, indicating the need for a more comprehensive transport approach for the treatment of density fluctuations and fragment formation.

[a]Chalk River Laboratories, Chalk River, Ontario K0J 1J0, Canada
[b]Instituto de Fisica, Universidade de Sao Paulo, C. Postal 20516, CEP 01498, Sao Paulo, Brazil
[c]Department of Chemistry, Washington University. St. Louis, MO 63130
[d]Institute de Physique Nucléaire, 91406 Orsay Cedex, France
[e]Department of Chemistry and IUCF, Indiana University, Bloomington, IN 47405
[f]Department of Physics, University of Wisconsin, Madison, WI 53706
[g]Gesellschaft für Schwerionenforschung, D-6100 Darmstadt 11, Germany
[h]Laboratoire National SATURNE, Saclay, France

References

1. J.W. Harris et al., Nucl. Phys. **A471**, 241 (1987).
2. R. Bougault, et al., Nucl. Phys. **A488**, 255 (1988).
3. C.A. Ogilvie et al., Phys. Rev. Lett **67**, 1214 (1991).
4. Y. Blumenfeld et al., Phys. Rev. Lett. **66**, 576 (1991).
5. D.R. Bowman et al., Phys. Rev. Lett. **67** 1527 (1991).
6. R.T. de Souza et al., Phys. Lett. **B268** 6 (1991).
7. K. Hagel et al., Phys. Rev. Lett. **68** 2141 (1992).
8. W.A. Friedman, Phys. Rev. Lett. **60**, 2125 (1988).
9. W.A. Friedman, Phys. Rev. **C42**, 667 (1990).
10. J. Hubele et al., Phys. Rev. **C46**, R1577 (1992)
11. G. Bertsch and P.J. Siemens, Phys. Lett. **126B**, 9 (1983).
12. P.J. Siemens, Nature **305**, 410 (1983).
13. T.J. Schlagel and V.R. Pandharipande, Phys. Rev. **C36**, 162 (1987).
14. L.G. Moretto, Nucl. Phys. **A247**, 211 (1975).
15. W.A. Friedman and W.G. Lynch, Phys. Rev. **C28**, 16 (1983).
16. D.H.E. Gross, Rep. Prog. Phys. **53**, 605 (1990).
17. L.G. Sobotka, et al., Phys. Rev. Lett. **51**, 2187 (1983).
18. J. Hubele et al., Z.Phys. **A340**, 263 (1991).
19. R.T. de Souza et al., Nucl. Instr. Meth. **A295** 109 (1990).
20. L. Phair et al., Nucl. Phys. **A548**, 489 (1992).
21. D.R. Bowman et al., Phys. Rev. **C46**, 1834 (1992).
22. W. Bauer et al., Phys. Rev. **C34**, 2127 (1986).
23. W. Bauer, Phys. Rev. Lett. **61**, 2534 (1988).
24. M. Blann et al., Phys. Rev. **C44**, 431 (1992).

FLUCTUATIONS IN MULTIFRAGMENT DECAYS

L. Phair, M.A. Lisa, D.R. Bowman[a], C.K. Gelbke, W.G. Gong[b], Y.D. Kim[c], W.G. Lynch, G.F. Peaslee, H. Schulz, R.T. de Souza[d], M.B. Tsang, and F. Zhu[e]

A recent analysis [1] of fragment size distributions observed in reactions induced by gold on emulsion at E/A=1 GeV [2] saw evidence for intermittency, which might indicate that fragmentation processes are scale invariant. We take up the problem of intermittency by analyzing the factorial moments of charge distributions observed in ^{36}Ar+^{197}Au reactions at beam energies between 35 and 110 MeV per nucleon [3].

The occurrence of intermittency is deduced from the factorial moments [4]

$$F_k(\Delta) = \frac{\sum_{i=1}^{Z_0/\Delta} \langle N_i(N_i-1)\ldots(N_i-k+1)\rangle}{\sum_{i=1}^{Z_0/\Delta} \langle N_i\rangle^k} \tag{1}$$

where Z_0 is the total charge of the disintegrating nuclear system, Δ is a binning parameter, and N_i is the number of fragments with charges in the interval $(i\text{-}1)\Delta < Z \le i\Delta$ where $i=1,\ldots,Z_0/\Delta$. The ensemble average $\langle\ \rangle$ is performed over all fragmentation events considered. Intermittency is defined by a relation [4]

$$F_k(\Delta') = F_k(a\Delta) = a^{-f(k)} F_k(\Delta) \tag{2}$$

between factorial moments $F_k(\Delta')$ and $F_k(\Delta)$ obtained for two different binning parameters Δ and $\Delta' = a\Delta$. Generally, evidence for intermittency has been obtained by examining the double logarithmic plot of $\ln F_k$ versus $-\ln\Delta$. Plots which show lines of positive slope are consistent with nonzero fractal dimension and considered to display intermittency. By construction, the factorial moments $F_k(\Delta)$ are unity for Poisson distributions. Hence, Poisson distributions do not exhibit intermittency. The expression for the second factorial moment can be written as

$$F_2(\Delta) = 1 + \frac{\sum_i \left(\sigma_i^2 - \langle N_i\rangle\right)}{\sum_i \langle N_i\rangle^2} \tag{3}$$

where $\langle N_i\rangle$ and σ_i denote the mean value and the variance of the multiplicity distribution in the ith bin. Distributions which are narrower (broader) than Poisson distributions possess moments which are less (greater) than unity. For $\Delta = Z_0$, the right hand side of eq. (3) reduces to $1 + \left(\sigma_c^2 - \langle N_c\rangle\right)/\langle N_c\rangle^2$, where $\langle N_c\rangle$ and σ_c^2 are the mean value and the variance of the charged particle multiplicity distribution.

Intermittency as an indicator of nontrivial physics is generally sought for systems exhibiting larger than Poisson fluctuations. Evidence for such large fluctuations must be sought in events representing similar initial conditions. Constraints from conservation laws may lead to reduced fluctuations.

In order to explore whether there is a basis for non-trivial intermittent behavior in a reaction in which multifragment emission has been observed, we analyzed the first and second moments of the charged particle multiplicity distributions measured [3], with a low-threshold 4π detector array [5], for ^{36}Ar+^{197}Au

collisions over a broad range of energies, 35≤ E/A≤110 MeV. Event selection was performed by cuts on the total transverse energy, $E_t = E\sin^2\theta$, of the emitted charged particles. For orientation, we also provide an empirical impact parameter scale by using the geometrical prescription [6],

$$\hat{b}(E_t) = \frac{1}{\sqrt{\sigma_R}}\left(\int_{E_t}^{\infty}\frac{d\sigma(\varepsilon)}{d\varepsilon}d\varepsilon\right)^{1/2} \qquad (4)$$

where $d\sigma(E_t)/dE_t$ is the cross section for events in which the transverse energy of all detected charged particles falls into the interval $E_t \pm \frac{1}{2}dE_t$ and σ_R is the reaction cross section for events satisfying the trigger condition $N_C \geq 2$ [3]. The "reduced" impact parameter $\hat{b}$ assumes values of $\hat{b} \approx 1$ for peripheral collisions and $\hat{b} \approx 0$ for the most violent collisions characterized by large values of E_t.

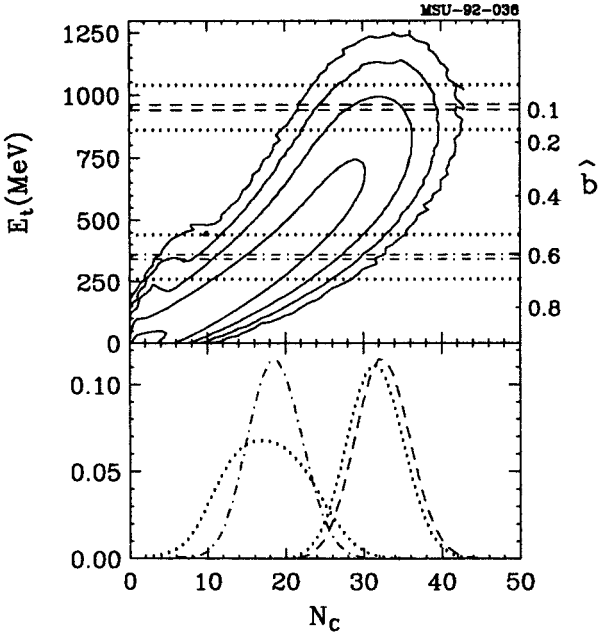

Figure 1: Upper part: Measured relation between transverse energy E_t and total charged particle multiplicity for $^{36}Ar+^{197}Au$ reactions at E/A=110 MeV. Lower part: Charged particle multiplicity distributions for the cuts on E_t, indicated in the top panel.

The top panel in Fig. 1 shows the measured two-dimensional correlation between transverse energy E_t and charged particle multiplicity N_C for $^{36}Ar+^{197}Au$ collisions at E/A=110 MeV. The dashed and dot-dashed curves in the bottom panel of Fig.1 depict charged particle distributions selected by narrow cuts on E_t, corresponding to reduced impact parameters $\hat{b} \approx 0.1$ and 0.6. The dotted curves illustrate the effects of increasing the widths, ΔE_t, of the cuts as indicated by dotted horizontal lines in the top panel. For central collisions, the N_C distribution is rather insensitive to ΔE_t, but for more peripheral collisions it suffers considerable broadening as ΔE_t is increased.

The broadening due to impact parameter averaging is illustrated more quantitatively in Fig. 2. Top, center and bottom panels of the figure depict the quantities $\sigma_C^2/\langle N_C\rangle$, σ_C^2, and $\langle N_C\rangle$, respectively, as a function of transverse energy. Solid circular, open square-shaped and star-shaped points show values obtained for cuts of widths ΔE_t=20, 180 and 340 MeV, respectively. For narrow cuts on ΔE_t, the charged particle multiplicity distributions are inconsistent with $F_2(\Delta = Z_0) > 1$, since $\sigma_C^2/\langle N_C\rangle < 1$. For near-central collisions, $\hat{b}$<0.3, the extracted values of $\sigma_C^2/\langle N_C\rangle$ exhibit little dependence on the widths of the applied cuts. However, for larger impact parameters, $\hat{b}$>0.4, wide cuts on E_t cause an artificial broadening of the multiplicity distributions resulting from the superposition of distributions with different centroids. Poorly defined ensembles of events may therefore exhibit larger than

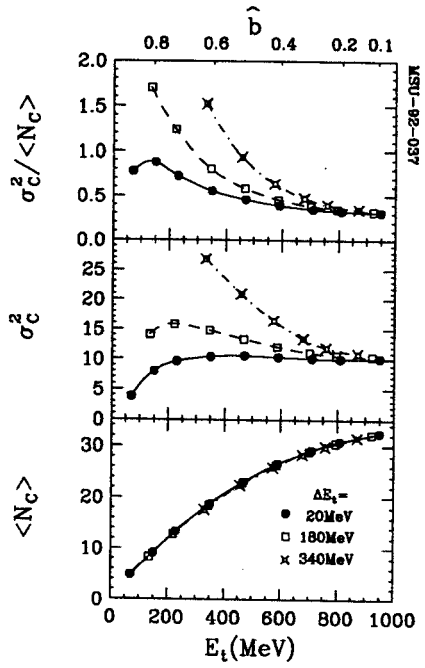

Fig. 2: Bottom, center and top panels show the mean values $\langle N_c \rangle$, variances σ_c^2 , and ratios $\sigma_c^2 / \langle N_c \rangle$ of the charged particle multiplicity distributions for $^{36}Ar+^{197}Au$ reactions at E/A=110 MeV. These quantities were selected by various cuts on the transverse energy; the mean values of these cuts are given by the abscissa and the widths are given in the figure. The upper scale gives the reduced impact parameter $\hat{b}$ related to E_t via Eq. (4).

Poisson variances, $\sigma_c^2 / \langle N_c \rangle > 1$. However, these large variances are an artifact from impact parameter averaging, and they do not represent intrinsic fluctuations of the decaying system.

Figure 3 depicts the relation between $\langle N_c \rangle$ and $\sigma_c^2 / \langle N_c \rangle$ extracted for central ($\hat{b}$<0.3) $^{36}Ar+^{197}Au$ collisions at the incident energies of E/A=35, 50, 80, and 110 MeV. At all energies, the fluctuations of the charged particle multiplicity are considerably smaller than expected for Poisson distributions.

In order to explore effects resulting from phase space constraints such as energy conservation, we performed calculations with the bond-percolation model of refs. [7,8]. For simplicity, we assumed the decay of the composite system (A=233, Z=97). Calculations with bond-breaking parameters close to the critical value of p=0.7 have already been shown [9] to reproduce the element distributions measured for the present reaction. Standard percolation calculations (in which the number of broken bonds is allowed to fluctuate from event to event) predict fluctuations in N_c which are much larger than observed experimentally. Open circular points in Fig. 3 show representative results for p=0.6 and 0.7. The indicated shift from the open circle to the open triangular point illustrates the magnitude of instrumental distortions [9] for the case p=0.7. These distortions are too small to affect our conclusions. If one introduces a constraint analogous to energy conservation by requiring a fixed number of broken bonds, much narrower charged particle distributions are produced (see open diamonds). These illustrative calculations suggest that the widths of impact parameter selected charged particle multiplicity distributions are strongly affected by phase space constraints due to energy conservation.

This conclusion is corroborated by more realistic statistical model calculations which incorporate energy conservation on an event-by-event basis. The open square and star-shaped points show predictions of the sequential decay model GEMINI [10] and of the Copenhagen fragmentation model [11], respectively. (The individual points represent results obtained for the decay of heavy compound nuclei at various excitation energies.) Both microcanonical and sequential decay models predict ratios $\sigma_c^2 / \langle N_c \rangle$ somewhat smaller than observed experimentally, and they do not show intermittency [12,13].

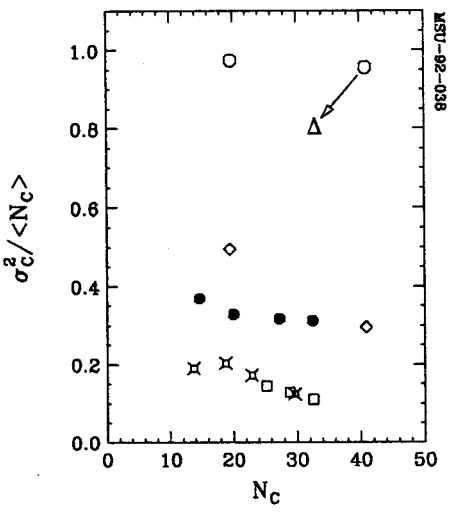

Fig. 3: Relation between mean charged particle multiplicity $\langle N_C \rangle$ and the ratios $\sigma_C^2 / \langle N_C \rangle$. Solid circular points: experimental values extracted from near-central ^{36}Ar+^{197}Au reactions at E/A=35, 50, 80 and 110 MeV. Open symbols explained in the text

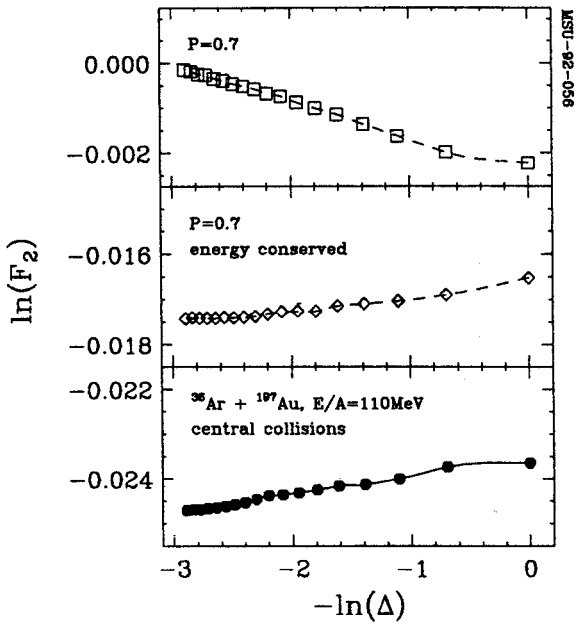

Fig. 4: Scaled factorial moments as a function of binning resolution. Solid points show experimental results for central ^{36}Ar+ ^{197}Au collisions at E/A=110 MeV. Open points show results from percolation calculations using p=0.7. Open squares depict calculations in which the total number of broken bonds is allowed to fluctuate; open diamonds represent calculations in which the total number of bonds is kept fixed.

In Fig. 4, second factorial moments calculated from Eq. 1 are presented as a function of binning resolution. The solid points represent experimental data selected by a narrow cut on central collisions at E/A=110 MeV. A slightly positive slope is observed, but the moments are smaller than unity. As argued above, this positive slope may be of trivial origin. In order to corroborate this point, we include the results of percolation calculations performed for p=0.7. Standard calculations for which the total number of broken bonds is allowed to fluctuate (open squares) predict large factorial moments, but no intermittency. When the number of broken bonds is constrained to be constant (open diamonds), the factorial moments are strongly reduced in magnitude, and they exhibit a small increase as a function of binning resolution, similar to that observed experimentally. This increase appears to be of little significance.

In summary, we argue that an intermittent signal is meaningful only when it is observed in data selected by a narrow cut in impact parameter, and only when $F_2(\Delta)>1$. These two conditions are never simultaneously met in our data. A surprisingly small value of about $\sigma_C^2 / \langle N_C \rangle \approx 0.3$ was measured in central collisions, independent of beam energy. The small widths of the charged particle distributions may be caused by the constraints imposed by energy conservation.

a. Chalk River Laboratories, Chalk River, Ontario K0J 1J0, Canada
b. Lawrence Berkeley Laboratory, University of California, Berkeley, CA 94720
c. National Laboratory for High Energy Physics, 1-1 Oho, Tsukuba, Ibaraki 305, Japan

d. Indiana University Cyclotron Facility and Department of Chemistry, Indiana University, Bloomington, IN 47405
e Brookhaven National Laboratory, Upton, Long Island, NY 11973

References

1. M. Ploszajczak and A. Tucholski, Phys. Rev. Lett. **65** (1990) 1539.
2. C.J. Waddington and P.S. Freier, Phys. Rev. C **31** (1985) 888.
3. R.T. de Souza et al., Phys. Lett. **B268** (1991) 6; D. Fox et al., Phys. Rev. C **47**, (1993) R421.
4. A. Bialas and R. Peschanski, Nucl. Phys. **B273** (1986) 703; **B308** (1988) 857.
5. R.T. de Souza et al., Nucl. Instr. and Meth. **A295** (1990) 109.
6. L. Phair et al., Nucl. Phys. **A548** (1992) 489
7. W. Bauer et al., Phys. Lett. B **150** (1985) 53; Nucl. Phys. **A452** (1986) 699.
8. W. Bauer, Phys. Rev. C **38** (1988) 1927.
9. L. Phair et al., Phys. Lett. B **285** (1992) 10.
10. R.J. Charity et al., Nucl. Phys. **A483** (1988) 371.
11. J.P. Bondorf et al., Nucl. Phys. **A443** (1985) 321; Nucl. Phys. **A444** (1986) 460; H.W. Barz et al., Nucl. Phys. **A448** (1986) 753.
12. H.W. Barz et al., Phys. Rev. C (1992), and Nucl. Phys. A (1992) in press.
13. B. Ellatari et al., preprint Strasbourg PHTH 19-91 (1991).

IMPACT PARAMETER FILTERS FOR $^{36}Ar+^{197}Au$ COLLISIONS AT E/A=50, 80 AND 110 MeV

L. Phair, D.R. Bowman[a], C.K. Gelbke, W.G. Gong[b], Y.D. Kim[c], M.A. Lisa, W.G. Lynch, G.F. Peaslee, R.T. de Souza[d], M.B. Tsang, and F. Zhu[e]

In most experiments, information about the impact parameter is extracted from quantities which relate to the collision geometry via simple intuitive pictures. Many impact parameter filters represent some measure of the "violence" of the reaction which, in turn, is assumed to be related to the collision geometry. Common impact parameter filters are based upon the measured multiplicity of charged particles [1-4], the transverse energy [5], or the summed charge of particles emitted at intermediate rapidity [6]. For collisions with incident energies of a few hundred MeV per nucleon, the summed charge, Z_{bound}, of particles with atomic number $Z \geq 2$ [7] has also been used. This quantity is the complement of the combined p, d, and t multiplicity. At lower energies, E/A=20-50 MeV, comparable information on impact parameter has been extracted from measurements of the velocities of fusion-like residues [8-10], charged particle multiplicities [10,11], or neutron multiplicities [8,12].

A priori it is unclear to what extent the various techniques select similar or equivalent impact parameters, and whether one technique provides superior resolution as compared to another. At low energies, cross calibrations have been performed between the linear momentum transfer techniques and the emitted charged [11] or neutral particle multiplicities [8]. We have investigated $^{36}Ar+^{197}Au$ collisions at several incident energies and explored the relation between impact parameter filters based upon the charged-particle multiplicity, N_C, the total transverse kinetic energy of detected charged particles, E_t, the mid-rapidity charge, Z_y, and the multiplicity of hydrogen nuclei, N_1.

The experiment was performed with ^{36}Ar beams extracted from K1200 cyclotron. The beam energies were E/A=50, 80, and 110 MeV and the extracted intensities were 10^8 particles per second. The areal density of the gold target was approximately 1 mg/cm^2. Light particles and complex fragments were detected with the MSU Miniball phoswich detector array [13]. Details about the detector geometry are given in refs. [13,14].

We use the following quantities to extract information on the magnitude of the impact parameter:

(1) The charged particle multiplicity, N_C. The number N_C is equal to the number of detectors in which at least one charged particle is detected in a given event.

(2) The total transverse kinetic energy of identified particles, E_t, is defined [14] as

$$E_t = \sum_i E_i \sin^2 \theta_i = \sum_i \frac{(p_i \sin \theta_i)^2}{2m_i}. \quad (1)$$

Here, E_i, p_i and θ_i denote the kinetic energy, momentum and emission angle of particle i with respect to the beam axis.

(3) The mid-rapidity charge, Z_y, is defined [6] as the summed charge of all identified particles of center-of-mass rapidity y with

$$0.75y_{tar} \le y \le 0.75y_{proj}. \tag{2}$$

(4) The identified hydrogen multiplicity, N_1. This quantity is defined as the number of detectors in which a Z=1 particle is identified.

In order to construct an approximate scale for the impact parameter, we adopt the geometrical prescription of ref. [4]. For each of the quantities N_C, E_t, Z_y, and N_1, we assume a monotonic relationship to the impact parameter and define the reduced impact parameter scale via

$$\frac{b(X)}{b_{\max}} = \hat{b}(X) = \left\{ \int_X^{\infty} \frac{dP(X')}{dX'} dX' \right\}^{1/2}, \tag{3}$$

where X=N_C, E_t, Z_y, and N_1; $dP(X)/dX$ is the normalized probability distribution for the measured quantity X, and b_{max} is the maximum impact parameter for which particles were detected in the Miniball ($N_C \ge 2$). $\hat{b}$ ranges from $\hat{b}$=1 for glancing collisions to $\hat{b}$=0 for head-on collisions.

While geometrical prescriptions implicit in equation (3) may provide reasonable scales for the

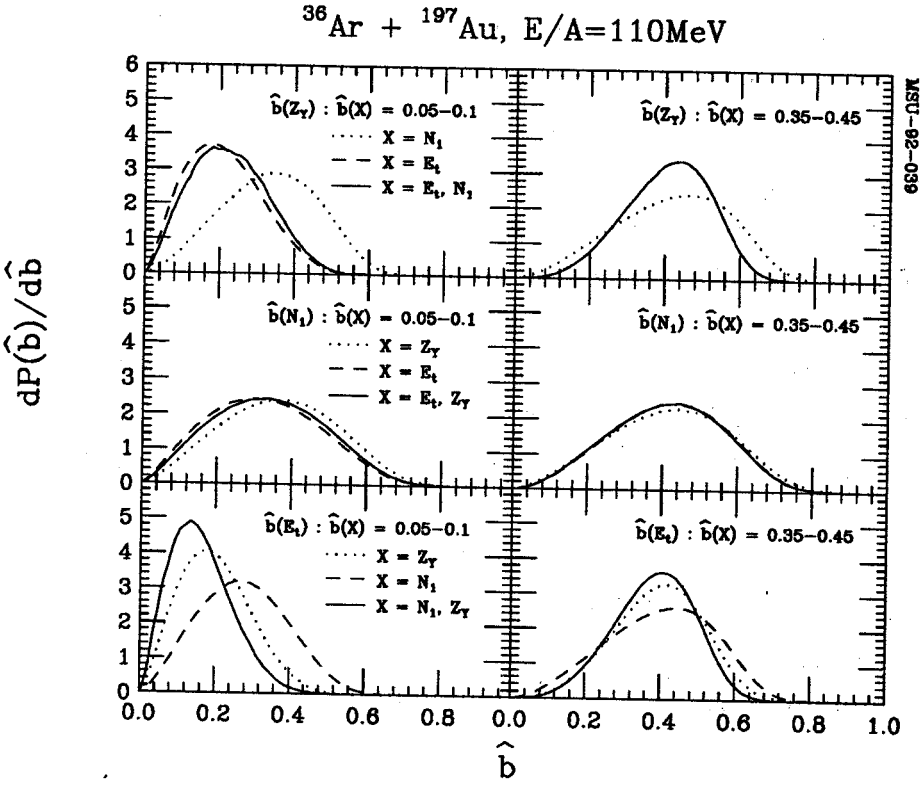

Figure 1: Conditional impact parameter distributions of $\hat{b}(Y)$ extracted for Y=Z_y(top panels), Y=N_1 (center panels), and Y=E_t (bottom panels) for the ^{36}Ar+^{197}Au reaction at E/A=110 MeV. Left and right hand panels show distributions selected by impact parameter cuts $\hat{b}(X)$=0.05-0.1 and $\hat{b}(X)$=0.35- 0.45 on the indicated observables (X=N_1, E_t, and Z_y). All impact parameter scales were constructed according to equation 3.

average relation between charged-particle multiplicity and impact parameter, it is not clear whether the scales extracted from the various quantities are commensurate. Furthermore, for collisions at fixed impact parameter, these quantities exhibit fluctuations of unknown magnitude. Therefore, reaction filters constructed from the various observables could have different resolution.

In order to investigate the relation between impact parameter scales extracted via equation (3) from the various measured observables, we have set narrow gates on impact parameters $\hat{b}(X)$, defined by means of an observable X, and determined the conditional distributions of impact parameters $\hat{b}(Y)$, constructed from different observables Y ($Y \neq X$ and $X,Y = N_C, E_t, Z_y$, and N_1).

Conditional impact parameter distributions are presented in figures 1-2. Individual panels of these figures show conditional impact parameter distributions $\hat{b}(Y)$ determined from the indicated observables Y. Left and right hand panels show distributions extracted for the cuts $\hat{b}(X)$=0.05-0.1 and $\hat{b}(X)$=0.35-0.45, respectively. Dashed and dotted curves show results obtained by cuts placed on one observable, and solid curves show results obtained by simultaneous cuts placed on two observables. The observables X used for these cuts are indicated in the individual left-hand panels; the conventions for left and right panels are identical. For better comparison, all conditional impact parameter distributions are normalized to unit area.

For the present reaction, impact parameter filters based upon N_1 (the complement of Z_{bound}) are considerably less selective than reaction filters based upon N_C, E_t, and Z_y. This effect is clear from figure 1,

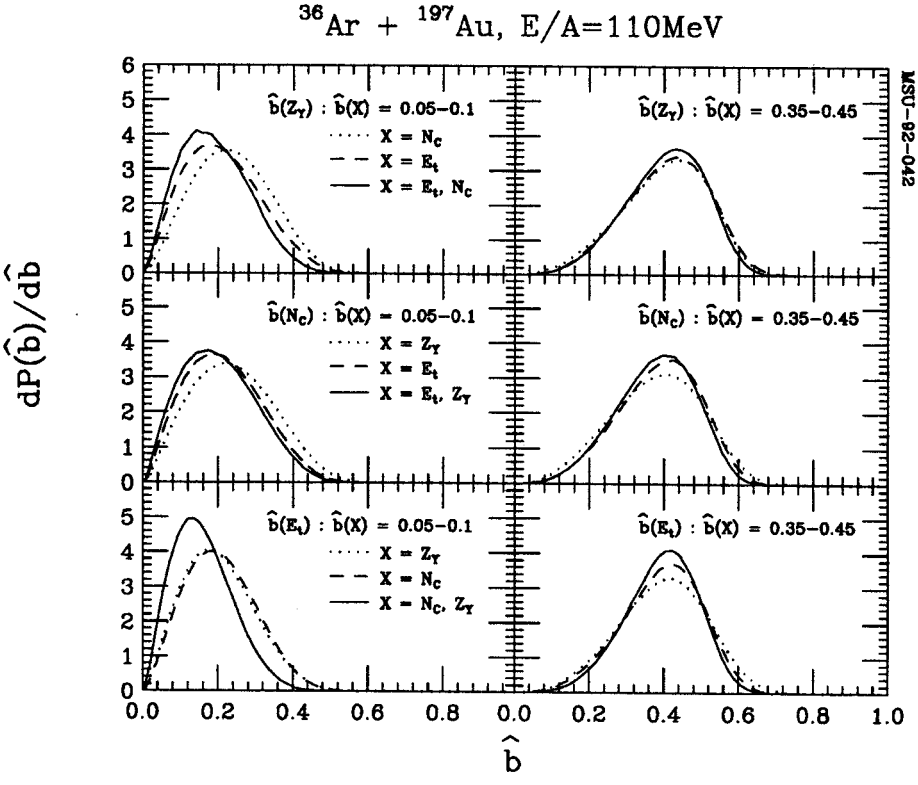

Figure 2: As figure 1 but replacing N_1 with N_C.

which compares conditional distributions based upon N_1, E_t, and Z_y for collisions at E/A=110 MeV. The reduced resolution of impact parameter filters based upon N_1 is most likely of statistical origin. For collisions at fixed impact parameter, the relative magnitude of statistical fluctuations is enhanced for the observable N_1 because it contains, by definition, only a small subset of the emitted particles.

Figure 2 presents conditional impact parameter distributions for filters based on N_C, E_t, and Z_y. Cuts on small impact parameters, $\hat{b}(X)$=0.05-0.1, generally produce conditional distributions peaked at larger impact parameters, $\hat{b}(Y)$=0.2. Conditional impact parameter distributions extracted for simultaneous cuts on small impact parameters, $\hat{b}(X_1)=\hat{b}(X_2)$=0.05-0.1, are slightly narrower and they peak at lower impact parameters, $\hat{b}(Y)$=0.12-0.16, than those obtained from cuts on a single observable. Hence, somewhat improved selection of central collisions can be obtained from multi-dimensional cuts.

One-dimensional cuts on $\hat{b}(E_t)$=0.05-0.1 produce narrower distributions in $\hat{b}(N_C)$ and $\hat{b}(Z_y)$ than the alternative one-dimensional cuts on $\hat{b}(Z_y)$ and $\hat{b}(N_C)$, respectively. Furthermore, two-dimensional cuts on small impact parameters produce narrower distributions for $\hat{b}(E_t)$ than for $\hat{b}(N_C)$ and $\hat{b}(Z_y)$. These observations suggest that filters based upon E_t may more effective in selecting central collisions than filters based upon the other observables listed in this report.

For cuts on intermediate impact parameters, $\hat{b}(X)$=0.35-0.45, the conditional distributions of $\hat{b}(Y)$ are peaked at values close to $\hat{b}(Y)$=0.4, i.e. close to the cut on $\hat{b}(X)$. Again, small improvements in resolution are obtained by the application of two-dimensional cuts. However, these improvements are less pronounced than that seen for very small impact parameters.

We have explored the efficiency of various impact parameter filters in terms of their ability to suppress projectile-like fragments emitted with near-beam velocity at forward angles. For illustration, Figure 3 shows the energy spectra of beryllium (left-hand panels) and carbon (right-hand panels) nuclei detected in Rings 1-10 in the Miniball for an incident energy of E/A=110 MeV. Top and bottom panels show the energy spectra gated by cuts on the charged particle multiplicity corresponding to $\hat{b}(N_C)$>0.6 and $\hat{b}(N_C)$<0.3, respectively. The energy spectra gated by large impact parameters exhibit pronounced maxima at forward angles which correspond to fragment velocities close to the beam velocity. Such projectile-like contributions are strongly suppressed in the energy spectra selected by high-multiplicity cuts corresponding to $\hat{b}(N_C)$<0.3. These qualitative findings are consistent with observations at lower energy, E/A=35 MeV [16]. They indicate that impact parameter filters based upon charged particle multiplicity are rather effective in selecting collisions with large geometrical overlap between target and projectile even in situations where simple participant-spectator models are not expected to be accurate in detail.

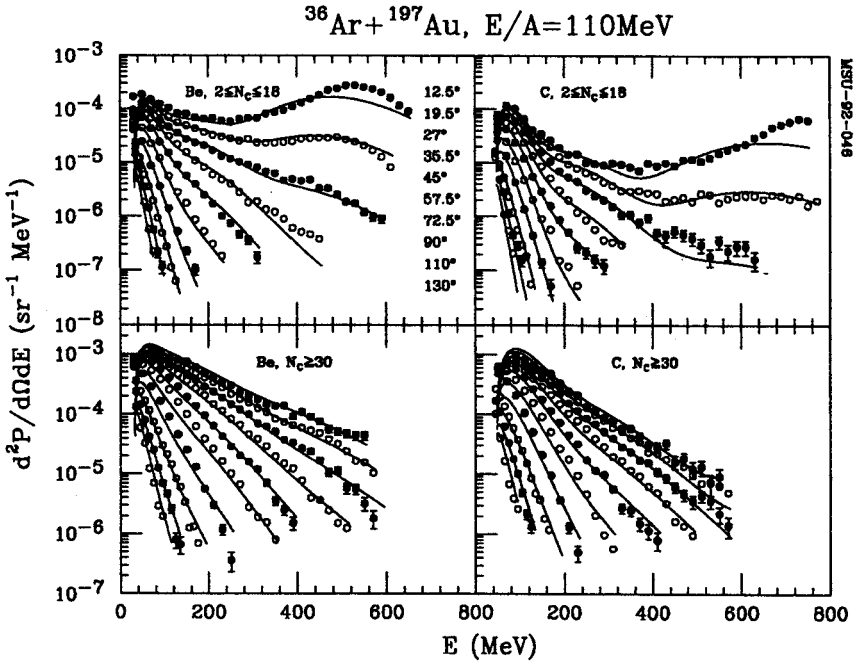

Figure 3: Energy spectra of beryllium (left hand panels) and carbon (right hand panels) nuclei emitted in peripheral ($\hat{b}$>0.6, top panels) and central($\hat{b}$<0.3, bottom panels) ^{36}Ar+^{197}Au collisions at E/A=110 MeV. The exact cuts on the measured charged particle multiplicity are given in the figure. The solid curves are fits with equation. (4).

In order to provide a more quantitative basis for discussing the effects of impact parameter filtering on the measured energy spectra, we fit the energy spectra with a simple three-source parameterization corresponding to the superposition of three Maxwellian distributions centered at velocities v_i and characterized by temperature parameters T_i:

$$\frac{d^2P}{dEd\Omega} = \sum_{i=1}^{3}\sigma_i(E,\theta) = \sum_{i=1}^{3} N_i\sqrt{E-V_C}\,e^{\frac{-\left(E-V_C+E_i-2\sqrt{E_i(E-V_C)}\cos\theta\right)}{T_i}}, \qquad (4)$$

where

$$E_i = \tfrac{1}{2}mv_i^2 \qquad (5)$$

is the energy of a particle at rest in source i. The parameter V_C is introduced to roughly account for Coulomb repulsion from a heavy charge assumed, for simplicity, at rest in the laboratory system [9,17]. Fits obtained with this parametrization are shown as solid curves in figure 3. The fits allow estimates of the relative contributions from fast projectile-like sources and intermediate-velocity "nonequilibrium" sources. In order to provide a more quantitative measure of the selectivity of the impact parameter filter based upon the charged particle multiplicity, we have fitted the multiplicity selected energy spectra of representative complex particles (He, Li, Be, C) with equations 4-5 and determined the relative contribution, $\sigma_{proj}/\sigma_{tot}$, of the projectile-like source to the total particle yield. This contribution was evaluated by integrating the respective sources over all angles and energies:

$$\sigma_{proj} = \iint \sigma_1(E,\theta)dEd\Omega \qquad (6)$$

$$\sigma_{tot} = \sum_{i=1}^{3} \iint \sigma_i(E,\theta) dE d\Omega \qquad (7)$$

Figure 4 shows ratios $\sigma_{proj}/\sigma_{tot}$, extracted from the energy spectra of He, Li, Be and C nuclei selected by different cuts on charged particle multiplicity for the ^{36}Ar+^{197}Au reactions at E/A=110 MeV. For illustration, a scale of the reduced impact parameter $\hat{b}(N_C)$ and a pictorial illustration of the geometric overlap between projectile and target nuclei are included in the figure. While such a simplistic graphic visualization must not be taken too seriously, it nevertheless illustrates that complete overlap between projectile and target nuclei is only achieved for relatively small impact parameters, representing less than 10% of the total reaction cross section. Even in such a naive geometrical picture, some emission from projectile-like sources must be expected down to impact parameters of $\hat{b}$=0.4. These simple expectations are fulfilled rather nicely for the emission of intermediate mass fragments for which projectile-like contributions are strongly suppressed at large multiplicities (small impact parameters). The suppression of projectile- like contributions is more effective for heavier (e.g. carbon nuclei) than for lighter particles (e.g. α-particles). In fact, the emission of fast α-particles does not follow the simple trends expected from simple geometrical arguments. Possibly α-particle emission already sets in at the early contact phase of the reaction and cannot be described by a simple participant-spectator picture.

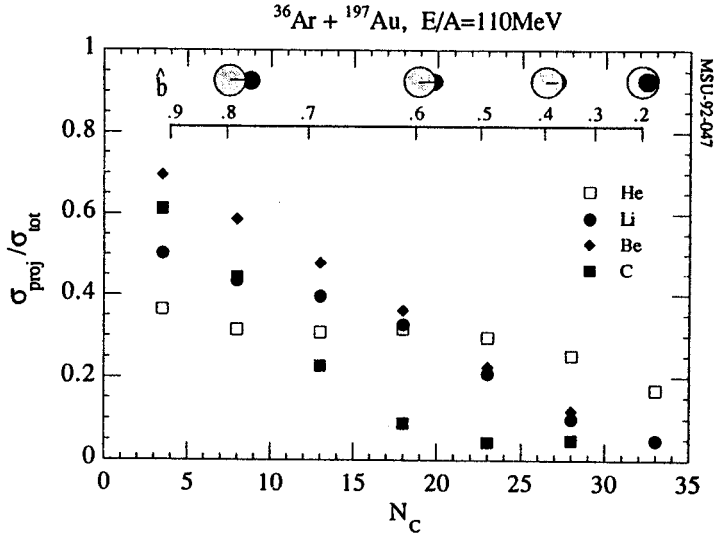

Figure 4: Relative contribution of projectile-like source extracted from the energy spectra of He, Li, Be and C nuclei selected by different cuts on charged particle multiplicity for ^{36}Ar+^{197}Au collisions at E/A=110 MeV. A scale of the reduced impact parameter $\hat{b}(N_C)$ and a pictorial illustration of the geometric overlap between projectile and target nuclei are included.

In order to compare of the effects of different impact parameter filters on the shapes of the energy spectra at forward angles, we have analyzed the energy spectra of particles detected in rings 1 and 2 (θ=9°-23°) and determined the "fast-particle fraction", $\sigma(v > \frac{1}{2} v_p)/\sigma_{tot}$, defined as the fraction of particles detected in rings 1 and 2 with velocities larger than half the projectile velocity. This simple quantity provides qualitatively similar insight as the quantity $\sigma_{proj}/\sigma_{tot}$ obtained from the moving source decomposition, but without necessitating cumbersome multi-parameter fits with Eq. 4.

Fast-particle fractions extracted for various cuts on impact parameter are shown in figure 5. Individual panels show the fast-particle fractions for He, Li, Be and C nuclei, and different symbols depict results obtained by different impact parameter filters. The fast-particle fractions are monotonic functions of the reduced impact parameter. The suppression of fast particles for cuts on small impact parameters is particularly effective for beryllium and carbon nuclei. The suppression of fast particles is less effective for α-particles. These qualitative observations are consistent with the results obtained with the moving source decomposition shown in figure 4. For impact parameters $\hat{b}$<0.6, all three impact parameter filters produce rather consistent fast-particle fractions. For intermediate and small impact parameters ($\hat{b}$<0.6), filters constructed from N_C, E_t, and Z_y appear to provide comparable resolution. Slightly better suppressions of the fast-particle fractions can be obtained by employing triple cuts on values of the impact parameters reconstructed from N_C, E_t, and Z_y (see star-shaped points).

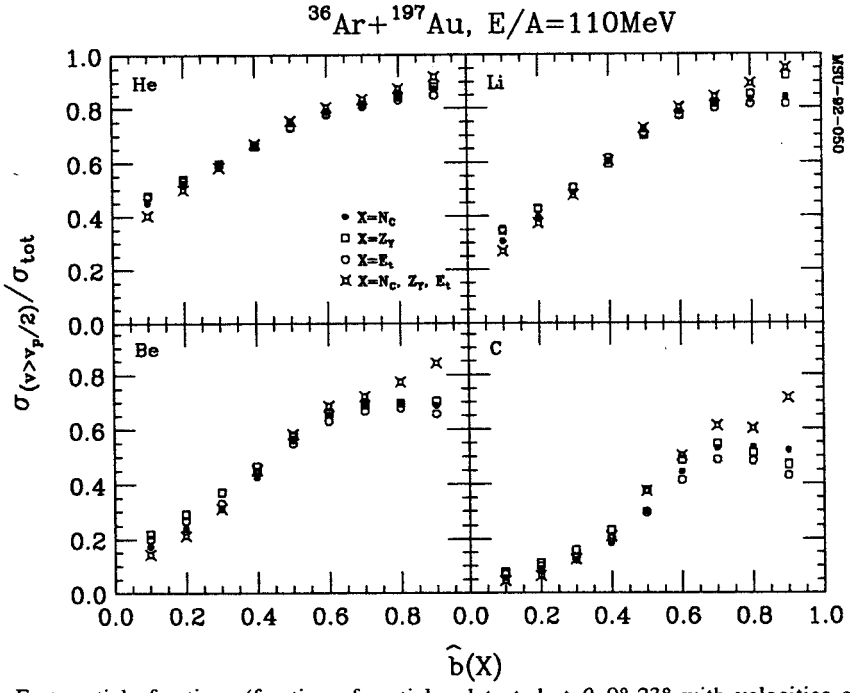

Figure 5: Fast-particle fractions (fraction of particles detected at θ=9°-23° with velocities greater than half the beam velocity) for ^{36}Ar+ ^{197}Au collisions at E/A=110 MeV. Solid points, open squares and open circles depict values determined for narrow cuts on the reduced impact parameters determined from N_C, E_t, and Z_y; star-shaped points represent simultaneous cuts on $\hat{b}(N_C)$, $\hat{b}(E_t)$, and $\hat{b}(Z_y)$.

For larger impact parameters, however, the differences between the various techniques become more significant. Such differences may be caused by statistical fluctuations of the quantities N_C, E_t, and Z_y. The relative magnitude of these fluctuations should be largest for peripheral collisions which are characterized by small mean values $\langle N_C \rangle$, $\langle E_t \rangle$, and $\langle Z_y \rangle$. As a consequence, selections of large impact parameters may be associated with larger uncertainties than selections of smaller impact parameters.

In conclusion, we have explored the selection of impact parameters via impact parameter filters based upon the detected charged particle multiplicity N_C, the transverse energy E_t, the intermediate rapidity charge Z_y, and the identified hydrogen multiplicity N_1 (which is the complement of Z_{bound}, [7]). All of these quantities display some sensitivity to the impact parameter. By applying a simple geometric prescription for the construction of a reduced impact parameter scale, quantitative comparisons of the various impact parameter scales were performed. Slightly improved selection of central collisions can be obtained by the use of multi-dimensional gates placed on different observables. In this regard, the future use of instruments capable of detecting neutral and charged particle observables in 4π geometry appears particularly promising.

a. Chalk River Laboratories, Chalk River, Ontario K0J 1J0, Canada
b. Lawrence Berkeley Laboratory, University of California, Berkeley, CA 94720
c. National Laboratory for High Energy Physics, 1-1 Oho, Tsukuba, Ibaraki 305, Japan
d. Indiana University Cyclotron Facility and Department of Chemistry, Indiana University, Bloomington, IN 47405
e. Brookhaven National Laboratory, Upton, Long Island, NY 11973

References

1. M.B. Tsang et al., Phys. Rev. C **40**, 1685 (1989).
2. R. Stock, Phys. Reports. **135**, 259 (1986).
3. H. Stöcker and W. Greiner, Phys. Reports **137**, 277 (1986).
4. C. Cavata et al., Phys. Rev. C **42**, 1760 (1990).
5. H.G. Ritter, Nucl. Phys. **A488**, 651c (1988).
6. C.A. Ogilvie et al, Phys. Rev. C **40**, 654 (1989).
7. J. Hubele et al., Z. Phys. **A340**, 263 (1991).
8. J. Galin, Nucl. Phys. **A447**, 519c (1985).
9. T.C. Awes et al., Phys. Rev. C **24**, 89 (1981).
10. Z. Chen et al., Nucl. Phys. **A473**, 564 (1987).
11. M.B. Tsang et al., Phys. Lett. B **220**, 492 (1989).
12. M. Morjean, et al., Phys. Lett. B **203**, 215 (1988).
13. R.T. de Souza et al., Nucl. Instr. and Meth. **A295**, 109 (1990).
14. M.B. Tsang et al., Phys. Rev. C **44**, 2065 (1991).
15. L. Phair et al., Nucl. Phys. **A548**, 489 (1992).
16. Y.D. Kim et al., Phys. Rev. C **45**, 338 (1992).
17. C.B. Chitwood et al., Phys. Rev. C **34**, 858 (1986).

IMPACT PARAMETER TAGGED LIGHT CHARGED PARTICLE EMISSION AT 25, 35 and 100 MeV/u

R. Vandenbosch[a], D. Bowman, G. Cren, M. Chartier, R. de Souza[b], J. Dinius, A. Elmaani[a], D. Fox[b], K. Gelbke, W. Hsi, C.E. Hyde-Wright[a], W. Jiang[a], W. Lynch, T. Moore[b], G. Peaslee, D.J. Prindle[a], C. Schwarz, Alejandro Sanzogni[a], M.-B. Tsang, and C. Williams

The mechanism for producing pre-equilibrium complex fragments in heavy ion collisions is not well understood. This is particularly true for more central collisions where prompt and sequential decays of projectile-like particles do not contribute. At low bombarding energies, complex particles are primarily limited to particles with masses 2–4. At higher bombarding energies considerably larger complex particles are produced in appreciable yield.

An important aspect of any reaction process is the impact parameter dependence. Characterization of impact parameter on an event-by-event basis is difficult, particularly for central collisions where the energy deposition for a wide range of impact parameters is similar. We have shown that it is possible to use the angular momentum dependence of evaporation-fission competition to generate tags for the most and less central impact parameters within the general class of fusion-like impact parameters. Using this technique we have shown that at 13.5 MeV/u the pre-equilibrium proton multiplicity falls off with increasing impact parameter while the ratio of pre-equilibrium complex particle to proton multiplicity increases with increasing impact parameter. In the present experiment we extend this study to higher bombarding energies and to coincidence detection of two or more light charged particles.

We used the MSU Miniball detector [1] to measure charged particle yields in 25 MeV/u ^{16}O and 35 MeV/u & 100 MeV/u ^{14}N on Au, Sm, Ta, and Tb targets. The most forward Miniball ring was replaced with an array of Si (E,veto) telescopes to measure coincident evaporation residues. In each of the remaining rings, one Miniball element was replaced with an Ion Chamber-Si-CsI (IC) telescope. We used the ion chambers primarily to measure the coincident fission fragments.

From the information obtained in this experiment we will also be able to address some other issues. One of the current topics for these intermediate energy heavy-ion induced reactions is the probe of nuclear matter properties via particle interferometry, or small-angle particle-particle correlations. The major driving forces for these correlation measurements are the emission space-time extent of the particle pair used to construct these correlations [2]. We intend to use relative momentum and reduced velocity correlation functions, respectively, to characterize the mean emission lifetime for light charged particles (LCP) and intermediate mass fragments (IMF). Our evaporation residue and fission tags will allow us to compare results for the most and less central collisions as described above.

The study of the evolution of the emission timescales over a wide range of excitation energies (25–100 MeV/u) will be used to look for a change in the emission mechanism. We are particularly interested in the transition from fusion-like reactions, which occur on a timescale of hundreds of fm/c, to nuclear breakup, occurring on timescales of a few fm/c.

In addition to small angle particle-particle correlations, we will compare the yields of complex particles with the coincidence yields of their (approximate) constituents, *e.g. d vs. pp*, ^{4}He vs *pt*, *dd*, etc, as a further guide to the emission mechanism.

The signal from each miniball detector was fanned out into 4 signals: 1 timing signal and 3 analog signals. The analog signals were integrated over 3 separate gates, defined relative to the constant fraction discriminator

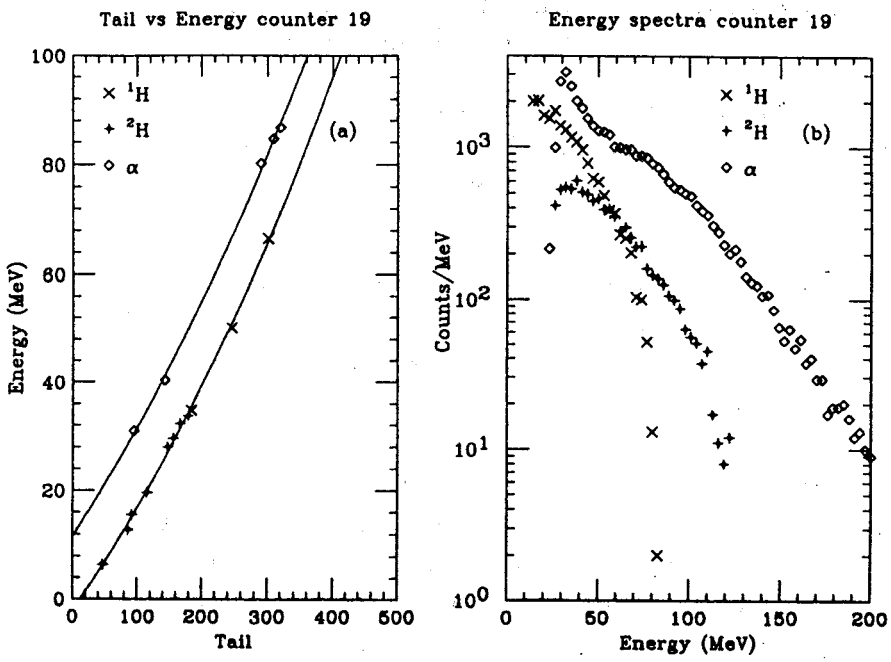

Figure 1: (a) Energy calibration points and the resulting quadratic fits for ^{1,2}H and ^{4}He measured in element 19 of the Miniball. (b) The corresponding energy spectra for ^{1,2}H, ^{4}He produced in the reaction of 25 MeV/u ^{16}O + ^{181}Ta and detected at $\theta_{lab} \approx 20°$.

output from the timing signal. The Fast gate has a 5 ns delay and 35 ns width. The Slow gate has a 200 ns delay and a 400 ns width. The Tail gate has a 2 μs delay and a 2 μs width.

We identified ^{1}H, ^{2}H, ^{3}H, ^{3}He, and ^{4}He by drawing 2-d gates in a plot of Tail *vs.* Slow, for each detector. This separation is possible because of the variable intensity and lifetime of the different light components in CsI as a function of ionization density. [3]

We have energy calibration runs with a ^{12}C beam on a polyethylene target. This produces two proton points from $p(^{12}C, p)^{12}C$ and $^{12}C^{*}$(4.4 MeV). Also we have a mixed deuteron and alpha beam on a polyethylene target which produce 2 proton points from $p(\alpha, p)\alpha$ and $p(d, p)d$. Deuteron points and α calibration points were produced by passing a mixed deuteron and alpha beam through a variable degrader and then scattering on a gold target. We separately calibrate the Tail *vs.* energy and Slow *vs.* energy. We use a common quadratic fit for energy vs light output for H isotopes and a separate quadratic fit for He isotopes. Sample calibration data and energy spectra from one element of the Miniball are shown in Fig. 1.

The forward array of Si telescopes was used to measure evaporation residues. The Miniball array of ten Ion-Chamber, Si, CsI telescopes from 19° to 150° was used to measure both evaporation residues and fission fragments. In the forward array, the first Si counter of each telescope stopped the residues, and the second counter vetoed quasi-elastic events. Residues were also identified by their correlated pulse height *vs.* time-of-flight distributions. Two of the Si telescopes were on a moveable arm, reaching from 3.5° to 15.5°. In the IC telescope, evaporation residues are identified by an ion-chamber signal in anticoincidence with the Si counter. In these same elements, the fission fragments were identified by coincidence between the Si and a large pulse height in the ion-chamber in anticoincidence with the CsI. Angular distributions of evaporation residues and fission fragments are shown in Fig. 2.

In Fig. 3 we present preliminary fission fragment relative azimuthal angular correlation results for the reaction 25 MeV/u ^{16}O + ^{181}Ta $\rightarrow FF1 + FF2$. $FF1$ is the trigger fission fragment measured in one of the

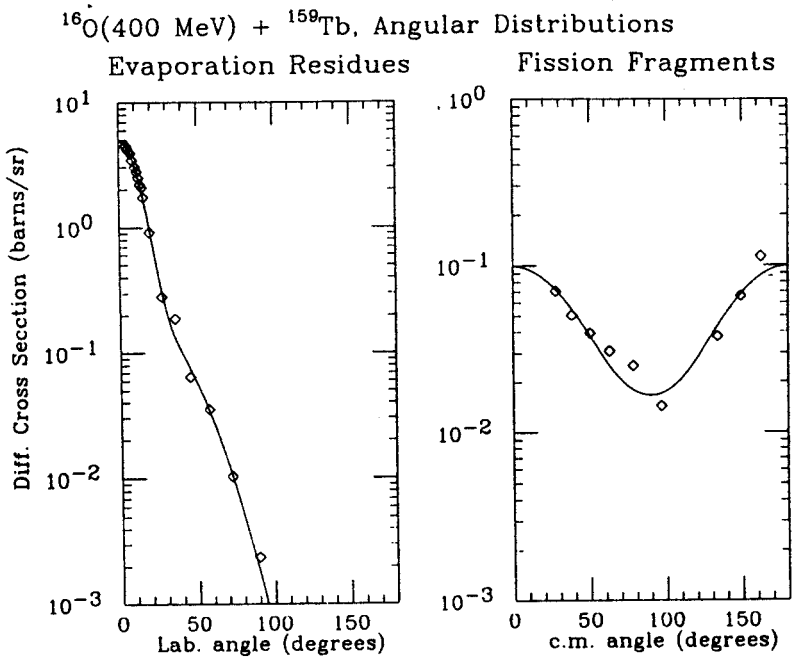

Figure 2: Evaporation residue and fission fragment angular distributions.

ion chambers and $FF2$ is the complementary fragment observed in coincidence in one of the regular Miniball plastic-CsI elements. The 180° preference clearly indicate the fission fragment co-planarity.

a. Nuclear Physics Lab, University of Washington, Seattle WA
b. Indiana University Cyclotron Facility, Indiana University, Bloomington IN.

References

1. R.T. Desouza *et al.*, Nucl. Inst. Meth. A **295**,109(1990).
2. A. Elmaani *et al.*, Phys Rev **C43** R2474 (1991), and W.G. Gong *et al.*, Phys. Rev. **C43** 1844 (1991).
3. R.S. Storey, W. Jack and A. Ward. Proc. Phys. Soc. 75 (1958) 72.

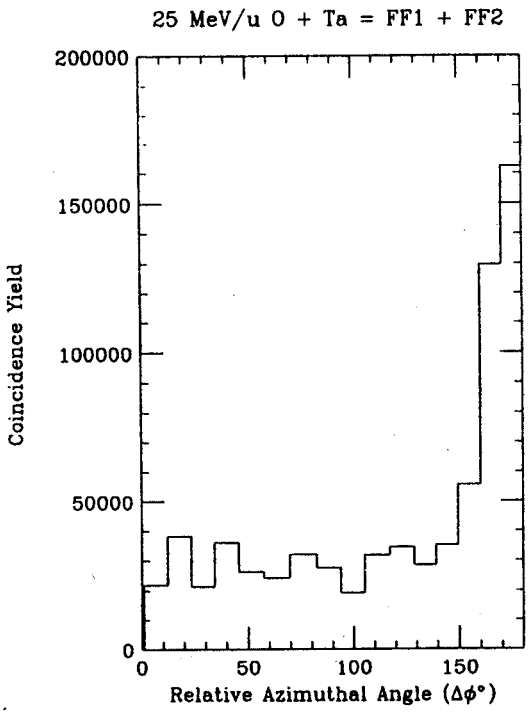

Figure 3: Azimuthal angular correlation for fission fragments detected in coincident events between an Ion Chamber and a Miniball Phoswich detector.

Emission temperatures from widely separated states in ^{14}N- and ^{129}Xe-induced reactions

C. Schwarz, W.G. Gong[a], N. Carlin[b], C.K. Gelbke, Y.D. Kim[c], W.G. Lynch, T. Murakami[d], G. Poggi[e], R.T. de Souza[f], M.B. Tsang, H.M. Xu[g], D.E. Fields[h], K. Kwiatkowski[f], V.E. Viola, Jr.[f], and S.J. Yennello[g]

To address questions concerning the statistical properties of hot nuclei, it is important to determine their temperature. By comparing the yield ratios of particle unstable states of emitted fragments with calculations one can extract an apparant temperature of the emission source. Until now, the relative populations of widely separated particle-unbound states have mainly been measured at forward angles for relatively light projectiles on heavy targets where contributions from the early nonequilibrated stages of the reaction predominate [1-9]. In this respect, it is interesting to extend emission temperature measurements to a variety of entrance channel mass asymmetries. We measured relative populations of widely separated states in ^{4}He, ^{5}Li, and ^{8}Be nuclei for ^{14}N+^{27}Al and ^{14}N+^{197}Au collisions at E/A=75 MeV and for ^{129}Xe+^{27}Al and ^{129}Xe+^{122}Sn collisions at E/A=31 MeV using the same detector geometry [10] Reactions induced by ^{14}N projectiles give rise to large contributions from the early nonequilibrated stages of the reactions and should, hence, be compared to previous measurements. For the ^{129}Xe+^{27}Al reaction, emission from nearly equilibrated composite systems dominates and the extraction of unbound state populations will provide a test case for emission temperatures from equilibrated systems. The breakup scenario for ^{129}Xe+^{122}Sn reactions is, at present, unknown.

The experiment was performed using ^{14}N and ^{129}Xe beams of E/A=75 MeV and of 31 MeV, respectively: the beam intensities were 5×10^{9} and 1×10^{8} ions per second, respectively. Light charged particles were detected with two ΔE-E detector arrays, consisting of 300-400 μm thick silicon ΔE-detectors and 10 cm long CsI(Tl) or NaI(Tl) E-detectors. The first array consisted of 37 Si-CsI(Tl) telescopes and was centered at polar and azimuthal angles of $\Theta = 25^{0}$ and $\Phi = 0^{0}$. Isotopic identification was achieved for hydrogen through beryllium isotopes. Representative software energy thresholds were 9, 12, and 13 MeV/nucleon for Z=2, 3, and 5 fragments, respectively. The second array, consisting of 13 Si-NaI(Tl) telescopes, was centered at $\Theta = 25^{0}$ and $\Phi = 90^{0}$. Isotopically identified p, d, t, ^{3}He, ^{4}He, ^{6}He, ^{6}Li, and ^{7}Li particles were detected with energy thresholds of 12, 14, 16, 35, 40, 45, 80, and 90 MeV, respectively.

Products from the decay of particle-unstable nuclei were detected as coincident particles and relative momentum spectra were accumulated. The coincidence yield can be decomposed into two parts, one results from the decay of particle unstable states, the other is largely determined by the available phase space. To remove the effects of detector thresholds and finite angular coverage, which influence both parts in similar fashion, we constructed the correlation function and parameterized the background correlation function. For our data analysis, we determined the sensitivity of the extracted coincidence yield to uncertainities of the background by choosing two extreme assumptions for this background [10].

Information about relative populations of states are obtained from the relative decay yields. The coincidence yield resulting from the decay of particle-unstable states can be approximated by a folding of the decay spectrum with the efficiency of the experimental apparatus for the detection of particle pairs resulting from the decay of specific particle-unstable nuclei [2]. For narrow, thermally populated states, the decay spectrum can be expressed as a Breit-Wigner formula multiplied by a Boltzmann factor; for broad states we used instead of the Breit-Wigner formula an one-level R-matrix formalism. The efficiency function is obtained from Monte-Carlo simulations, which take into account the kinetic energy spectra of the particle-unstable fragments, as well as the precise geometry and detector response and the angular straggling in the target [2]. For the calculation of the

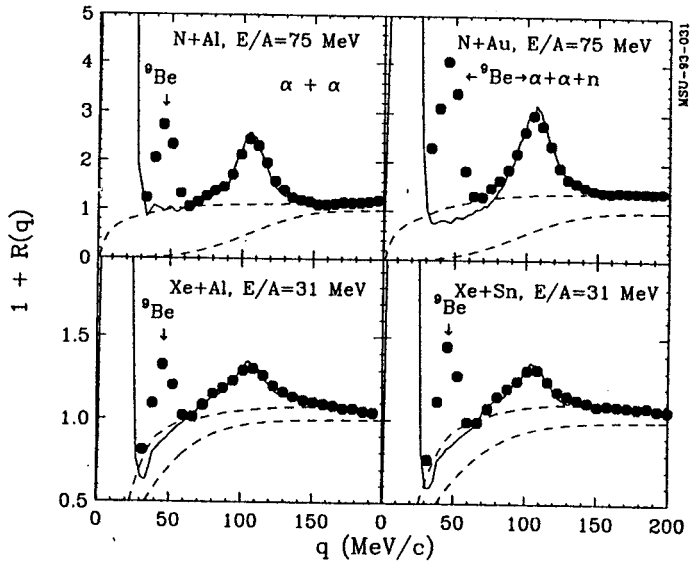

Figure 1: $\alpha - \alpha$ correlation functions for different reaction systems. The dashed lines are extreme bounds for the background correlation function. The solid line is a calculation with $T = 4$ MeV for the ^{14}N and $T = 3$ MeV for the ^{129}Xe-induced reactions assuming the minimum background correlation function. The peak at q=45 MeV/c is largely due to the decay of the 2.43 MeV state in ^{9}Be ($^9Be \rightarrow 2\alpha + n$); in addition, it contains contributions from the "ghost peak" of the ^{8}Be ground state (see Ref. 2 and references therein).

efficiency function, the ^{8}Be parent distribution was assumed to be given by the parameters that were used to describe the ^{7}Be cross sections.

Fig. 1 shows $\alpha - \alpha$ correlation functions. The peak at $q \approx 105$ MeV/c results from the decay of the 3.04 MeV state in ^{8}Be ($J^\pi = 2^+$, $\Gamma_{c.m.} = 1.5$, $\Gamma_\alpha/\Gamma = 1.00$). For the present investigation, the structures at lower relative momenta are not of interest, for a detailed discussion see Ref. [2]. To improve the agreement between calculated line shapes (solid lines in Fig. 1) and the data we have allowed the maximum background correlation shown as the upper dashed line, to exeed unity. For ^{129}Xe-induced reactions the peaks of correlation function due to the 2^+ state are only significantly smaller than for the ^{14}N-induced reactions.

The p-^{7}Li correlation functions are shown in Fig. 2. The first maximum at $q \approx 25$ MeV/c corresponds to the 17.64 MeV state in ^{8}Be ($J^\pi = 1^+$, $\Gamma_{c.m.} = 10.7$ keV, $\Gamma_p/\Gamma = 1.00$ [11]). Parameters for the other resonances were taken from Ref. [11]. We could not describe all these states assuming a thermal population of excited states in ^{8}Be and a background correlation function which increases monotonically with q. This may indicate a nonstatistical population of states. On the other hand structures could occur in the correlation function due to 3-body decays or decays to excited states in ^{7}Li. To explore this as a possible upper limit of the experimental background, we have explored hand-drawn dashed lines, which exceed unity, shown in Fig. 2 as extreme limits to the background.

Population ratios of widely separated states in ^{8}Be fragments (Fig. 1, 2) give similar results to analysed population ratios of widely separated states in ^{4}He- and ^{5}Li fragments. Here, we analysed the ratio between the ($J^\pi = 1^+$) state at 17.64 MeV, which decays in p and ^{7}Li, and the ($J^\pi = 2^+$) state at 3.04 MeV, which decays into two α-particles. Yields of the p-^{7}Li and α-α decay channels were integrated from q=18 MeV/c to 32 MeV/c and from q=65 MeV/c to 160 MeV/c, respectively. Consistent with the results for ^{4}He and ^{5}Li fragments, higher temperatures are observed for ^{14}N-induced reactions at the higher incident energy of E/A=75 MeV ($T = 4.9 \pm 0.9$ MeV for ^{14}N+^{27}Al and $T = 4.5 \pm 0.9$ MeV for ^{14}N+^{197}Au, respectively) and lower temperatures for ^{129}Xe-induced reactions at the lower incident energy of E/A=31 MeV ($T = 3.3 \pm 0.5$ MeV for ^{129}Xe+^{27}Al

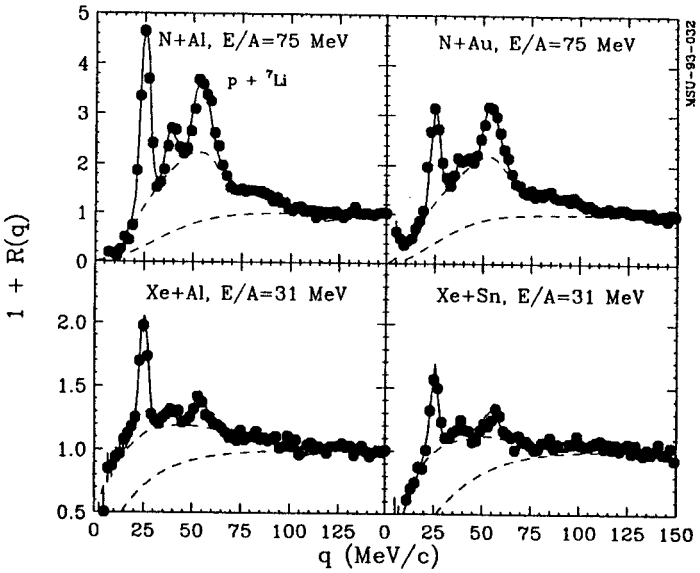

Figure 2: p-^{7}Li correlation functions for different reaction systems. The dashed lines are extreme bounds for the background correlation function. The solid line is a calculation with $T = 4$ MeV for the ^{14}N and $T = 3$ MeV for the ^{129}Xe-induced reactions assuming the maximum background correlation function.

and $T = 3.9 \pm 1.0$ MeV for ^{129}Xe+^{122}Sn, respectively).

A summary of all extracted emission temperatures is shown in Fig. 3. The uncertainties are due to extreme assumptions of the background correlation functions. Estimates of the range of emission temperatures consistent with these measurements are indicated by the dashed lines; for ^{129}Xe-induced reactions the average was taken over the ^{4}He and ^{8}Be fragments. Emission temperatures from the states discussed in this paper are expected to be robust with respect to distortions due to sequential feeding from heavier particle-unstable nuclei for temperatures less than 5 MeV [12]. The largest distortions were predicted for ^{4}He for which calculations at T=5 MeV predict populations corresponding to extracted temperatures which are about 0.5 MeV lower due to sequential decay.

Average emission temperatures extracted from the relative populations of widely separated states are T=4.3±0.2 MeV for ^{14}N+^{27}Al and T=4.1±0.2 MeV for ^{14}N+^{197}Au. These values are significantly smaller than the values of "kinetic temperature" parameters (T≈18-20 MeV) which characterize the slopes of the kinetic energy spectra of protons emitted at $\theta_{lab} \approx 25°$ [13]. The extracted emission temperatures are consistent with previous measurements. Their low values may be related to cooling due to expansion [14-16], to preequilibrium effects [8, 17-21], or both.

Average emission temperatures extracted for the ^{129}Xe-induced reactions were lower by about 1 MeV, T=3.1±0.2 MeV for ^{129}Xe+^{27}Al and T=3.5±0.3 MeV for ^{129}Xe+^{122}Sn (Fig. 3). For the ^{129}Xe+^{27}Al reaction, these temperatures are slightly smaller than the kinetic temperature parameters T≈4-6 MeV which characterize the energy spectra for protons [13]. The same is true for the ^{129}Xe+^{122}Sn reaction for which the extracted temperature is slightly smaller than the kinetic temperature (T≈4 MeV) which characterizes the emission of protons [13] from the projectile-like source which dominates emission at the angles of the present measurement. Previous investigations [22] have reported that the apparent temperatures of such spectra are considerably larger than the temperature of compound systems. These studies suggest that such backward angle proton spectra may still be contaminated by preequilibrium emission.

Within experimental errors, the emission temperatures extracted for the ^{129}Xe-induced reactions are

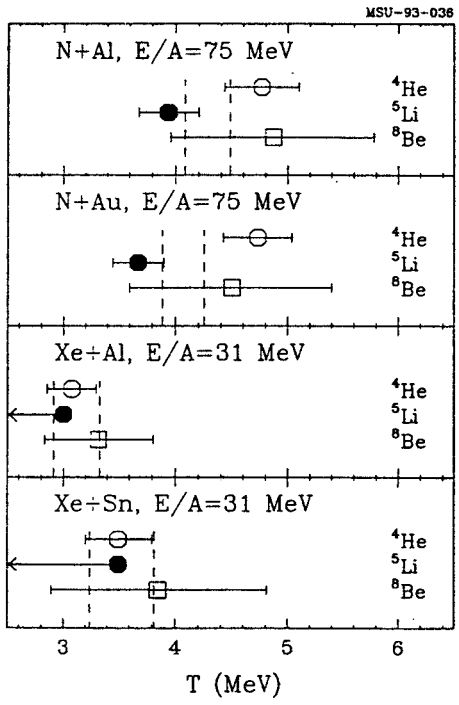

Figure 3: Extracted apparent temperatures from widely spaced levels of the fragments ^{4}He, ^{5}Li, and ^{8}Be. The uncertainties are due to the extreme assumptions of the background correlation functions indicated in Figs. 1 and 2. The fragment averaged temperature bounds are marked by dashed lines. (For ^{129}Xe-induced reactions the average was taken over the ^{4}He and ^{8}Be fragments.)

comparable (though slightly smaller in magnitude) to temperatures previously extracted from other reactions at comparable incident energies per nucleon in which large nonequilibrium contributions could not be excluded. For example, average emission temperatures of T=3-4 MeV were determined from the population of particle-unbound states of particles emitted at $\theta_{lab} \approx 38°$ in ^{14}N+^{nat}Ag reaction at E/A=35 MeV [7] and from the relative populations of particle-stable states in ^{32}S+^{nat}Ag and (and $\theta_{lab} \approx 20°$-$50°$) [23].

The emission temperatures determined for ^{129}Xe+^{27}Al are also smaller than temperatures expected for equilibrated fusion-like residues. Linear momentum transfer (LMT) systematics [24] predict a ratio of the linear momentum transfer to the initial beam momentum of $p_{\|}/p_{beam} = 0.73$ and, as determined from an incomplete fusion scenario for the ^{129}Xe+^{27}Al reaction, an excitation energy of E*/A=3.4 MeV. Assuming a level density parameter of a=A/8 MeV^{-1}, this provides a compound nucleus temperature of 5.2 MeV, which is significantly larger than the observed emission temperature. This estimate of excitation energy from an incomplete fusion ansatz is an upper limit, however, since all the missing beam momentum is assumed to be carried away by particles moving with the beam velocity and with zero transverse momenta.

BUU transport equations calculations, which do account for particle emission at non-zero emission angles, predict residue temperatures of about 3 MeV for calculations of the similar ^{40}Ar + ^{124}Sn system, assuming a soft EOS at low density [17]. Further measurements are needed to determine whether such calculations can also reproduce the energy spectra or other observables in this reaction.

a. Nuclear Science Division, Lawrence Berkeley Laboratory, Berkeley, CA 94720, USA.

b. Instituto de Física, Universidade de São Paulo, C. Postal 20516, CEP 01498, São Paulo, Brazil.
c. National Lab. for High Energy Physics (KEK), Department of Physics, 1-1 Oho, Tsukuba, Ibaraki 305, Japan.
d. Department of Physics, Kyoto University, Kyoto 606, Japan.
e. Dipartimento di Fisica dell'Universitá and INFN, Largo Enrico Fermi 2, 50125 Firenze, Italy.
f. Dept. of Chemistry, Indiana Univ. Cyclotron Facility, Indiana Univ., Bloomington, Indiana 47405, USA.
g. Cyclotron Institute, Texas A&M University, College Station, Texas 77843, USA.
h. P-2 Division, Los Alamos National Laboratory Los Alamos, New Mexico 87545.

References

1. J. Pochodzalla, W. A. Friedman, C. K. Gelbke, W. G. Lynch, M. Maier, D. Ardouin, H. Delagrange, H. Doubre, C. Grégoire, A. Kyanowski, W. Mittig, A. Péghaire, J. Péter, F. Saint-Laurent, Y. P. Viyogi, B. Zwieglinski, G. Bizard, F. Lefébvres, B. Tamain, and J. Québert, Phys. Lett. B **161**, 275 (1985).
2. J. Pochodzalla, C. K. Gelbke, W. G. Lynch, M. Maier, D. Ardouin, H. Delagrange, H. Doubre, C. Grégoire, A. Kyanowski, W. Mittig, A. Péghaire, J. Péter, F. Saint-Laurent, B. Zwieglinski, G. Bizard, F. Lefébvres, B. Tamain, J. Québert, Y. P. Viyogi, W. A. Friedman, and D. H. Boal, Phys. Rev. C **35**, 1695 (1987).
3. Z. Chen, C. K. Gelbke, J. Pochodzalla, C. B. Chitwoood, D. J. Fields, W. G. Gong, W. G. Lynch, and M. B. Tsang, Nucl. Phys. **A473**, 564 (1987).
4. Z. Chen, C. K. Gelbke, W. G. Gong, Y. D. Kim, W. G. Lynch, M. R. Maier, J. Pochodzalla, M. B. Tsang, F. Saint-Laurent, D. Ardouin, H. Delagrange, H. Doubre, J. Kasagi, A. Kyanowski, A. Péghaire, J. Péter, E. Rosato, G. Bizard, F. Lefébvres, B. Tamain, J. Québert, and Y. P. Viyogi, Phys. Rev. C **36**, 2297 (1987).
5. Z. Chen, C. K. Gelbke, W. G. Gong, Y. D. Kim, W. G. Lynch, M. R. Maier, J. Pochodzalla, M. B. Tsang, F. Saint-Laurent, D. Ardouin, H. Delagrange, H. Doubre, J. Kasagi, A. Kyanowski, A. Péghaire, J. Péter, E. Rosato, G. Bizard, F. Lefébvres, B. Tamain, J. Québert, and Y. P. Viyogi, Phys. Lett. B **199**, 171 (1987).
6. F. Saint-Laurent, A. Kyanowski, , D. Ardouin, H. Delagrange, H. Doubre, C. Grégoire, W. Mittig, A. Péghaire, J. Péter, G. Bizard, F. Lefébvres, B.Tamain, J. Québert, Y. P. Viyogi, J. Pochodzalla, C. K. Gelbke, W. G. Lynch, and M. Maier, Phys. Lett. B **202**, 190 (1988).
7. T. K. Nayak, T. Murakami, W. G. Lynch, K. Swartz, D. J. Fields, C. K. Gelbke, Y. D. Kim, J. Pochodzalla, M. B. Tsang, H. M. Xu, F. Zhu, and K. Kwiatkowski, Phys. Rev. C **45**, 132 (1992).
8. G. J. Kunde, J. Pochodzalla, J. Aichelin, E. Berdermann, B. Berthier, C. Cerruti, C. K. Gelbke, J. Hubele, P. Kreutz, S. Leray, R. Lucas, U. Lynen, U. Milkau, W. F. J. Müller, C. Ngô, C. H. Pinkenburg, G. Raciti, H. Sann, and W. Trautmann, Phys. Lett. B **272**, 202 (1991).
9. H. Xi, W. Zhan, Y. Zhu, Z. Guo, X. Hu, G. Liu, J. Zhou, S. Yin, Y. Zhao, Z. Wei, and E. Fan, Nuc. Phys. **A552**, 281 (1993).
10. C. Schwarz, W. G. Gong, N. Carlin, C. K. Gelbke, Y. D. Kim, W. G. Lynch, T. Murakami, G. Poggi, R. T. de Souza, M. B. Tsang, H. M. Xu, D. E. Fields, K. Kwiatkowski, V. E. Viola, Jr., and S. J. Yennello, submitted to Phys. Rev. C .
11. F. Ajzenberg-Selove, Nucl. Phys. **A490**, 1 (1988).
12. Z. Chen and C. K. Gelbke, Phys. Rev. C **38**, 2630 (1988).
13. W. G. Gong, C. K. Gelbke, W. Bauer, N. Carlin, R. T. de Souza, Y. D. Kim, W. G. Lynch, T. Murakami, G. Poggi, D. P. Sanderson, M. B. Tsang, H. M. Xu, D. J. Fields, K. Kwiatkowski, R. Planeta, V. E. Viola, S. J. Yennello, and S. Pratt, Phys. Rev. C **43**, 1804 (1991).
14. H. W. Barz, J. P. Bondorf, and H. Schulz, Phys. Lett. B **184**, 125 (1987).
15. W. A. Friedman, Phys. Rev. Lett. **60**, 2125 (1988).
16. D. H. E. Gross and H. Massmann, Nucl. Phys. **A471**, 339c (1987).
17. H. M. Xu, P. Danielewicz, and W. G. Lynch, Phys. Lett. B **299**, 199 (1992).
18. C. Schwarz, H. Fuchs, H. Homeyer, K. Möhring, T. Schmidt, A. Siwek, A. Sourell, W. Terlau, and A. Budzanowski, Phys. Lett. B **279**, 223 (1992), Z. Phys. A **345**, 29
19. K. Möhring, T. Srokowski, and D. H. E. Gross, Nucl. Phys. **A533**, 333 (1991).
20. D. H. Boal and J. N. Glosli, Phys. Rev. C **37**, 91 (1988).
21. D. H. Boal and J. N. Glosli, Phys. Rev. C **42**, R502 (1990).
22. V. E. Viola, Nucl. Phys. **A471**, 53c (1987).
23. H. M. Xu, W. G. Lynch, C. K. Gelbke, M. B. Tsang, D. J. Fields, M. R. Maier, D. J. Morrissey, T. K. Nayak, J. Pochodzalla, D. G. Sarantites, L. G. Sobotka, M. L. Halbert, and D. C. Hensley, Phys. Rev. C **40**, 186 (1989).
24. M. Fatyga, K. Kwiatkowski, V. E. Viola, C. B. Chitwood, D. J. Fields, C. K. Gelbke, W. G. Lynch, J. Pochodzalla, M. B. Tsang, and M. Blann, Phys. Rev. Lett. **55**, 1376 (1985).

COMPETITION BETWEEN MULTIFRAGMENTATION AND FUSION-FISSION

E.E. Gualtieri, J. Yee, D. Craig, S. Hannuschke, R. Lacey[a], T. Li, W.J. Llope, A. Nadasen[b], E. Norbeck[c], R. Pak, A. Vander Molen, G. D. Westfall, J.S. Winfield and S.J. Yennello

New experimental results have established important changes in the reaction mechanisms between two nuclei with increasing (intermediate) beam energies. In particular, fusion-fission processes have been shown to disappear in Ar + Th reactions as beam energy increases, as measured using fission fragment opening angles [1]. The time scale of fragment emission has also been shown to change significantly as beam energy changes from 35 MeV/n to 45 MeV/n [2].

To measure such changes in reaction mechanisms, the MSU 4π array has been equipped with Multi-Wire Proportional Counters (MWPC's). These devices provide the position of outgoing fission fragments, and, to some extent, that of other heavy particles [3]. Using these newly installed devices, we studied the system $^{40}Ar + ^{232}Th$, in the energy range 15 MeV/n to 115 MeV/n, with the goal of understanding the contribution of multifragmentation and fusion-fission as the dominant reaction mechanisms in collisions in this energy range.

We discuss here events in which two particles were detected in the MWPC's, and have made gates on events based on their opening angle. We then looked for correlations between opening angle and global observables measured in the 4π array. In the data shown here it is required that the two particles detected be coplanar with the target, i.e. are separated in the azimuthal angle by $180° \pm 10°$.

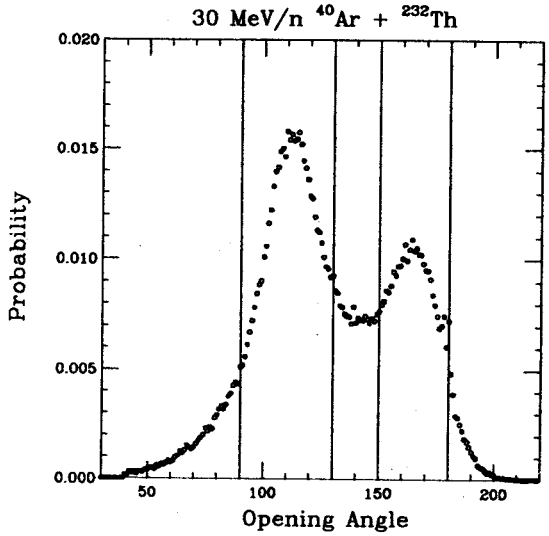

Figure 1: Opening angle distribution with gates - 30 MeV/n.

Shown in Fig. 1. is the distribution of opening angles from events for the 30 MeV/n system. Gates have been drawn around the peak at 110°, and around the peak at 165°. The peak at larger angles is generally thought to arise from peripheral, low momentum transfer collisions in which the target is caused to fission. The other peak is believed to result from more central, high momentum transfer collisions in which the target and projectile fuse and subsequently fission.

To investigate this, we have plotted the Z-distributions for events in each of these two peaks as shown in

Fig. 2a and 2b. Figure 2a shows that the distribution coming from the low momentum transfer peak has a higher proportion of high-Z particles relative to the distribution from the high momentum transfer peak. This runs contrary to previous measurements which show that, at 31 MeV/n, target-fission fragments from this system are somewhat larger than fusion-fission fragments [1],meaning fewer smaller fragments would be left behind to be detected.

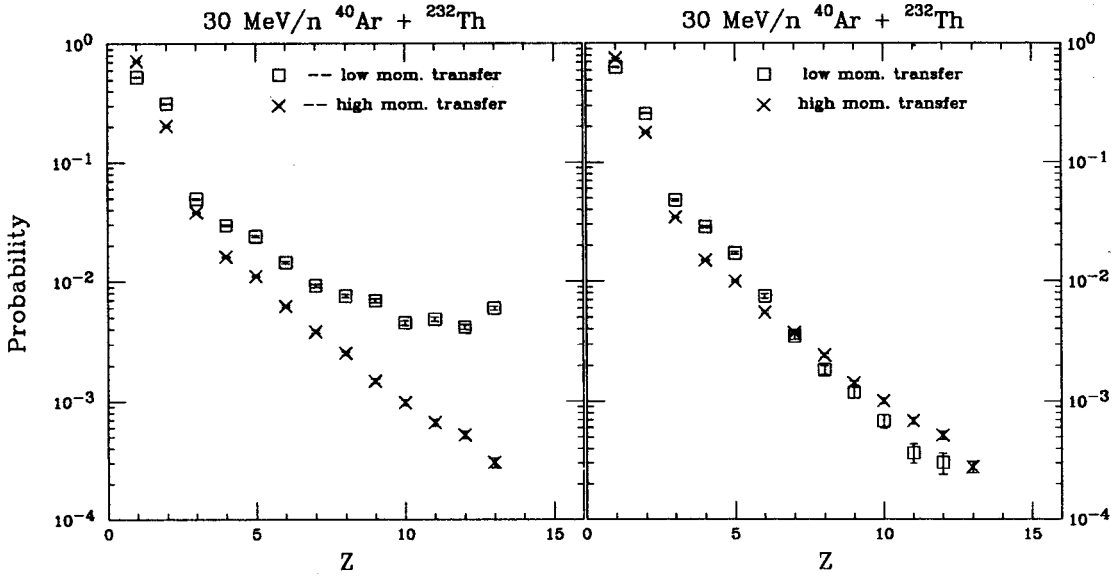

Figure 2: Z-distributions with and without forward array contributions.

However, if particles detected in the forward array of phoswiches, which covers polar angles from 7° to 18° are removed from the distributions (Fig. 2b) we see that the distribution for the target-fission events is now somewhat steeper than that of the fusion-fission events. This provides evidence that the high-Z particles seen in the low momentum transfer events result from the break up of the projectile which interacts peripherally with the target.

Using the same opening angle gates, we plot several variables generally considered to be correlated with impact parameter (Fig. 3), where maximal values of these variables indicate more central collisions for reactions in this energy range. The distributions of total multiplicity of detected charged particles, (N_c), in Fig. 3b, indicate that the reactions in the high momentum transfer gate are more central than those in the low momentum transfer gate.

The relative postions of the distributions of mid-rapidity charge (Z_{mr}) in Fig. 3c also indicate this, however, the distinction is less clear than with N_c. The same is true of the transverse momentum (P_t) distributions (Fig. 3d). The distribution of IMF multiplicity (Fig. 3a) shows almost no difference between events from the two gates, however, for the reasons described above, the distribution from the low momentum transfer gate is distorted.

In the 15 MeV/n system (Fig 4), it is difficult to make any distinction between the gated distributions of N_c, Z_{mr}, and P_t. The distributions of N_{imf} show some difference that would indicate that the low-momentum transfer events contain more IMF's, but again this variable is suspect.

In the 115 MeV/n system (Fig 5), we see a drastic difference between all of the distributions of centrality variables, all of which suggest that the high momentum transfer events are more central. The large values attained by the peaks of the distributions of N_c and Z_{mr} also indicate that multifragmention has replaced fusion-fission.

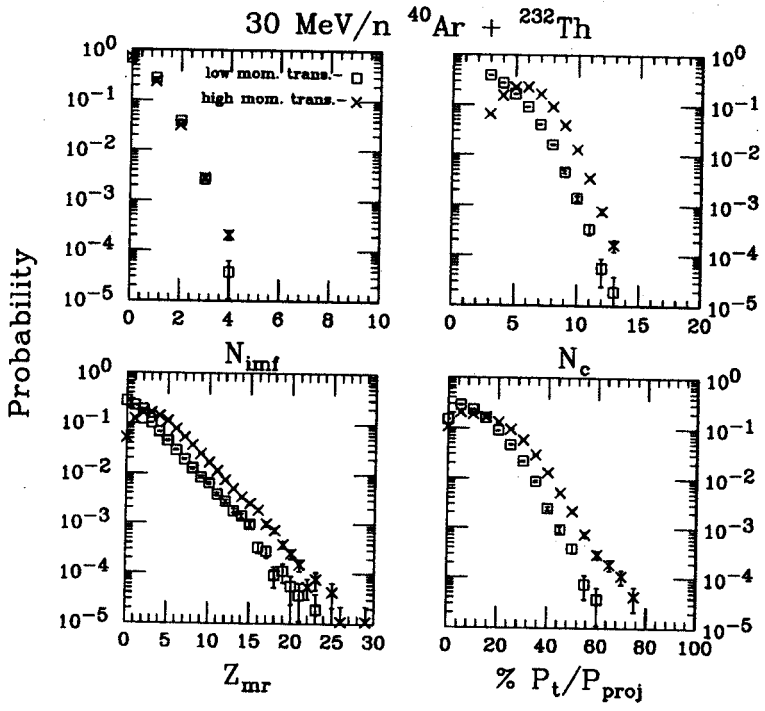

Figure 3: Distributions of centrality variables – 30 MeV/n

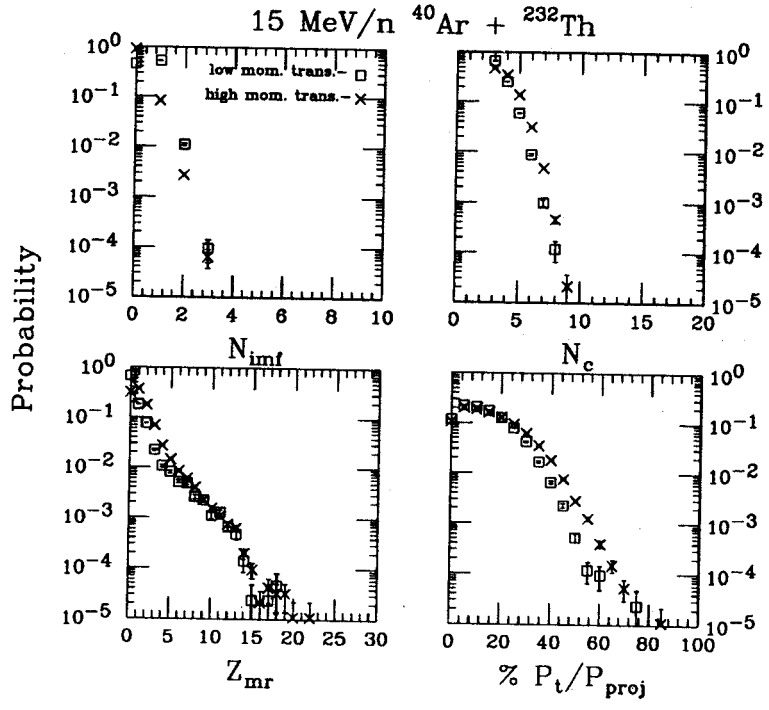

Figure 4: Distributions of centrality variables – 15 MeV/n

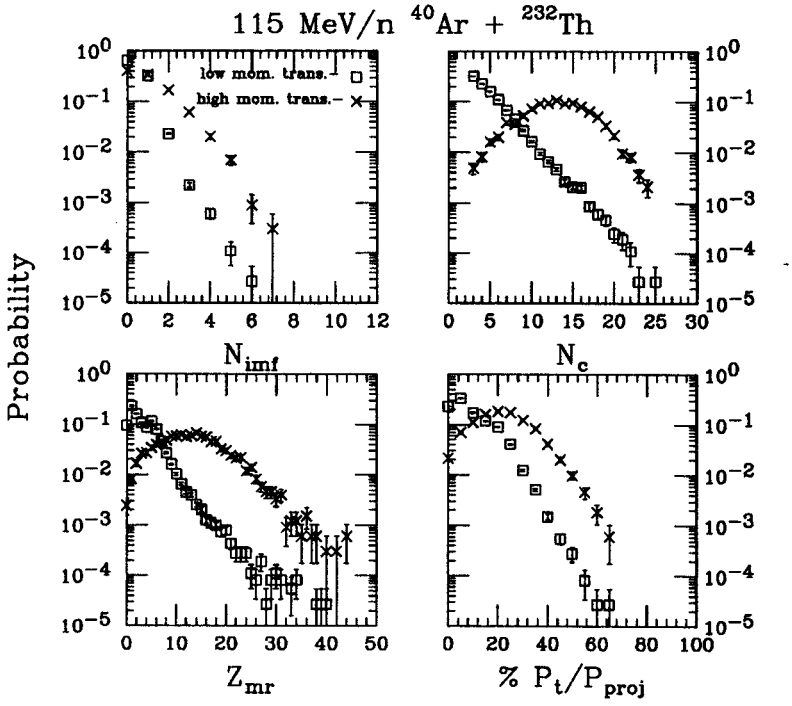

Figure 5: Distributions of centrality variables – 115 MeV/n

In conclusion, we have seen from our 30 MeV/n system that there is some correlation between opening angle and centrality variables, and found evidence which could confirm that the target fission fragments are larger than the fusion-fission fragments.

The data from the 15 MeV/n system show little correlation between centrality variables and opening angle, while the 115 MeV/n system shows a strong correlation and indicates that multifragmentation has taken over.

a. Department of Chemistry, State University of New York at Stony Brook, Stony Brook NY 11794-3400
b. Department of Physics, University of Michigan at Dearborn, Dearborn, MI 48128
c. Department of Physics and Astronomy, University of Iowa, Iowa City, Iowa 52242

References

1. M. Conjeaud et. al.,Phys. Lett. B159,244 (1985).
2. D.A. Cebra et. al., Phys. Rev. Lett. 64, 2246 (1990).
3. MSU/NSCL Annual Report (1991).

MASS DEPENDENCE OF THE DISAPPEARANCE OF FLOW

G.D. Westfall, W. Bauer, D. Craig, M. Cronqvist, E. Gualtieri, S. Hannuschke, D. Klakow, T. Li, T. Reposeur, A.M. Vander Molen, W.K. Wilson, J.S. Winfield, J. Yee, S.J. Yennello, R. Lacey[a], A. Elmaani[a], J. Lauret[a], A. Nadasen[b], and E.Norbeck[c]

The study of global collective variables in nucleus-nucleus collisions can provide information about the nuclear equation of state (EOS)[1,2]. In recent years much emphasis has been placed on the study of collective flow and several groups have performed experiments to study its disappearance[3-8]. The disappearance of collective flow is predicted to occur at an incident energy (termed the balance energy, E_{bal}[3]) corresponding to the point where the attractive scattering, dominant at incident energies around 10 MeV/nucleon, balances the repulsive interactions observed at energies around 400 MeV/nucleon[3,9,10]. Because the magnitude of parameters of the EOS can be related to the dominance of repulsive or attractive scattering, there is great value in the determination of E_{bal}. We report here results from the the first systematic study of the disappearance of flow in nucleus-nucleus collisions. We present new data for the C+C, Ne+Al, Ar+Sc, and Kr+Nb systems which show that E_{bal} scales as $A^{-1/3}$, where A is the mass of the combined projectile-target system. The general trend of this result is reproduced by Boltzmann Uehling Uehlenbeck (BUU) model calculations confirming the interpretation of E_{bal}.

We interpret the scaling of E_{bal} with mass to be the result of a competition between the dominantly attractive mean field interaction which scales as the surface area, $A^{2/3}$, and the dominantly repulsive nucleon-nucleon scattering which scales as the volume of the two nuclei, A.

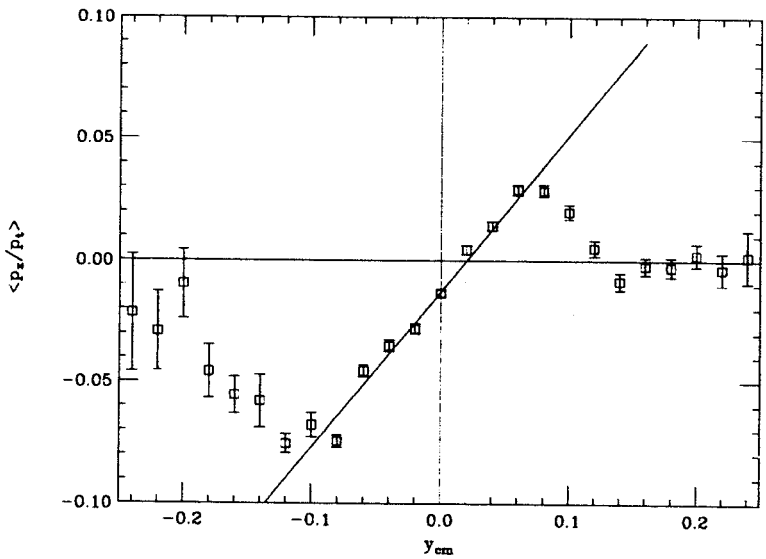

Figure 1: Average transverse momentum in the reaction plane divided by the total transverse momentum versus the center of mass rapidity for He fragments from 35 MeV/nucleon Kr+Nb. The solid line is fit over the region of $-0.08 \leq y_{cm} \leq 0.08$.

The present measurements were carried out with the MSU 4π Array[11] at the National Superconducting Cyclotron Laboratory (NSCL) using beams from the K1200 cyclotron. The 4π Array consists of a main ball of 170 phoswich counters (arranged in 20 hexagonal and 10 pentagonal subarrays) covering angles from 23° to 157° and a forward array of 45 phoswich counters covering angles from 7° to 18°. The 30 Bragg curve counters

installed in front of the hexagonal and pentagonal sub-arrays were operated in ion chamber mode (in three different experiments) with pressures of 500, 250, and 100 torr of P5 (95% argon, 5% methane), CF_4, and C_2F_6 gases respectively. The hexagonal anodes of the five most forward Bragg curve counters are segmented creating a total of 55 separate ΔE gas counters.

The Bragg curve counters served as ΔE detectors for charged particles that stopped in the fast plastic scintillator of the main ball. Consequently, the Array was capable of detecting charged fragments from Z=1 to Z=12. Low energy thresholds (in each experiment) were $\approx$17 MeV/nucleon, $\approx$3 MeV/nucleon and $\approx$5 Mev/nucleon for fragments of Z=1,3, and 12 respectively. The targets used in the experiments consisted of 1 mg/cm^2 natural carbon, 1 mg/cm^2 natural aluminum, 1.6 mg/cm^2 natural scandium, and 1 mg/cm^2 natural niobium. Beam intensities were approximately 100 particle pA. The beam energies used were 55 to 155 MeV/nucleon for ^{12}C, 55 to 140 MeV/nucleon for ^{20}Ne, 35 to 115 MeV/nucleon for ^{40}Ar, and 35 to 75 MeV/nucleon for ^{86}Kr. Data were taken with a minimum bias trigger (charged particle multiplicity $m \geq 2$) and a more central trigger ($m \geq 5$).

To extract collective flow in nucleus-nucleus collisions one must determine the impact parameter, b, and the reaction plane. We determined the centrality of each event by way of cuts on the total transverse momentum. Central collisions corresponding to an average impact parameter $\approx$ 0.40 b_{max} were used for each system. Here, b_{max} is the maximum estimated impact parameter. The reaction plane was determined using the method of azimuthal correlations[12].

Having selected central collisions and determined the reaction plane for each event, the average fraction of the total transverse momentum in the reaction plane, $< p_x/p_t >$, was evaluated and plotted as a function of the center of mass rapidity, y_{cm}. Fig. 1 shows an example of such a plot for He fragments from collisions of 35 MeV/nucleon Kr+Nb. The characteristic shape commonly associated with flow is quite evident in this figure. The errors shown are statistical, and the solid line corresponds to a linear least square fits for the region $-0.08 \leq y_{cm} \leq 0.08$. The slope of this line is the reduced flow.

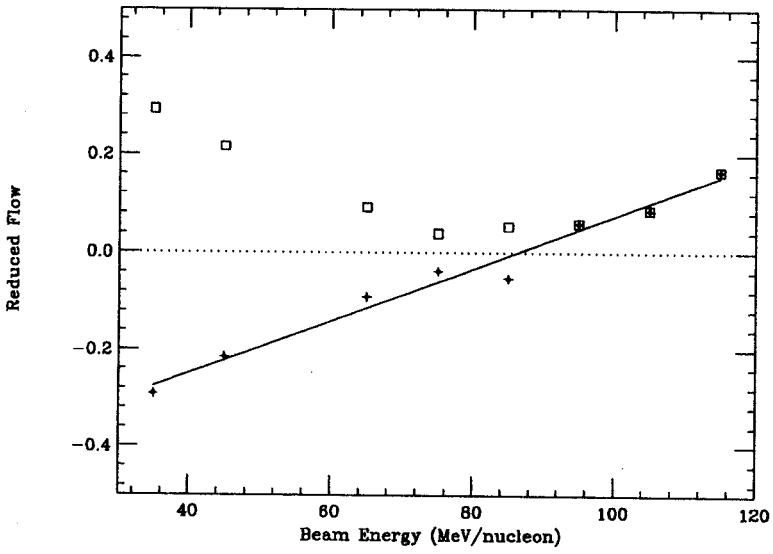

Figure 2: Reduced flow versus incident energy for protons from Ar+Sc. Squares represent reduced flow values as extracted while crosses stand for inverted reduced flow values for incident energies below 95 MeV/nucleon. Solid line is a linear fit.

The reduced flow is shown as a function of beam energy for protons from collisions of Ar+Sc in Fig. 2.

The top panel of Fig. 2a clearly shows that the reduced flow goes through a minimum. Because our measurements are unable to distinguish the sign (+ or -) of collective flow, such a minimum is indicative of the disappearance of flow. In order to facilitate the determination of E_{bal}, the extracted values of the reduced flow for beam energies below 95 MeV/nucleon are plotted as negative values in Fig. 2b. This procedure is in accordance with expectations from BUU calculations. E_{bal} is determined from this plot (Fig. 2b) by performing a linear least square fit to the reduced flow values. The solid line shown in Fig. 2b represents such a fit. The value of E_{bal} is fixed by the point or intersection of this line with the dashed line (zero reduced flow). In a similar manner, E_{bal} was extracted for C+C, Ne+Al, Ar+Sc, and Kr+Nb. Varying the point at which the values for the reduced flow changes sign makes little difference in the resulting value for E_{bal}. Nevertheless, this effect is included in the estimated errors for E_{bal}.

The fact that E_{bal} is independent of particle type is demonstrated in Fig. 3 for the Ar+Sc system. Here, we plot the reduced flow for p, d, t, and He particles as a function of incident energy. The dotted, dot-dashed, dashed, and solid lines represent linear fits to the reduced flow values of p, d, t, and He particles respectively. All of these lines intersect at approximately the same point (note arrow) indicating similar E_{bal} for each particle.

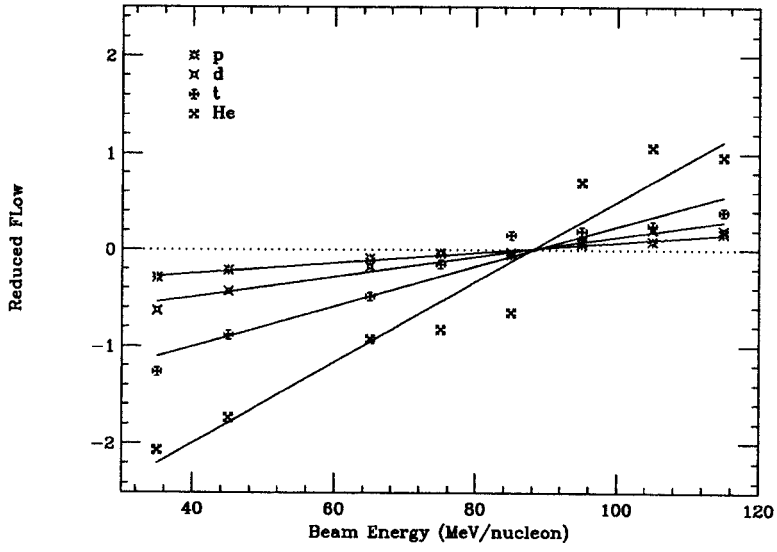

Figure 3: Reduced flow versus incident energy for p,d,t and He fragments from collisions of Ar+Sc. The lines are linear fits. Negative flow values are assigned as described in the text.

The E_{bal} values extracted for the four systems are summarized in Table 1. The value listed for each system in column two represents an average of the E_{bal} values obtained for each particle (p, d, t, and He). E_{bal} values obtained only from He particles are listed in column three. The quoted error bars which include both statistical and systematic errors are much smaller for the He particles. This difference is due to the relatively large reduced flow observed for these particles. We have also plotted E_{bal} (solid squares) as a function of the mass of the entrance-channel in Fig. 4. The solid line in this figure corresponds to a fit of the form $A^{-1/3}$, where A is the mass of the combined system. The results of BUU model calculations[13] (solid circles) are also included in Fig. 4. A fit of the form $A^{-1/3}$ to the calculated E_{bal} values is represented by the dotted line in Fig. 4. For these calculations, the in-medium nucleon-nucleon cross sections (σ_{nn}) were taken to be the free nucleon-nucleon cross sections and the incompressibility constant K was fixed at a value of 200 MeV. The calculated dependence of E_{bal} on entrance-channel mass (dotted line in Fig. 4) is strikingly similar to that of the experimental data

Table 1: Extracted values for the balance energy.

System	Balance Energy (all particles) (MeV/nucleon)	Balance Energy (helium) (MeV/nucleon)
C+C	122±6	125±2.6
Ne+Al	111±10	111±2.3
Ar+Sc	87±12	88±2.0
Kr+Nb	64±12	61±3.3

(solid line). On the other hand, the calculated E_{bal} values are systematically 10 to 20 MeV/nucleon below the experimental values. Better agreement with the data can be obtained by way of a 10% reduction of σ_{nn}. It should be stressed that while the present calculations do not allow an unambiguous distinction between a hard (K= 380 MeV) and a soft (K= 200 MeV) EOS, the calculated trends are in good agreement with those of the data. Further calculations may very well provide more stringent constraints to the EOS.

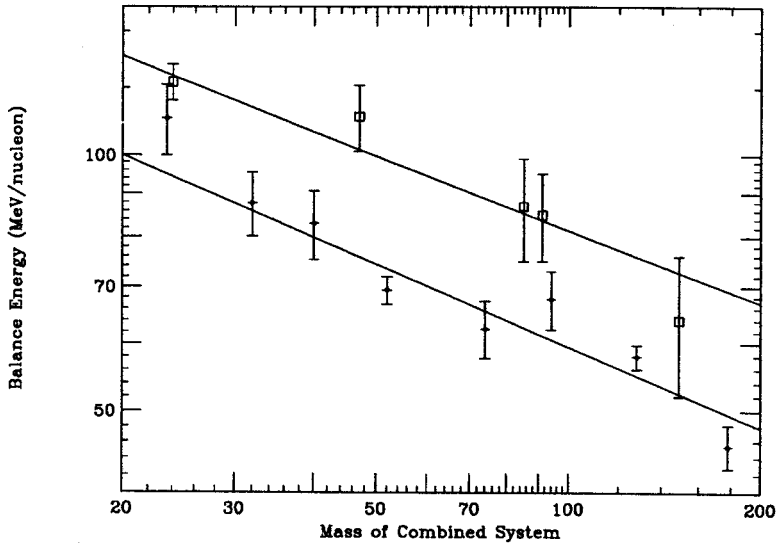

Figure 4: Extracted values of the balance energy (squares) for C+C, Ne+Al, Ar+Sc, and Kr+Nb compared with the predictions of the BUU model for a soft equation of state (crosses). The lines correspond to fits of the form $A^{-1/3}$. The value for Ar+V is from Ref. 7.

The dependence of E_{bal} on the mass of the combined system can be interpreted as a signature of the competition between the attractive mean field and the repulsive nucleon-nucleon interactions. The mean field can be associated with the surface of the two interacting nuclei and hence should scale as $A^{2/3}$. Similarly, the repulsive nucleon-nucleon interaction should scale as A. This being the case, one expects E_{bal} to show the mass dependence illustrated in Fig. 4. The fact that BUU calculations reproduce this dependence, serves to confirm the interpretation of the disappearance of flow as a balancing of the attractive scattering (dominant at low energies) by the repulsive nucleon-nucleon scattering (dominant at high energies).

In conclusion we have measured E_{bal} for C+C, Ne+Al, Ar+Sc, and Kr+Nb. These values for E_{bal} scale as $A^{-1/3}$. The observed balance energies do not depend on the particle type. BUU calculations reproduce the scaling with mass but under predict E_{bal}. These results confirm that the disappearance of flow is related to the balance between the attractive and repulsive components of the nuclear equation of state.

a. State University of New York, Stony Brook
b. University of Michigan, Dearborn
c. University of Iowa

References

1. H.H. Gutbrod, A.M. Poskanzer, and H.G. Ritter, Rep. Prog. Phys. **52**, 1267 (1989).
2. P. Danielewicz, H. Ströbele, G. Odyniec, D. Bangert, R. Bock, R. Brockmann, J.W. Harris, H.G. Pugh, W. Rauch, R.E. Renfordt, A. Sandoval, D. Schall, L.S. Schroeder and R. Stock, Phys. Rev. **C38**, 120 (1988).
3. C.A. Ogilvie, W. Bauer, D.A. Cebra, J. Clayton, S. Howden, J. Karn, A. Nadasen, A. Vander Molen, G.D. Westfall, W.K. Wilson, and J.S. Winfield, Phys. Rev. **C42**, R10 (1990).
4. D. Krofcheck, W. Bauer, G.M. Crawley, C. Djalali, S. Howden, C.A. Ogilvie, A. Vander Molen, G.D. Westfall, and W.K. Wilson, R.S. Tickle, and C. Gale, Phys. Rev. Lett. **63**, 2028 (1989).
5. J.P. Sullivan, J. Péter, D. Cussol, G. Bizard, R. Brou, M. Louvel, J.P. Patry, R. Regimbart, J.C. Steckmeyer, B. Tamain, E. Crema, H. Doubre, K. Hagel, G.M. Jin, A. Péghaire, F. Saint-Laurent, Y. Cassagnou, R. Lebrun, E. Rosato, R. Macgrath, S.C. Jeong, S.M. Lee, Y. Nagashima, T. Nakagawa, M. Ogihara, J. Kasagi, and T. Motobayashi, Phys. Lett. **B249**, 8 (1990).
6. W.M. Zhang, R. Madey, M. Elaasar, J. Schambach, D. Keane, B.D. Anderson, A.R. Baldwin, J. Cogar, J.W. Watson, G.D. Westfall, G. Krebs, and H. Wieman, Phys. Rev. **C42**, R491 (1990).
7. D. Krofcheck, D.A. Cebra, M. Cronqvist, R. Lacey, T. Li, C.A. Ogilvie, A. Vander Molen, K. Tyson, G.D. Westfall, W.K. Wilson, J.S. Winfield, A. Nadasen, and E. Norbeck, Phys. Rev. **C43**, 350 (1991).
8. D. Krofcheck, W. Bauer, G.M. Crawley, S. Howden, C.A. Ogilvie, A. Vander Molen, G.D. Westfall, W.K. Wilson, R.S. Tickle, C. Djalali, and C. Gale, Phys. Rev. C in press, 1992.
9. J. Molitoris, D. Hahn and H. Stöcker, Nucl. Phys. **A447**, 13c (1986).
10. G.F. Bertsch, W.G. Lynch and M.B. Tsang, Phys. Lett. **189B**, 384 (1987).
11. G.D. Westfall, J.E. Yurkon, J. van der Plicht, Z.M. Koenig, B.V. Jacak, R.Fox, G.M. Crawley, M.R. Maier, B.E. Hasselquist, R.S. Tickle, and D. Horn, Nucl. Inst. Meth. **A238**, 347 (1985).
12. W.K. Wilson, R. Lacey, C.A. Ogilvie, and G.D. Westfall, Phys. Rev. **C45**, 768 (1992).
13. W. Bauer, Phys. Rev. Lett. **61**, 2534 (1988) and W. Bauer, C.K. Gelbke, and S. Pratt, Ann. Rev. Nucl. Part. Sci. **42**, 77 (1992).

FISSION FRAGMENT CORRELATIONS IN HEAVY ION REACTIONS

J. Yee, G.D. Westfall, W. Bauer, D. Craig, M. Cronqvist, E. Gualtieri, S. Hannuschke, D. Klakow, T. Li, T. Reposeur, A.M. Vander Molen, W.K. Wilson, J.S. Winfield, S.J. Yennello, R. Lacey[a], A. Elmaani[a], J. Lauret[a], A. Nadasen[b], and E.Norbeck[c]

The angular correlation of fission fragments can be related to linear momentum or energy transfer, so that it may be used as a probe to the reaction mechanism.[1] The MSU 4π Array is suitable for this kind of study because it has the ability to detect from light charged particles to fission fragments at the same time as well as a geometric coverage of about 83 characterization is possible once we get all the information from the Array.

In this report, we present the folding angle distribution of the Ar + Th system with nine beam energies ranging from 15 to 115 MeV/n. A 1 mg/cm^2 Th target was used. Particle identification is done for Z = 1 - 15 using phoswich and bragg curve detectors. Although the Z and E for the particles detected in MWPC[2] are not available at this stage, the Z distribution of identified particles in correlation with MWPC events and the angular distribution of MWPC events show that the particles detected in MWPC are mainly fission fragments with our event selection. Only when two events are recorded in MWPC, do we accept those as binary fission events.

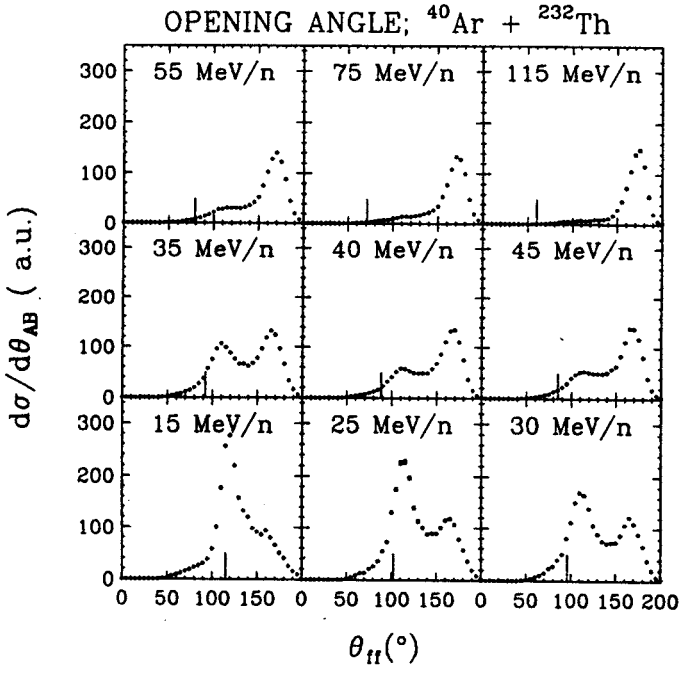

Figure 1: Folding angle distribution.

Figure 1 shows the folding angle distribution. Two distinct peaks are observed. The left peak is related to large momentum transfer and the other to low momentum transfer. The vertical bar is pointing to complete linear momentum transfer. The low momentum transfer peak is from peripheral collisions such as inelastic collisions, and the large momentum transfer peak is believed to be from incomplete fusion mixed with complete fusion which are mainly central collisions. As the beam energy increases, the centroid of the large momentum peak moves to larger folding angle, and the vertical bar moves to the smaller folding angle. The cross section from that peak also decreases. The low momentum transfer peak remains virtually at the same folding angle while the cross section grows. Qualitatively we can say that fusion-fission becomes less and less dominant while the contribution from peripheral collisions increases. These are shown in Figure 2. Here we assumed that the reaction cross section is almost the same as the fission cross section because of the high fissility(Z^2/A). The upper limit of the cross section from complete fusion can be estimated, and this is shown. It decreases rather rapidly as beam energy increases and becomes less than 10 Figure 3 shows the mean linear momentum transfer per projectile nucleon. It reaches maximum value around 30 MeV/n.

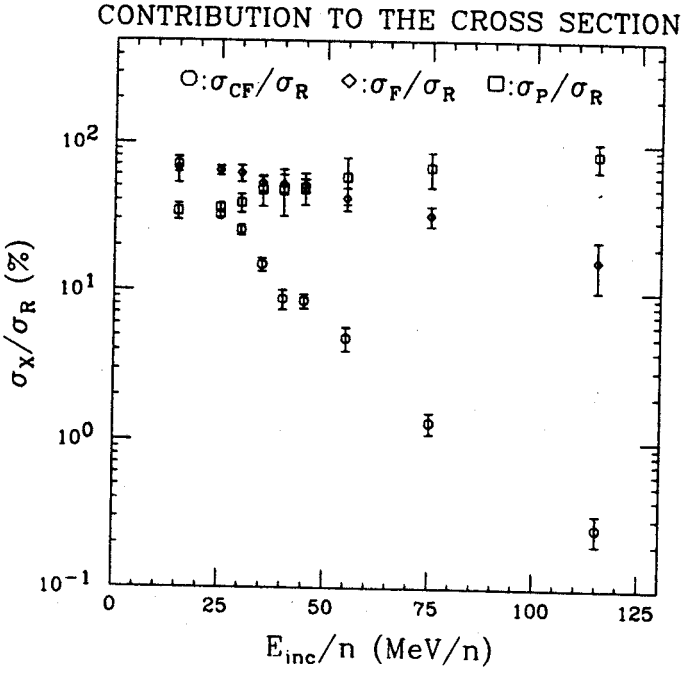

Figure 2: Ratio of cross section of each component to total reaction cross section. CF : complete fusion , F : complete + incomplete fusion , P : peripheral collision.

We observed the angular correlation of fission fragments in the Ar + Th system. The cross section from the fusion reaction decreases substantially at beam energy around 40 MeV/n, which coincides with the energy where linear momentum transfer reaches its maximum value.

a. State University of New York, Stony Brook
b. University of Michigan, Dearborn
c. University of Iowa

References

1 V.E. Voila, Nucl. Phys. A502 (1989) 531c
2 G.D. Westfall, J.E. Yurkon, J. Van Der Plicht, Z.M. Koenig, B.V. Jacak, R. Fox, G.M. Crawley, M.R. Maier and B.E. Hasselquist, Nucl. Inst. and Meth. A238 (1985) 347.

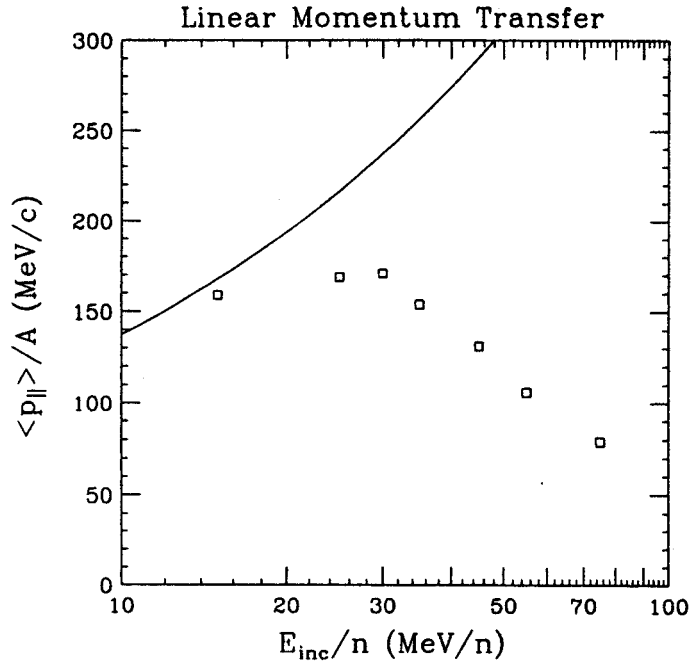

Figure 3: Linear momentum transfer per projectile nucleon. The solid line designates full momentum transfer.

HINTS TOWARD THE LIQUID GAS PHASE TRANSITION IN NUCLEAR MATTER

T. Li, W. Bauer, E. Gualtieri, S. Hannuschke,R. Lacey[a], W.J. Llope, A. Nadasen[b],E. Norbeck[c], T. Reposeur, A. Vander Molen, G.D. Westfall, J.S. Winfield, J. Yee and S. Yennello

A liquid-gas phase transition has been predicted by comparing the nuclear equation of state (EOS) with the Van der Waals equation of state[1,2]. The signature of the phase transition is a power-law cluster distribution $\sigma(A) = \alpha A^{-\tau}$ (where A is the size of a cluster, α and τ are constants) around the critical point predicted by both the droplet model [3,4] and the percolation model[5]. At the critical point, the parameter τ reaches a minimum. We have performed a bond percolation calculation [5] for the previously reported Z-distributions of central collisions of $^{40}Ar + ^{45}Sc$ at beam energies from 35 to 115 MeV/nucleon[6] and recently collected data at 15 and 25 MeV/nucleon. Assuming a cubic lattice structure and that the energy deposited into each bond after the initial compression of the reaction is described by Boltzmann distribution, the percolation calculation shows a critical temperature 8.5 ± 0.5 MeV for Ar + Sc and about 13.1 ± 0.6 MeV for infinite nuclear matter with binding energy of 8 MeV/nucleon.

We chose a nearly symmetric system, ^{40}Ar + ^{45}Sc to suppress projectile and target spectators for central collisions. The experiment was done with the Michigan State University 4π Array [7] with Bragg curve spectrometers. Beam energies of 15,25, 35, 45, 65, 75, 85, 95, 105, 115 MeV/nucleon were used to cover the phase transition region predicted by theories. The correction of detector acceptance and centrality selection have been discussed in previous publication[6].

To estimate the finite size effect, a bond breaking percolation is performed. The bond breaking percolation model assumes that each nucleon is "linked" with nearest neighbours by a potential bond. Each bond can absorb a maximum energy called the bond breaking energy, E_b, and has a probability of P_b to break. Such simulations have allowed the fitting of P_b to an experimental data [5]. In the present work, we assume that during the initial compression of nuclear reaction, the energy distributed into each bond, ϵ_b, can be described by a Boltzmann distribution with a temperature, t_b, called bond temperature. Each site of the lattice has an average of α bonds, the average energy deposited per site, $< E_s >= \alpha < \epsilon_b >$, the site temperature, $T_s = \alpha t_b$, and the binding energy per nucleon of the initial nuclear system, $B = \alpha E_b$. When the system expands, the bond which has an energy greater than the bond breaking energy, E_b, will break. Therefore the bond breaking probability is,

$$\begin{aligned} P_b &= \left(\int_{E_b}^{\infty} \sqrt{\epsilon_b} e^{-\epsilon_b/t_b} d\epsilon_b\right) / \left(\int_0^{\infty} \sqrt{\epsilon_b} e^{-\epsilon_b/t_b} d\epsilon_b\right) \\ &= \left(\int_B^{\infty} \sqrt{E_s} e^{-E_s/T_s} dE_s\right) / \left(\int_0^{\infty} \sqrt{E_s} e^{-E_s/T_s} dE_s\right). \end{aligned} \quad (1)$$

We note that the bond breaking probability P_b calculated by equation (1) is independent of α, therefore the calculation is independent of the lattice structure. We use proton kinetic energy spectra as the approximation of the initial "site" temperature of the system. By fitting the proton kinetic energy spectra with a single moving Boltzmann source [8], we obtain the temperatures for each beam energy.

The initial lattices is assumed by the fireball geometry for an overlap region of projectile and target with impact parameter of $0.25 b_{max}$ where b_{max} is the maximum impact parameter of the reaction. Therefore we used

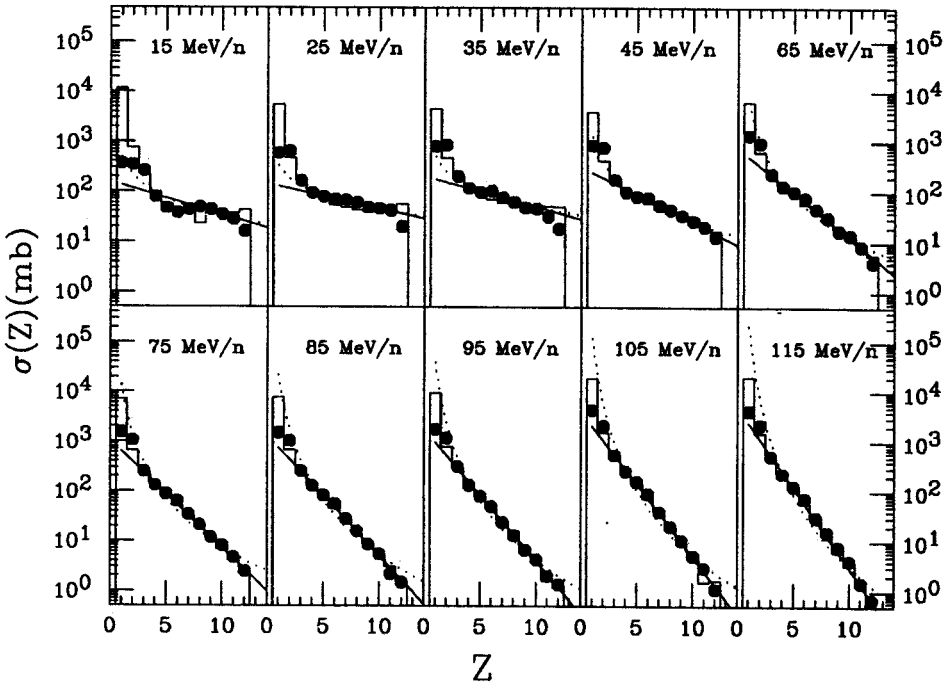

Figure 1: Z-distributions of both experimental data and percolation calculations of 15, 25, 35, 45, 65, 75, 85, 95, 105, 115 MeV/nucleon Ar + Sc. The solid circles are experimental data corrected for detector acceptance and the histograms are percolation calculations. The percolation calculations are normalized with experimental data for IMF ($3 \leq Z \leq 12$) cross sections. The dashed lines are power law fit to the percolation calculations.

initial cubic lattice of 68 sites with the bond breaking probabilities calculated by equation (1) using the kinetic temperature of protons and binding energy of 7.8 MeV/nucleon. The same percolation also performed for 150 sites to reproduce the Au + C, Al, Cu data. The binding energy used as a fitting parameter. For Au + C, Al, Cu 7.0 MeV/nucleon binding energy is used.

Fig. 1 shows the experimental Z-distributions of Ar + Sc from 15 to 115 MeV/nucleon beam energy corrected for detector acceptance (solid circle) and percolation calculation (histogram). The dashed curve is the fit of the percolation calculation to a power law distribution, $\sigma(Z) \sim Z^{-\tau}$.

The percolation results are normalized with the experimental data by the intermediate mass fragment (IMFs: $3 \leq Z \leq 12$) cross sections. The power law parameter, τ, vs. beam energy shown in Fig. 2. The solid circles are the power law fittings to the experimental data of ^{40}Ar +^{45}Sc. and the solid histogram is the percolation simulation with 68 sites and binding energy of 7.8 MeV/nucleon. The open squares are GSI data of Au + C, Al, Cu at 600 MeV/nucleon and the dashed histogram is the percolation calculation with 150 sites and 7.0 MeV/nucleon binding energy. The equivalent beam energy on the plot for GSI data is obtained by converting the excitation energy calculated by ref. [9] to a symmetric system assuming total inelastic collision. For Ar + Sc a minimum appears at about 25 MeV/nucleon corresponding to a temperature of about 8.5 ± 0.5 MeV.

In conclusion, the Z-distributions of central collisions of Ar + Sc at 15, 25, 35, 45, 65, 75, 85, 95, 105,115 MeV/nucleon has been observed and power law fits show a minimum of τ parameter at about 25 MeV/nucleon beam energy which correspond to a temperature of 8.5 ± 0.5 MeV. The percolation calculation assuming an initial energy deposition into each bond is a Boltzmann distribution, using binding energy as fitting parameter and proton kinetic temperature, reproduced both experimental data and showed lattice size dependence of the critical behavior.

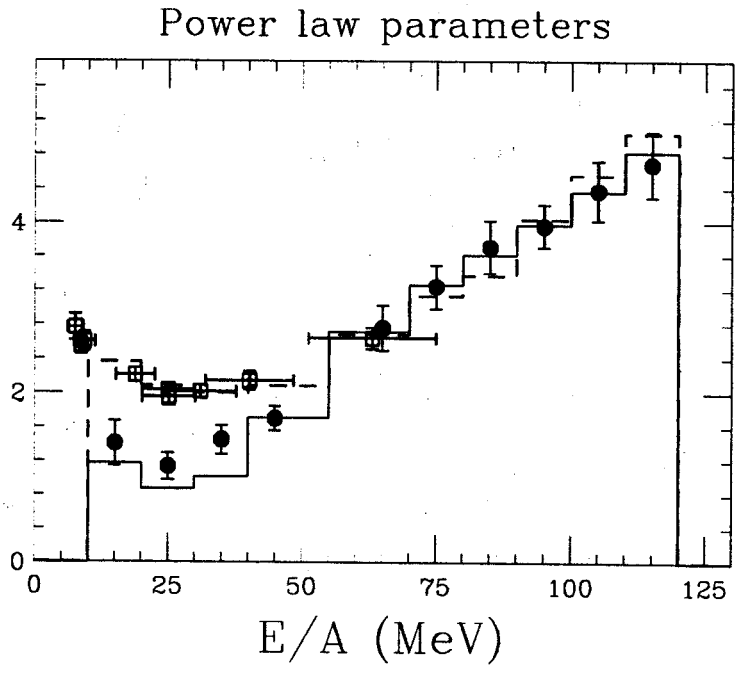

Figure 2: Comparison of power law fitting parameters to the percolation calculations with experimental results. The solid circles are the power law ($\sigma(Z) \sim Z^{-\tau}$) fit to the experimental data of Ar + Sc from 15 to 115 MeV/nucleon and the open squares are GSI data of Au + C. Al. Cu at 600 MeV/nucleon. The solid histogram is the power law fit to the percolation calculations with lattice size of 68 calculated from fireball geometry with a binding energy of 7.8 MeV/nucleon and the dashed histogram is the percolation of lattice size of 150 with binding energy of 7.0 MeV/nucleon.

a. Department of Chemistry State University of New York at Stony Brook, Stony Brook, NY11794-3400.
b. Department of Physics University of Michigan at Dearborn, Dearborn, MI 48128
c. Department of Physics and Astronomy, University of Iowa, Iowa City, Iowa 52242

References

1. David H. Boal, Alan L. Goodman, Phys. Rev. **C33**, 1690 (1986).
2. Joseph Kapusta, Phys. Rev. **C29** 1735 (1984)
3. M.E. Fisher, Physics 3, 255 (1967).
4. A.D. Panagiotou, M.W. Curtin, H. Toki, D.K. Scott, and P.J. Siemens, Phys. Rev. Lett. **52**, 496 (1984)
5. W. Bauer, Phys. Rev. **C38**, 1297 (1988).
6. T. Li, W. Bauer, D. Craig, M. Cronqvist, E. Gualtieri, S. Hannuschke, R. Lacey, W.J. Llope, T. Reposeur, A.M. Vander Molen, G.D. Westfall, W.K. Wilson, J.S. Winfield, J. Yee, S.J. Yennello, A. Nadasen, R.S. Tickle and E. Norbeck, Phys. Rev. Letts. **70** 1924 (1993)
7. G.D. Westfall, J.E. Yurkon, J. Van der Plicht, Z.M. Koenig, B.V. Jacak, R. Fox, G.M. Crawley, M.R. Maier, and B.E. Hasselquist, Nucl. Instr. and Meth. **A238**, 347 (1985)
8. G.W. Westfall, J.Gosset, P.J. Johansen, A.M. Poskanzer, and W.G. Meyer, Phys. Rev. Lett. **37**, 1202 (1976)
9. C.A. Ogilvie et al., Phys. Rev. Lett. **67**, 1214 (1991).

EVENT SHAPES FROM INTERMEDIATE ENERGY HEAVY ION REACTIONS - CENTRALITY DEPENDENCE

W.J. Llope, G.D. Westfall, D. Craig, E. Gualtieri, S. Hannuschke, T. Li, R. Pak, A. Vander Molen, J. Yee, A. Nadasen[a], R.A. Lacey[b], and E. Norbeck[c].

The emission patterns of the particles emitted during nucleus-nucleus collisions, or the "shapes" of events, are sensitive indicators of the mechanisms that govern the decay of excited nuclear systems [1,2]. Of particular interest at present is information concerning the observed transition from sequential light particle emission or binary fission decays to "multifragmentation" processes, as the excitation energy of a nuclear system is increased. Such information has been previously obtained in event shape analyses via the comparison of the shapes of experimental and model code generated events. However, these event generators are generally the most appropriate for the description of the most central collisions, where the usual model assumption of thermal or statistical equilibrium is the least tenuous. Thus, the dependence of the average event shapes in the method by which central collisions are selected from the experimental data must be understood before realistic comparisons with model code calculations.

The event shapes can be characterized by the so-called sphericity and coplanarity variables [3], which have distinct values for all possible two and three dimensional shapes of the average envelope of the particle emission. Calculated in the projectile-target center of momentum (CM) frame, the sphericity is maximal for emission patterns that are isotropic in the CM, and is severely suppressed in events for which the particle emission occurs from two or three independent (thermal) sources. Two source (projectile and target-like) descriptions can be applied for the most peripheral collisions, while increasingly more central collisions result in larger cross sections for particle emission from a source at rest in the CM frame. The sphericity therefore provides a sensitive observable by which one can evaluate the efficiencies of the various methods commonly used for the selection of central collisions from the experimental data. It is noted, however, that all event shape observables, including the sphericity and coplanarity, are susceptible to so-called "finite multiplicity distortions" [4], which are, in effect, a statement of the inability of all shape observables to describe the true shapes of events in which the measured particle multiplicities are small.

In this report, the average shapes of the events that are accepted using different experimental methods for the selection of the most central collisions will be presented. This is important prerequisite information for the comparison of the shapes of experimentally selected "central" collision events with those from the model codes. This will also allow, after the treatment of the finite multiplicity distortions to the observed shapes, inferences concerning the relative efficiencies by which the different methods for the selection of central collisions in fact minimize the impact parameters contributing to the selected events. A comprehensive set of data was collected using the MSU 4π Array [5] and analyzed, which includes the systems ^{20}Ne+^{27}Al, ^{40}Ar+^{45}Sc, ^{84}Kr+^{93}Nb, ^{129}Xe+^{129}La, each at many (intermediate) beam energies. This will allow the description of the systematic dependence of the present results on the beam energy and the total mass in (nearly) symmetric entrance channels.

Figure 1 depicts the average sphericity as a function of the "severity" of cuts used to select the most central collisions, where the cuts are placed on global observables ("centrality" variables) for which maximal values are expected to occur in the most central collisions [6]. The centrality variables studied here are the charged particle multiplicity N_{chgd} (solid), the total charge at mid-rapidity Z_{MR} (short dashed), the total multiplicity of protons, N_p, (long dashed; this variable is complementary to the total charge bound in fragments, Z_{bound}), the total charge detected Z_{det} (dot dashed), and the total transverse kinetic energy KE_T (dotted). The

horizontal axis is the fraction of the total number of events that are accepted above a threshold placed on the global observables listed above. The inclusive average sphericities are therefore left most in each frame, while proceeding to the right implies increasingly strict cuts on the largest values of the centrality variable. Four representative systems are shown, as labelled in each frame.

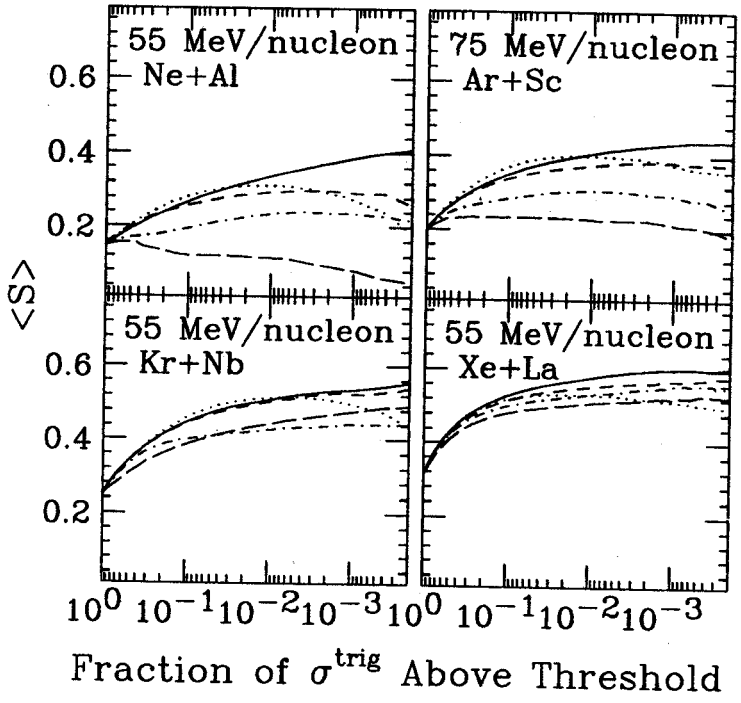

Figure 1: The mean sphericity of events selected by one-dimensional cuts on the various centrality variables. The horizontal axis is the fraction of the total number of events accepted by a lower limit cut on each variable separately.

There are apparently large differences in the average shapes of events selected by cuts placed on the different centrality variables, which would affect the accuracy of inferences made during the comparison of the average shapes of the experimentally selected "central" collisions and those from model code calculations. These curves cannot, however, be used to evaluate the relative efficiencies of the various centrality variables for the selection of central collisions, for reasons that are now described.

All event shape observables accurately describe the average envelope of the particle emission only in the limit of infinite particle multiplicities. The finite multiplicity distortions to the sphericity and coplanarity have been quantified for the present analysis using events generated with specified shapes and multiplicities and filtered through an extensively tested software replica of the 4π Array. Depending on the generated shape of the event, the finite multiplicity distortions to the sphericity and coplanarity may be severe, especially for the lowest multiplicities. The differences between the curves of Figure 1 may thus be artifacts of different finite multiplicity distortions to the shapes of the events selected by cuts on the different variables, and not at all related to the different efficiencies of these variables for the selection of central collisions.

This possibility is motivated by Figure 2, which depicts the mean values and the widths of the charged particle multiplicity spectra accepted by cuts on the the different centrality variables, for two representative systems. The horizontal axis is the same as that for Figure 1. The spectra of charged particle multiplicities for

the events accepted by cuts on the different centrality variables can be very different, as reflected by the different mean values and widths seen in Figure 2. The relative spacings of the curves shown in Figure 1 must therefore be affected by different multiplicity distortions to each curve. These distortions must be individually treated in some way before the relative efficiencies of the different variables for the selection of the most central collisions can be inferred.

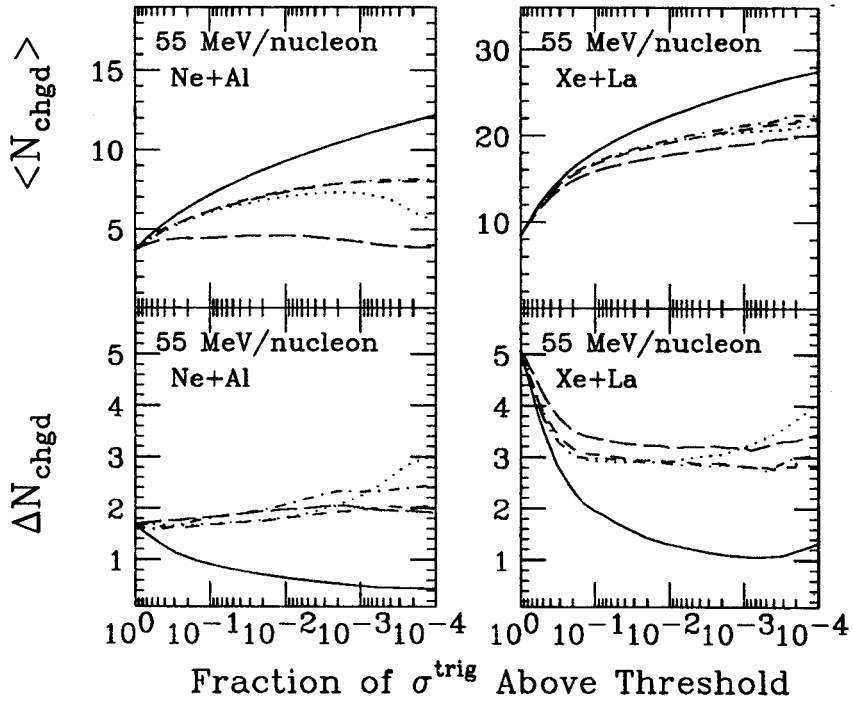

Figure 2: The mean values and widths of the multiplicity spectra of events selected by one-dimensional cuts on the various centrality variables for 55 MeV/nucleon ^{20}Ne+^{27}Al and ^{129}Xe+^{139}La. The horizontal axis is the fraction of the total number of events accepted by a lower limit cut on each variable separately.

The biases to results obtained in event shape analyses that are made possible by the finite multiplicity distortions were previously [1,2] removed by the matching of the experimental and model code generated multiplicity spectra for the study of central ^{40}Ar+^{51}V collisions [1], or by studying only exclusively defined final states for the dissociations of ^{16}O in peripheral collisions [2]. Such methods for the treatment of the finite multiplicity distortions are inapplicable for this study, as model code event generation is not involved and the exclusive definition of final states is made intractable due to their number. Several methods for the treatment of the multiplicity distortions in the present analysis were investigated, and the most accurate of these is now described.

The experimental dependence of the average sphericity on the measured charged particle multiplicity is shown in Figure 3. It is noted that the mean sphericity at specific multiplicities is only weakly dependent on the total entrance channel mass and the beam energy.

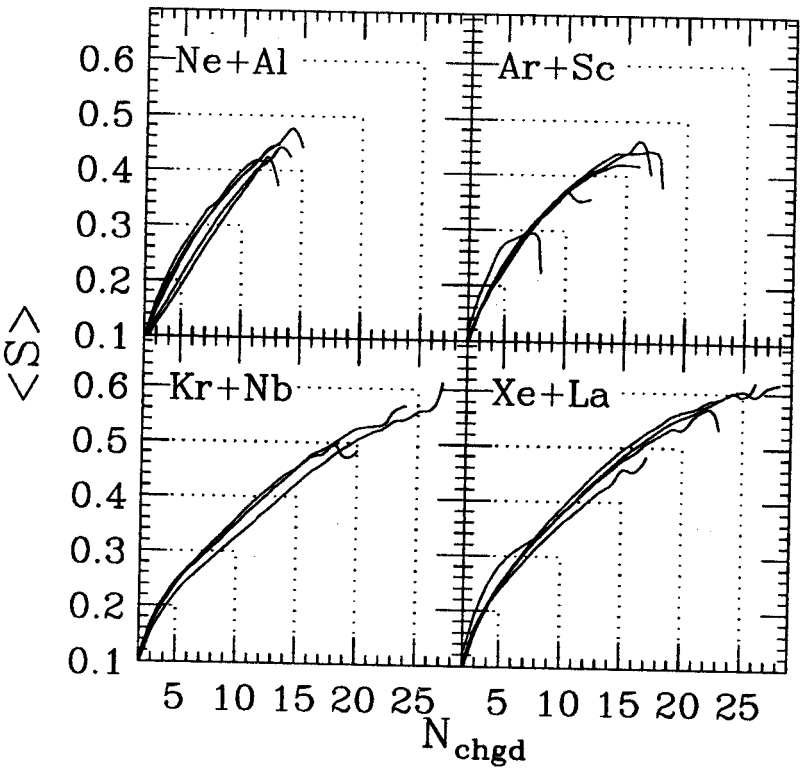

Figure 3: The mean values of the sphericity versus the multiplicity for the systems ^{20}Ne+^{27}Al (55, 75, 95, 115, and 135 MeV/nucleon), ^{40}Ar+^{45}Sc (15, 35, 75, 95, and 115 MeV/nucleon), ^{84}Kr+^{93}Nb (35, 55, and 75 MeV/nucleon), and ^{129}Xe+^{139}La (25, 35, 45, and 55 MeV/nucleon).

The present treatment of the multiplicity distortions to the curves shown in Figure 1 starts with the specification of these (semi-inclusive) average sphericities versus the multiplicity as "reference" average sphericities, $< S_{ref} >$. Then, in a second pass through the data, the reference sphericity for each event is located from the appropriate curve of Figure 3, using the measured multiplicity of the event. A "reduced" sphericity is then defined as $S_{red} = S/ < S_{ref} >$, where S is the measured sphericity of the event.

The average values of the "reduced" sphericities so defined, as functions of the severity of different centrality cuts, can then be extracted in the same way as was done for Figure 1. The average values of the reduced sphericities are free from the multiplicity distortions by definition, so that the average reduced sphericities obtained by different centrality cuts imply the relative efficiencies by which each centrality cut selects the smallest impact parameter events.

The inclusive distributions of each centrality variable were converted into "reduced" impact parameter scales using the geometrical prescription of Cavata *et al.* [7]. These generally implied that cuts strict enough to allow $\lesssim$10% of the events select average reduced impact parameters $< b > /[R_P + R_T] \sim 0.25$, where $R_P(R_T)$ is the radius of the projectile(target) nucleus. This selection of $\sim$10% of the events as the most central collisions is somewhat *ad hoc*, as it is generally expected that stricter cuts do not more efficiently select the most central collisions (see below).

The variable(s) which are the most efficient for the selection of central collisions in a given system and beam energy are thus those with the largest average reduced sphericities for cuts such that $\lesssim$10% of the events are selected. The average values of the "reduced" sphericities as functions of the severity of different centrality

cuts are shown in Figure 4 for the same systems and beam energies shown in Figure 1.

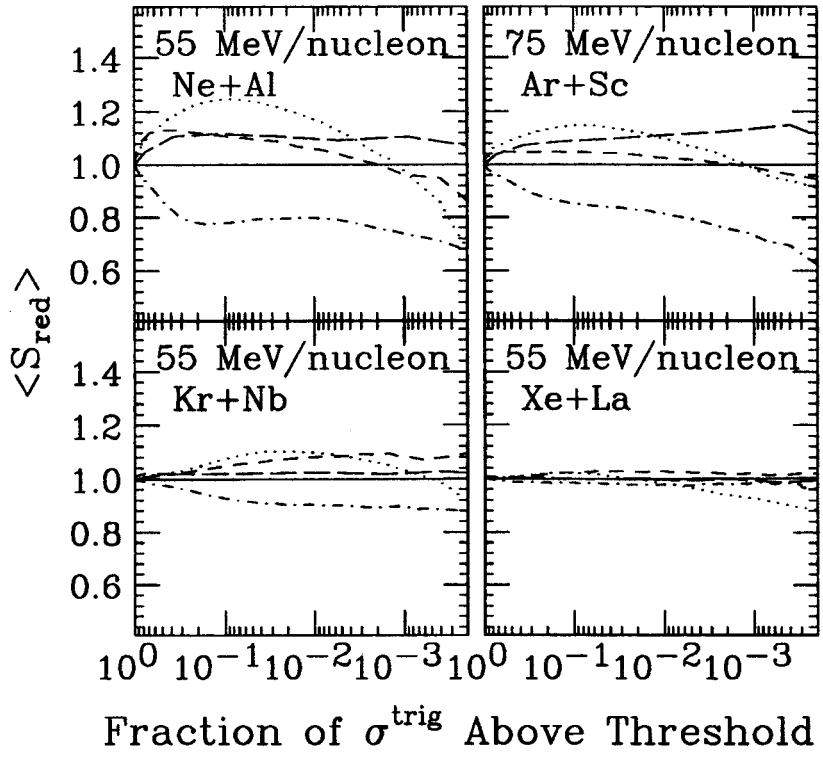

Figure 4: The same as Figure 1, except that the vertical axis is the reduced sphericity of the events passing specific cuts on the different centrality variables.

The particular choice of centrality variable is apparently the most crucial in the lighter systems, while increases in the entrance channel mass lessen the distinctions between the average shapes obtained from cuts on the different centrality variables. A drop-off of $< S_{red} >$ for increasingly strict cuts implies that such very strict cuts do not select significantly more central events, but events with significant topological fluctuations. Such topological fluctuations are apparently very important in the lightest systems, especially for the highest beam energies, but are of lesser importance in the heavier systems.

The relative efficiencies of the various centrality variables for the selection of the smallest impact parameter collisions can be read directly from Figure 4. A summary of the full beam energy dependence of this ranking of the relative efficiencies of the centrality variables for the four systems is given in the Table below. For each system and range of beam energies, the most efficient centrality variables are listed in order of decreasing efficiency. Parentheses around two or more centrality variables are used to indicate that the average reduced sphericities obtained from specific cuts on the enclosed variables are very similar.

System	$KE_{proj} \lesssim 30$ MeV/nucleon	$KE_{proj} \gtrsim 30$ MeV/nucleon
^{20}Ne+^{27}Al	N/A	KE_T, (N_p, Z_{MR}), N_{chgd}
^{40}Ar+^{45}Sc	N_p, N_{chgd}, (Z_{MR}, KE_T)	KE_T, (N_p, Z_{MR}), N_{chgd}
^{84}Kr+^{93}Nb	N/A	KE_T, Z_{MR}, (N_p, N_{chgd})
^{129}Xe+^{139}La	N_p, N_{chgd}, Z_{MR}	(Z_{MR}, KE_T), (N_p, N_{chgd})

At the lowest beam energies ($\lesssim$ 30 MeV/nucleon), the particle multiplicities, N_p and N_{chgd}, are the most efficient for the selection of the most central collisions, independent of the entrance channel mass. In all but the heaviest system (^{129}Xe+^{139}La) at beam energies larger than ~30 MeV/nucleon, the most central events are selected with the highest efficiency by cuts on the variable KE_T, while in the heaviest system, the efficiencies of the different variables are similar, with cuts on Z_{MR} being slightly more efficient than cuts on the other centrality variables. The variable Z_{det} is always the least efficient for the selection of the most central collisions, which would be expected for any data collected in a (nearly) 4π geometry.

The present analysis has evaluated the relative efficiencies by which various one-dimensional cuts select the most central collisions. Multi-dimensional centrality cuts limit the selection of less than central events that have significant topological fluctuations, which are apparently especially important for collisions between light nuclei. The most efficient two dimensional centrality gate for these data would then involve those two centrality variables which result in the largest average reduced sphericities, which can be read from the Table above. Further studies of such multi-dimensional cuts, which involve the extraction of the widths of the reduced sphericities, $\Delta S = \sqrt{[< S_{red}^2 > - < S_{red} >^2]}$, as functions of the centrality variable and cut, are presently underway.

In addition, the study of the system and beam energy dependence of the predominant reaction mechanisms, i.e. deep-inelastic collisions or sequential versus multifragment decays of a single exited residue (see W.J. Llope *et al.*, in this Annual Report), in these data would allow the correlation of the most efficient centrality conditions with the characteristics of the predominant reaction mechanisms. It is expected that the observed evolution of the most efficient centrality variables as a function of the system mass and beam energy has contributions from a similar evolution in the predominant reaction decay mechanisms. Indeed, the centrality variables N_{chgd} and N_p would be expected to depend strongly on the characteristics of the reaction decay mechanisms, while the variables Z_{MR} and KE_T are largely "coalescence invariant". Work along these lines is in progress.

a. Department of Physics, U. of Michigan - Dearborn, Dearborn, MI 48128
b. Department of Chemistry, SUNY - Stony Brook, Stony Brook, NY 11794
c. Dept. of Physics and Astronomy, U. of Iowa, Iowa City, IA 52242

References

1. D.A. Cebra, *et al.*, Phys. Rev. Lett. **64**, 2246 (1990); H.W. Barz *et al.*, Phys. Lett. **267B**, 317 (1991).
2. B.A. Harmon *et al.*, Phys. Lett. **235B**, 234 (1990); A. Badalá *et al.*, *ibid.* **299B**, 11 (1993); J. Suro *et al.*, Nucl. Phys. **A548**, 353 (1992); J.P. Bondorf *et al.*, Phys. Rev. C **46**, 374 (1992).
3. M. Gyulassy *et al.*, Phys. Lett. **110B**, 185 (1982); G. Fái *et al.*, Nucl. Phys. **A404**, 551 (1983).
4. P. Danielewicz *et al.*, Phys. Lett. **129B**, 283 (1983); J.P. Bondorf *et al.*, *ibid.* **240B**, 28 (1990).
5. G.D. Westfall *et al.*, Nucl. Inst. and Methods **A238**, 347 (1985).
6. C.A. Ogilvie *et al.*, Phys. Rev. C **40**, 654 (1989); L. Phair *et al.*, Nucl. Phys. **A548**, 489 (1992); W.J. Llope *et al.*, submitted to Physical Review C.
7. C. Cavata *et al.*, Phys. Rev. C **42**, 1760 (1990).

EVENT SHAPES FROM INTERMEDIATE ENERGY HEAVY ION REACTIONS – MULTIFRAGMENTATION

W.J. Llope, G.D. Westfall, C.M. Mader, W. Bauer, D. Craig, E. Gualtieri, S. Hannuschke, T. Li, R. Pak, A. Vander Molen, J. Yee, A. Nadasen[a], R.A. Lacey[b], and E. Norbeck[c].

A transition in decay mechanisms occurs as the excitation of nuclear systems is increased - from the predominance of decays involving the sequential emission of particles or binary fissions to those which the decay proceeds much more rapidly, and includes the emission of many intermediate mass fragments (IMFs, for which $3 \leq Z \lesssim 20$). While sequential decays are generally well understood on the basis of extended Hauser-Feshbach descriptions of the nuclear systems formed in low energy heavy ion collisions, the description of the relatively rapid, more violent, "multifragmentation" processes observed in intermediate energy collisions is less certain. Model codes written for the description of multifragmentation reactions may involve assumptions concerning fundamental physics, such as the nuclear equation of state, in-medium scattering cross sections and Pauli blocking, liquid–gas phase transitions in nuclear matter, et cetera.

These two general decay mechanisms are expected to result in different patterns of the emission of the final state particles and fragments, i.e. different "shapes" of the events. As the sum over a cascade of single particle or light fragment emissions from, or binary fissions of, an excited residue over long time scales, sequentially decaying systems generally have average emission patterns that are elongated prolate or triaxial shapes in phase space. Multifragmentation reactions apparently involve the more rapid explosion of the nuclear system, which produce larger numbers of IMFs in events with overall more spherical emission patterns.

The patterns of the particle emission are thus sensitive indicators of the characteristics of the reaction mechanisms, and these emission patterns can be characterized by the so–called sphericity and coplanarity variables [1]. These variables describe the relative lengths of the three principal axes of the average emission pattern event by event, and have distinct values for all possible two and three dimensional shapes. Comparisons of the sphericity/coplanarity distributions obtained from experimental and model code generated events have previously been performed for central $^{40}Ar+^{51}V$ collisions [2,3], and for peripheral collisions in lighter systems [4]. Sensitive tests of the beam energy dependence of the accuracy of various model code calculations for the description of the observed shapes in these systems were described, and inferences concerning the importance of sequential and multifragmentation decay processes were made.

In the present article, an event shape analysis of a comprehensive set of experimental data collected with the MSU 4π Array [5] is described. The present analysis includes a wide range of total mass in (nearly) symmetric entrance channels (from $^{20}Ne+^{27}Al$, $^{40}Ar+^{45}Sc$, $^{84}Kr+^{93}Nb$, $^{129}Xe+^{139}La$ collisions), with each system measured over a wide range of intermediate beam energies. The experimental event shapes are compared to those obtained from four different model code event generators, and the beam energy and entrance channel mass dependence of the accuracy by which the various model codes reproduce the experimental shapes will be described. Two of these event generators embody the well known aspects of sequential or (multiple) binary fission decay mechanisms, while the other two simulate multifragmentation processes, so that the beam energy and system mass dependence of the relative importance of these general decay mechanisms in the experimental data should be apparent.

Each of these four decay models assume that either thermal or statistical equilibrium has been obtained in specified nuclear system, and their output contains the charge, mass, kinetic energy, and angles for each of the particles and fragments in the final state. These events are then Lorentz boosted from the projectile–target center of momentum frame (CM) into the laboratory (see below), and then filtered through an accurate software

replica of the 4π Array. In order to make realistic comparisons of the event shapes from the model codes with those from the experimental data, attention must first be directed along two specific directions.

First, experimental events must be selected for which it is most probable that a thermalized nuclear system of known charge and mass has been formed. This is accomplished via the selection of the most central collisions; a previous event shape analysis of these data [6] has indicated the most efficient means by which such collisions can be experimentally selected. For data at beam energies $\gtrsim$30 MeV/nucleon, the placement of simultaneous thresholds on the total transverse kinetic energy, KE_T, and the total charge at mid-rapidity, Z_{MR}, each threshold such that the "top" $\sim$10% of the events are accepted by this two-dimensional cut, results in the selection of the most central collisions with the highest efficiency [6]. Centrality cuts on the proton or total charged particle multiplicity, N_p or N_{chgd}, were seen to be efficient only at the lowest beam energies, i.e. $\lesssim$30 MeV/nucleon, independent of the entrance channel mass.

Second, the model code input parameters, i.e. the initial charge Z, mass A, total excitation energy E^*, and angular momentum J of the decaying system, must be specified for each projectile–target combination and beam energy. The model codes used for the generation of events with sequential decays are "Sequential" [2], and "Gemini" [7], while multifragmentation events are generated with the "Copenhagen" [3] and "Berlin" [8] codes. For each code, the charge and mass of the decaying system is taken as that contained in the region of geometrical overlap for collisions at average impact parameters appropriate [6] for the above method for the selection of the most central collisions, which is $< b > /b_{max} \sim 0.25$. Roughly 80% of the total number of nucleons in the projectile and target nuclei are thus assumed to form a single decaying system at rest in the CM frame. The excitation energy of this system is obtained from BUU calculations (see e.g. Ref. [9]), which were run at $b/b_{max} \sim 0.25$, and terminated for each system and beam energy when the average density of the system following a compressional phase dropped below the average density in the entrance channel. Angular momentum effects are included in the Gemini and Berlin codes (sequential and multifragmentation, respectively); the maximum angular momenta allowed for these codes was $36\hbar$, $65\hbar$, $80\hbar$, and $70\hbar$, for the systems formed in the most central ^{20}Ne+^{27}Al, ^{40}Ar+^{45}Sc, ^{84}Kr+^{93}Nb, and ^{129}Xe+^{139}La collisions, respectively. The system sizes and excitation energies from the BUU calculations are not strongly dependent on whether a stiff or soft nuclear equation of state (EOS) is assumed, and except at the lowest beam energies, the average shapes at specific multiplicities from the filtered model codes when a stiff and soft EOS are used in the BUU calculations are nearly identical.

The finite multiplicity distortions [10] to shapes of the events from the data and the model codes are removed in the present analysis via the presentation of the average event shapes versus the measured(filtered) multiplicity in the experimental(generated) event. This method furthermore has the advantage that, at a specific multiplicity, the experimental and model code generated shapes can be compared even if the overall multiplicity distributions from the data and the model codes are not in agreement. Any uncertainties in the extraction of the decay model input parameters from the BUU calculations, which may be related to the uncertainty in the time at which the BUU calculations are stopped and the decay model codes started, as well as uncertainties in the in-medium nucleon-nucleon scattering cross sections, the form of the EOS, et cetera, do not compromise the accuracy of the present analysis. The average sphericities at specific multiplicities that are obtained from a given decay model are largely insensitive to changes in the decay model input parameters when e.g. the BUU calculations are run for longer times.

Only an illustrative subset of all of the systems and beam energies that were analyzed will be discussed here. The average sphericity of the experimental(generated) events versus the measured(filtered) multiplicity are shown in Figure 1, while the average coplanarities are shown in Figure 2. The crossed points are the experimental

semi-inclusive average shapes, while the diamonds are the average shapes for the most central events selected as

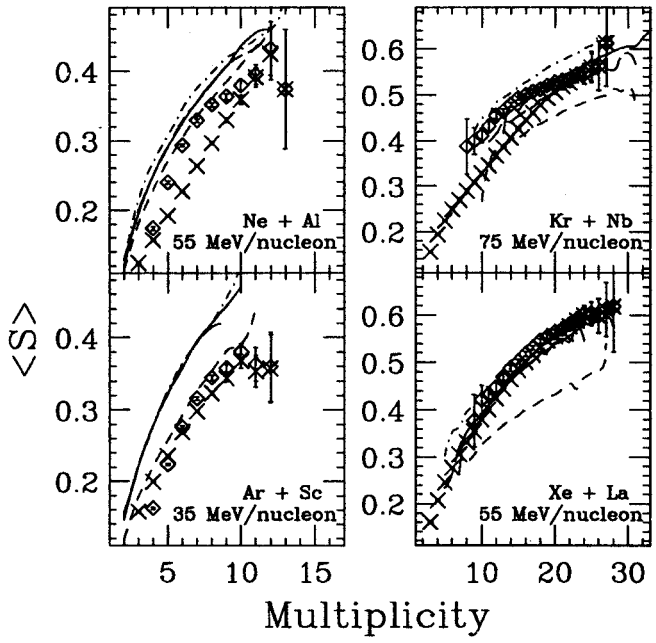

Figure 1: The average sphericity versus the multiplicity for the inclusive experimental data (crosses), the most central experimental collisions (diamonds), and the various filtered model code events (lines).

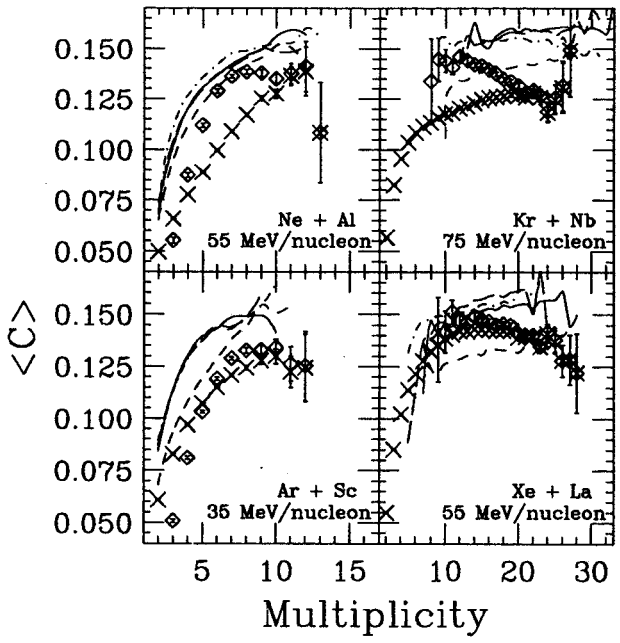

Figure 2: The average coplanarity versus the multiplicity for the inclusive experimental data (crosses), the most central experimental collisions (diamonds), and the various filtered model code events (lines).

described above and in Ref. [6]. The filtered model code shapes are given by the lines: the multifragmentation

decay codes are the solid and long-dashed (Berlin and Copenhagen, respectively) lines, while the sequential decay codes are short-dashed and dot-dashed (Sequential and Gemini, respectively) lines.

The increase in the average sphericities going from the semi-inclusive events (crosses) to those when the most central collisions are selected (diamonds) is most pronounced in the light systems. This is to be expected from the previous event shape analysis of these data [6], which implied that the use of the multiplicity alone to specify centrality in the lighter systems (at the beam energies shown in Figures 1 and 2) is significantly less efficient than cuts on the variables KE_T and/or Z_{MR}. As the system mass is increased, the efficiencies of the various centrality variables become similar, and centrality gating using the multiplicity is not significantly less efficient than the two dimensional cut described above. It is surprising, however, to note that the average coplanarities at intermediate multiplicities *also* increase when only the most central events are analyzed, especially for the lighter systems. This could be an artifact of the transverse collective flow already observed in these data [11]; further analysis of the sensitivity of the coplanarity variable to transverse collective flow is underway.

The comparison, at specific multiplicities, of the experimental average shapes from the central collisions (diamonds) and the various model codes (lines) can be used to infer the validity of each model code for the description of the shapes of the measured events. In the lighter systems (each shown at the lowest beam energies that were analyzed in each case), the filtered Sequential model [2] events most nearly reproduce the experimental sphericities of the most central experimental events. In the heavier systems (each shown at the highest beam energies collected in each case), the average sphericities are more accurately described by either of the multifragmentation models, i.e. the Berlin [8] and Copenhagen [3] codes. The sequential binary fission code Gemini [7] fails to reproduce the experimental shapes for all of the systems shown above. There is generally poorer agreement between the generated and experimental coplanarities. This may again be related to transverse collective flow effects, which are not included in any of the event generators used here.

Figures 1 and 2 indicate that the validity of a particular decay model for the description of the shapes of the most central experimental events can be evaluated with reasonable sensitivity in the present analysis. Additional tests of the various models are possible via the comparisons of the experimental and model code generated shapes of particular subsets of the particles in the event; e.g. the IMFs. The average sphericities of only the IMFs is plotted versus the multiplicity of IMFs (again removing the finite multiplicity distortions) in Figure 3, for the same systems shown in Figures 1 and 2.

In the lighter systems shown, the average IMF sphericities are not accurately described over the full range of observed IMF multiplicities by any of the four decay models. The emission of IMFs in the lighter systems is substantially less isotropic in the CM frame than predicted by the models, although the shapes of the entire events in the lighter systems are reasonably well reproduced by the Sequential model [2]. The dependence of the rapidity distributions of the IMFs on the IMF multiplicity indicates that, even in the selected central collisions, IMF emission in these light systems is predominantly from projectile-like and target-like sources. In the heavier systems, quantitative agreement over the full range of IMF multiplicities exists between the two multifragmentation models [3,8] and the experimental data, while both of the sequential decay models [2,7] significantly underestimate the observed IMF sphericities.

It is noted that there may be additional or magnified uncertainties in the interpretation of the shapes of subsets of the events. The multiplicities are generally much lower leading to more severe shape distortions and lesser sensitivity to the distinctions between the data and the model predictions. Also, the total momentum need not be conserved amongst the particles included in some subset of the event. Nonetheless, the study of the shapes of subsets of the events, e.g. IMFs or light charged particles (S, C), particles at mid-rapidity (C), et cetera, appears particularly promising. Certainly, the evidence for the validity of a particular model for

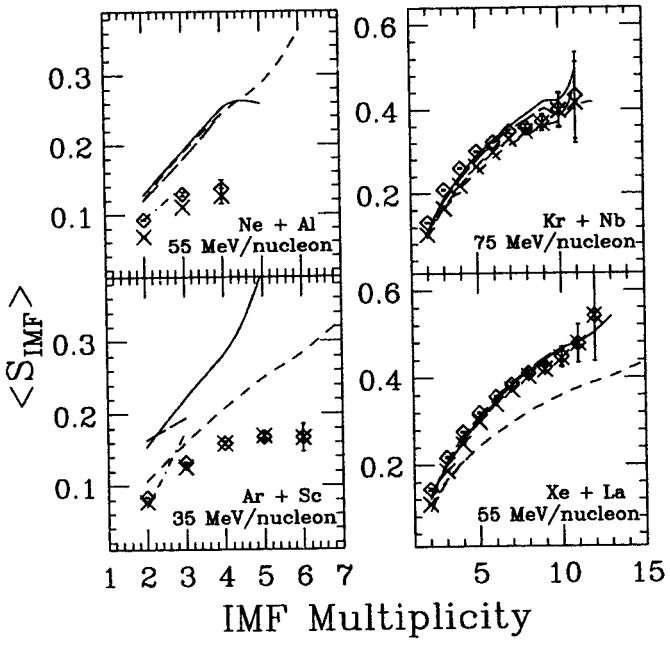

Figure 3: The average sphericity of only the IMFs in the events, versus the multiplicity of IMFs, for the inclusive experimental data (crosses), the most central experimental collisions (diamonds), and the various filtered model code events (lines).

some system and beam energy is strengthened if both the average shapes from the entire event and particular subsets of the event are reproduced. This is apparently the case for the heavier systems shown; either of the multifragmentation models quantitatively reproduce the observed shapes for the entire events as well as the shapes of the IMF emission alone.

The wide range of beam energies collected for the four systems (55 - 135 MeV/nucleon for ^{20}Ne+^{27}Al, 15 - 115 MeV/nucleon for ^{40}Ar+^{45}Sc, 35 - 75 MeV/nucleon for ^{84}Kr+^{93}Nb, and 25 - 55 MeV/nucleon for ^{129}Xe+^{139}La, each in ~10 MeV/nucleon steps), will give detailed information concerning the excitation energy dependence of the validity of the various model codes for each system. The present analysis will therefore indicate the system mass and excitation energy dependence of the relative probabilities for sequential and multifragmentation decays of the excited nuclear systems formed in (nearly) symmetric intermediate energy heavy ion collisions.

a. Department of Physics, U. of Michigan - Dearborn, Dearborn, MI 48128
b. Department of Chemistry, SUNY - Stony Brook, Stony Brook, NY 11794
c. Dept. of Physics and Astronomy, U. of Iowa, Iowa City, IA 52242

References

1. M. Gyulassy *et al.*, Phys. Lett. **110B**, 185 (1982); G. Fái *et al.*, Nucl. Phys. **A404**, 551 (1983).
2. D.A. Cebra, *et al.*, Phys. Rev. Lett. **64**, 2246 (1990);
3. H.W. Barz *et al.*, Phys. Lett. **267B**, 317 (1991).
4. B.A. Harmon *et al.*, Phys. Lett. **235B**, 234 (1990); A. Badalá *et al.*, *ibid.* **299B**, 11 (1993); J. Suro *et al.*, Nucl. Phys. **A548**, 353 (1992); J.P. Bondorf *et al.*, Phys. Rev. C **46**, 374 (1992).
5. G.D. Westfall *et al.*, Nucl. Inst. and Methods **A238**, 347 (1985).

6. W.J. Llope *et al.*, submitted to Phys. Rev. C (1993); see also W.J. Llope *et al.* in this Annual Report.
7. R.J. Charity *et al.*, Nucl. Phys. **A340**, 371 (1988).
8. Sa Ban-Hao and D.H.E. Gross, Nucl. Phys. **A437**, 643 (1985); X.-Z. Zhang *et al.*, *ibid.* **A461**, 641 (1987); X.-Z. Zhang *et al.*, *ibid.* **A461**, 668 (1987).
9. D.R. Bowman *et al.*, Phys. Rev. C **46**, 1834 (1992).
10. P. Danielewicz *et al.*, Phys. Lett. **129B**, 283 (1983).
11. G.D. Westfall *et al.*, submitted to Phys. Rev. Lett. (1993).

FRAGMENTATION OF ^{86}Kr AT 70 MeV/NUCLEON

R. Pfaff, M. Fauerbach, M. Hellström, J. Kelley, R.A. Kryger, D.J. Morrissey, B.M. Sherrill, M. Steiner, J.S. Winfield, J.A. Winger, and B.M. Young

Projectile fragmentation, especially at intermediate energies (50–100 MeV/nucleon) has proven to be an efficient method for producing beams of radioactive nuclei[1–3]. At these energies, one– or multi–nucleon transfer processes also take place, leading to reaction products with higher neutron or proton numbers — and even higher masses — than the incident projectile. Mohar *et al.*[2] have demonstrated the importance of these transfer reactions for producing nuclei very far from stability, where in many cases no other reaction mechanism would be as effective.

It is crucial for the planning of future experiments with secondary beams that the total production yields of exotic nuclei can be accurately predicted. However, at present no theoretical model exists that can accurately predict the transfer reaction production cross sections for projectile–like fragments. To achieve this, we need a better understanding of the interplay between the competing reaction mechanisms in this energy region, and to map out the gradual transition from the deep inelastic processes of the low–energy regime to the more violent collisions at relativistic energies. Until now, the efforts to achieve this have been greatly hampered by the lack of sufficient experimental data, especially from reactions with heavy (A> 80) projectiles at a range of energies. The aim of the present study — together with other experiments to be performed at the NSCL — is to close this gap in our knowledge by providing high–quality data on production yields and momentum distributions for the "fragmentation" of a heavy projectiles in the intermediate energy region.

In December of 1992 we performed an experiment at the NSCL, using the A1200 projectile fragment mass separator[4]. A 0.6 pnA 70 MeV/nucleon ^{86}Kr beam, delivered by the K1200 cyclotron, was allowed to interact with 4 mg/cm^2 aluminum target placed at the medium acceptance target position of the A1200. The settings of the separator were varied stepwise, covering a rigidity range of Bρ=2.40–2.85, corresponding to fragment mass–to–charge ratios A/Q = 1.95–2.36. The detector setup, see Figure 1, included timing scintillators, position–sensitive parallel–plate avalanche (PPAC) detectors, and a silicon telescope.

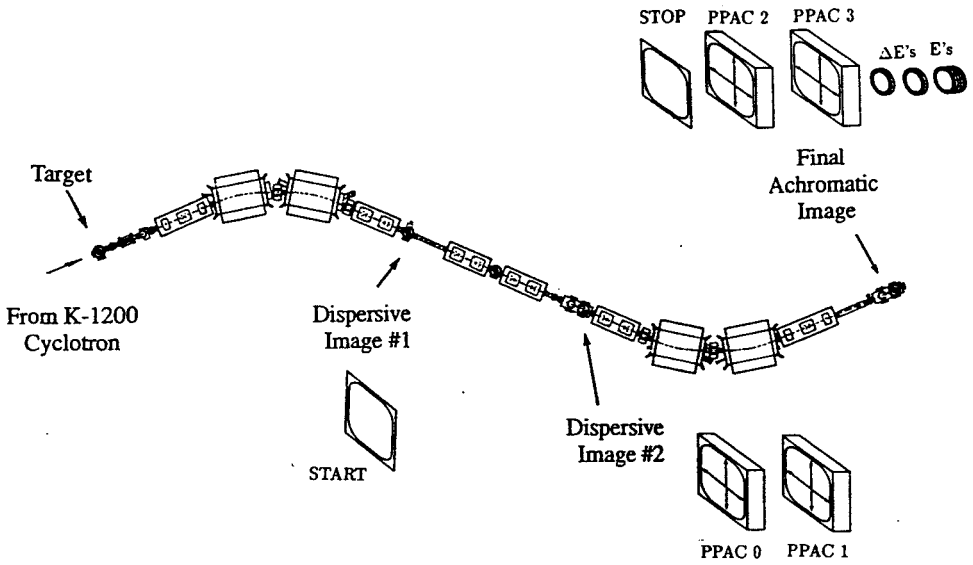

Figure 1: The A1200 projectile fragment separator at NSCL. The detector setup used in the present study was identical to that used by Yennello *et al.*[5].

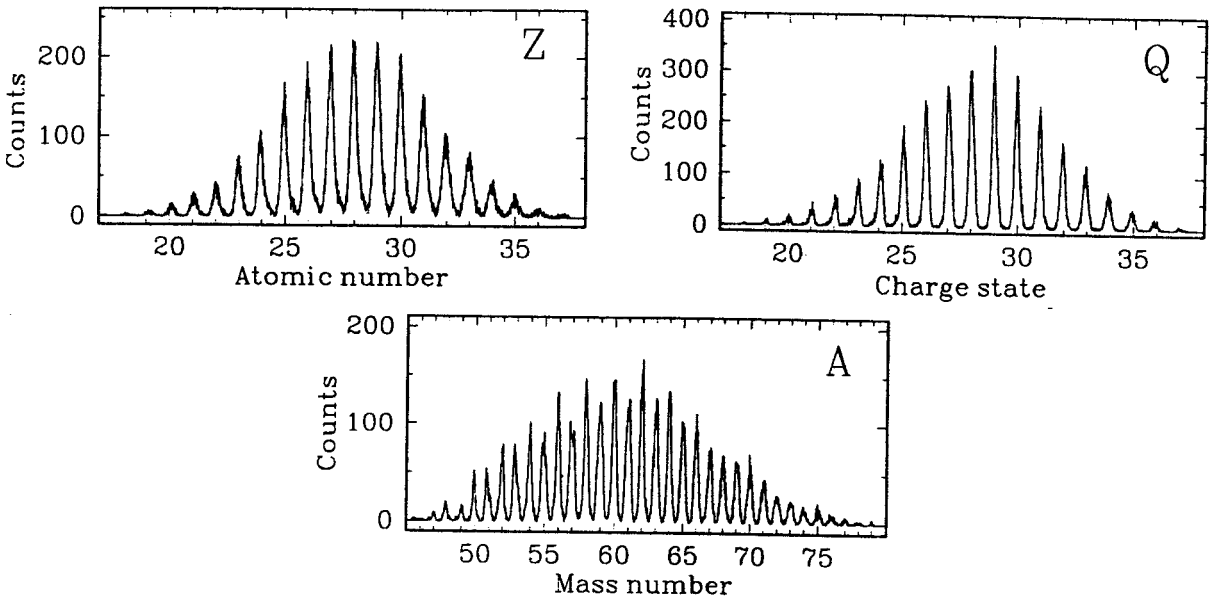

Figure 2: Distributions of proton number Z, charge state Q, and mass A. All data were obtained with the same A1200 settings (Bρ=2.36). Note the good resolution for all parameters.

The time–of–flight (TOF), energy loss, and total kinetic energy was determined for each particle traversing the separator. Together with the values of the magnetic fields of the A1200 dipoles, this information was used to unambiguously determine the mass A, proton number Z, and charge state Q of all particles. Figure 2 shows the good resolution obtained for these parameters.

Previous studies of ^{86}Kr–induced reactions include experiments by Bazin *et al.*[1] (44 MeV/nucleon, Al target) and by Weber *et al.*[3] (500 MeV/nucleon, Be target). The fragment production yields from the reaction at higher energy were very well reproduced by the empirical parametrization EPAX of Sümmerer *et al.*[6], which is based on data from relativistic energy reactions. The good agreement of the 500 MeV/nucleon data with this model thus indicates the dominance of the so–called "pure" fragmentation reaction process at 500 MeV/nucleon. In contrast to these results, Bazin *et al.*[1] have shown that at the much lower energy of 44 MeV/nucleon there is clear evidence for the appearance of two components in the production yield distribution for fragments close to the projectile (Z=33–37): one resulting from projectile fragmentation and the other representing nuclides produced via transfer reactions.

During our experiment we observed both multi–charge–pickup reaction products (strontium and possibly yttrium isotopes) and reaction products with higher masses than the projectile. Although the analysis of our data is still in progress, we have extracted some preliminary longitudinal momentum distributions for a number of reaction products close to the projectile, including a number of bromine and rubidium isotopes, as is shown in Figure 3. There seems to be a significant difference in both shape and width between the distribution of ^{81}Rb, which can only have been produced in a process involving proton transfer, and that of ^{77}Br. The latter distribution seems to be composed of two components. This could indicate that for this projectile–like "fragment", transfer reactions still contribute strongly to the total production yield at 70 MeV/nucleon. However, these results are preliminary and no definite conclusions can be made at this early stage of the analysis.

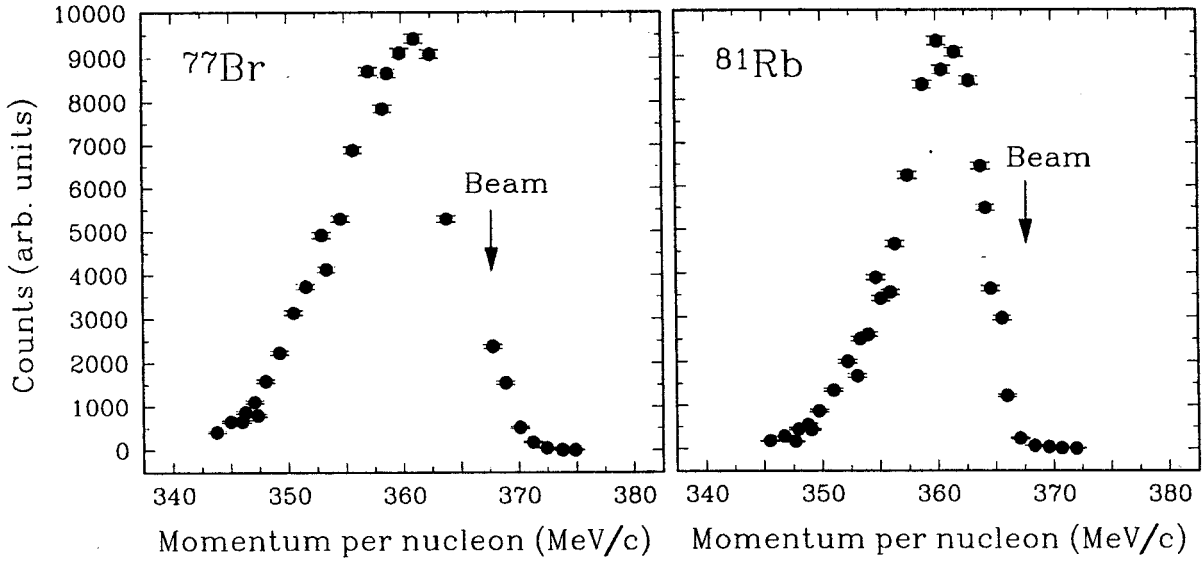

Figure 3: Longitudinal momentum distributions for two projectile–like reaction products. See the text for a discussion of the differences in shape and width.

As the analysis process continues more detailed data will be extracted for nuclei with Z>20, including both parallel momentum distributions and production cross sections. Apart from the widths and shapes of the momentum distributions of different fragments, the shift of their centroids relative to the momentum of the incoming beam particles is also of great interest. We also intend to compare our results to predictions by theoretical models that have shown to be very successful in the description of fragmentation (and charge-pickup) reactions at relativistic energies. Finally, the good resolution of our data provides us with confidence that we will be able to extend our reaction mechanism studies at intermediate energies to even heavier projectiles, e.g., cadmium and xenon.

References

1. D. Bazin *et al.*, Nucl. Phys **A515** (1990) 349.
2. M. F. Mohar *et al.*, Phys. Rev. Lett. **66**, (1991) 1571.
3. M. Weber, Ph. D. thesis, Technische Hochschule Darmstadt (1993).
4. B. M. Sherrill *et al.*, Nucl. Instrum. Methods **B56** (1991) 1106.
5. S. J. Yennello *et al.*, Phys. Rev. **C46** (1992) 2620.
6. K. Sümmerer *et al.*, Phys. Rev. **C42** (1990) 2546.